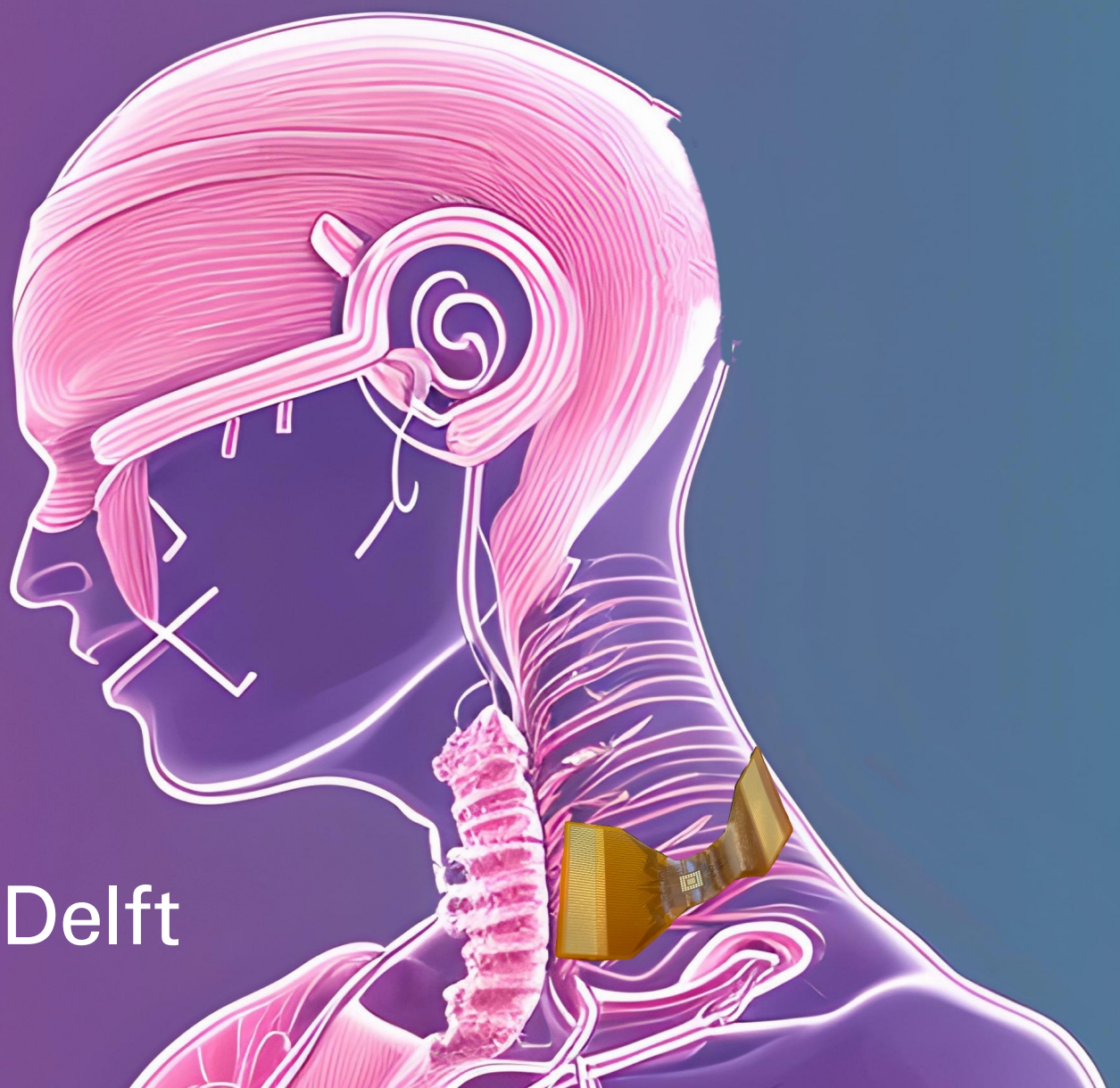# A Wearable Ultrasonic Vagus Nerve Stimulator

## Design and Fabrication of Piezoelectric Transducer Prototype

Chunyan Xue

**TU**Delft

# A Wearable Ultrasonic Vagus Nerve Stimulator

## Design and Fabrication of Piezoelectric Transducer Prototypes

Thesis report

by

# Chunyan Xue

to obtain the degree of Master of Science
in Electrical Engineering
at the Delft University of Technology

| | |
|---|---|
| Thesis Committee: | Dr. T. Costa |
| | Dr. F. A. Cardoso |
| Supervisor: | Dr. T. Costa |

| | |
|---|---|
| Project Duration: | September, 2022 - August, 2023 |
| Student number: | 5456460 |

An electronic version of this thesis is available at `http://repository.tudelft.nl/`.

Delft University of Technology

# Abstract

Vagus nerve stimulation serves as an approach to manage drug-resistant epilepsy. Focused ultrasound stands out as a unique tool, offering a non-invasive modality for VNS (Vagus Nerve Stimulation). With its excellent depth of penetration and sub-millimeter focusing capabilities in soft tissue, ultrasound allows for precise targeting of the vagus nerve without the need for surgical intervention. This technology relies on piezoelectric transducers that convert electrical energy into ultrasonic waves. However, the high costs and technical difficulties associated with the production of these arrays have led to limited commercialization of piezoelectric transducer arrays.

This thesis investigates the design, fabrication, and optimization of a small, low-cost phased-array piezoelectric ultrasonic transducer. The transducer is specially designed for non-invasive UVNS applications in the form of a small patch for the neck. The research is dedicated to the fabrication of the transducer array, designing a transducer capable of both transmitter (TX) and receiver (RX) functions, which in the future can be used for simultaneous image-guided neural regulation. Two prototypes were fabricated: one is a 256-element 2MHz rectangular transducer array integrated into an 8-layer stacked rigid printed circuit board (PCB), and the other is a dual-frequency array integrated into a 4-layer flexible PCB substrate, explicitly designed for simultaneous imaging and neural modulation.

The study utilized two key materials, the well-known PZT and the lesser-known but promising <001> oriented PMN-0.3PT piezoelectric single crystal. Through extensive optimization, air-filled PZT transducer arrays were realized, and the cutting parameters for PMN-PT were significantly improved. A unique aspect of the fabrication was the use of flip-chip technology to directly integrate the air-filled 2D array onto the PCB, a method seldom detailed in existing research.

While exhaustive testing on phase-delayed beam-forming and imaging capabilities could not be conducted due to equipment limitations, preliminary evaluations of the capacity to generate plane waves were made. The properties of the bulk PZT and PMN-PT transducers were characterized. It was observed that the PMN-PT transducer generated significantly lower ultrasonic pressure compared to the PZT transducer, which aligns with expectations due to the fragile nature of PMN-PT. The first prototype of the PZT array transducer was successfully fabricated and assessed, achieving a pressure of 176 kPa at its 10 mm natural focal point. Subsequently, the internal array second of the prototype was fabricated and evaluated, registering a pressure of 1.14 MPa at the 1.2 mm natural focus point. The results demonstrate the feasibility of building complex piezoelectric arrays using optimized fabrication methods. This lays the foundation for future prototypes to test beam-forming capabilities and for fabrication of the complete equipment afterwards.

**Key words:** Ultrasound piezoelectric transducer, non-invasive Vagus nerve stimulation, Image guided neuro-modulation, PZT, PMN-PT, Fabrication

# Contents

# Nomenclature

**List of Abbreviations**

ACF    Anisotropic Conductive Film

FPCB  Flexible Printed Circuit Board

FUS    Focused Ultrasound

HIFU   High-intensity Focused Ultrasound

ICA     Isotropic Conductive Adhesive

IPA     Isopropyl Alcohol

MEMS  Micro-Electro-Mechanical-Systems

PCB    Printed Circuit Board

PDMS  Polydimethylsiloxane

PMN-PT  Lead Magnesium Niobate-lead Titanate

PZT    Lead Zirconate Titanate

RX     Receive

TX     Transmi

VNS   Vagus Nerve Stimulation

**List of Symbols**

$\epsilon$      Dielectric Constant

$\lambda$      Wavelength

A      Surface Area

AR    Aspect Ratio

$C_{33}$   Clamped Capacitance

d      Piezoelectric Coefficient

fa     Anti-Resonance Frequency

fr     Resonance Frequency

IL     Insertion Loss

K     Piezoelectric Coupling Coefficient

L      Length

Q     Quality Factor

t      Thickness

Tc    Curie Temperature

v     Sounds velocity

W    Width

Za    Acoustic Impedance

# List of Figures

# List of Tables

<div align="right">

# 1

</div>

<div align="right">

# Introduction

</div>

## 1.1. Background

### 1.1.1. Vagus Nerve Stimulation

The vagus nerve (VN) is essential to the autonomic nervous system. It emanates from the cranial base and passes through the neck, bridging the brain and internal organs. Vagus nerve stimulation(VNS) is an effective treatment for medically refractory epilepsy that got approved by FDA [1].

The typical clinical application of VNS is through implanted Vagus Nerve Stimulation (iVNS). In this method, a pulse generator is implanted under the skin of the upper chest, and the electrode is connected to the left vagus nerve in the neck. Through iVNS, electrical pulses are delivered to the nerve, and the signals are then transmitted to the brain. As of 2021, over 125,000 patients worldwide have undergone iVNS implantation treatment [2]. Compared to other methods like transcranial electrical stimulation or craniotomy surgery, iVNS is convenient, effective, and less invasive. However, it still requires electrode implantation through surgery, which carries some degree of trauma and potential risk of nerve damage.

Non-invasive VNS is a novel alternative method that offers a non-surgical and cost-effective option [3]. One approach to non-invasive VNS involves electrical stimulation, which attaches to the neck or auricle and acts directly on the skin rather than the nerves [4]. This has challenged perception and pain thresholds and raised concerns about effectiveness and potential side effects on neighbouring tissues. With such limitations and risks, ultrasound has emerged as a promising contender. Building on decades of experience with focused ultrasound technology, ultrasound presents an innovative approach that has the potential to bridge the gap between the precision of iVNS and the need for minimally invasive techniques.

### 1.1.2. Focused Ultrasound Transducers

Ultrasound has been an integral tool in medicine for decades. In ultrasound diagnostics, the transducer emits ultrasound waves and receives their echoes, creating real-time images of human tissues. Ultrasound transducers can focus ultrasound waves to perform tissue ablation or nerve stimulation for therapeutic purposes. Instead of using electrical or magnetic stimulation, precisely calibrated ultrasound waves can be focused on specific targets located anywhere. Hence, it offers unprecedented spatial resolution and precision control compared to other non-invasive neuro-modulation methods. The treatment can be done with a probe attached to the skin, and it has been proven not to have any biological side effects. Moreover, ultrasound has the unique capability of providing real-time imaging of the targeted area. The imaging feature allows for accurate visualization of the anatomical structures, aiding in the precise placement of the stimulation and ensuring that the intended neural circuits are effectively targeted. Furthermore, the integration of imaging and stimulation in the same device presents an opportunity for image-guided

neuro-modulation. This integrated approach allows for real-time feedback during the stimulation process, improving the efficiency and accuracy of the treatment. It could open up new possibilities for precise and effective neuro-modulatory therapies.

Ultrasonic nerve stimulation devices generate and transmit ultrasound waves through a piezoelectric transducer probe. A phased array transducer comprises many small piezoelectric elements arranged in a specific pattern. These elements can be individually controlled to generate and receive ultrasonic waves. By controlling the time delay of the transmitting (or receiving) pulses of each array element, the phase relationship of the sound waves arriving at (or leaving) a point within an object is changed. This allows the phased array transducer to focus and direct the ultrasound beam in different directions without physically moving the transducer itself. This technique enables targeted neuro-stimulation with minimal invasiveness and greater precision in clinical applications.

## 1.2. Research Gap and Project Approach

The neuro-modulation capability of ultrasound phased-array transducers depends on transducer size and shape design, centre frequency, and material selection. Applying application-specific transducer arrays with proper design can provide optimized performance. However, the miniaturization of phased array transducers pose complex and challenging fabrication processes. In the past, medical ultrasound arrays faced technical barriers that hindered the construction of large aperture, high-power, and densely phased arrays, limiting their full potential in therapeutic applications. In the current marketplace, commercially available phased array transducers tend to be large in size and mainly use linear array configurations. While these linear arrays have proven effective in a wide range of applications, they have limitations in terms of portability and adaptability to specific clinical scenarios.

Researchers have been consistently investigating ways to minimize the physical size, optimize array configurations, and seek higher output power of ultrasound transmission within limited spaces effectively. The medical ultrasound array design field encompasses various 2D and 3D innovative designs, including dual-frequency transducers, kerfless, and sparse arrays. Emerging technologies have been employed in transducer manufacturing, such as CMUT (Capacitive Micro-machined Ultrasonic Transducers), multi-layer piezoelectric materials, piezoelectric material/polymer composites, single-crystal materials, and ultra-fine pitch arrays. Some of these technologies have already been commercialized, resulting in improved ultrasound image quality.

While advancements are palpable, the field still grapples with unresolved critical issues. Designing an array capable of precise, high-energy focused ultrasound often escalates its size – an unfitting trait for miniaturized applications like the vagus nerve neck patch, calling for distinct design considerations. Conventional manufacturing methods need to be improved when dealing with new demands. High-precision cutting and assembly are required for transducer arrays, particularly in small-sized and high-density arrays, which can be challenging. Meeting the specific requirements of phased arrays while optimizing the cutting process to preserve the ultrasonic emission capability and yield is an area that needs exploration. Introducing new materials in ultrasound technology brings potential advantages but presents new technical challenges. These materials have unique physical properties and process requirements, necessitating thorough testing and experimental validation to ensure manufacturing feasibility and stability.

## 1.3. Motivation and Objectives

The primary objective of this thesis is to design and fabricate a miniaturized phased array piezoelectric ultrasound transducer prototype. This prototype is envisioned for non-invasive UVNS applications, specifically as a patch to be positioned on the neck, holds potential for adaptation in rodent research during preliminary study phases. Such a concept has not yet been commercialized and remains sparsely studied in current research. The key design objective is to incorporate phase delay technology to generate focused beam-forming ultrasound, enabling it to function as both a transmitter (TX) and receiver (RX). Through proper circuit design and algorithm implementation, the transducer will have the capability to perform both imaging and stimulation functions, ultimately acting as an image-guided simulator.

This research will investigate the design and optimization of miniature UVNS transducer arrays from both advanced materials and array configuration design perspectives. Emphasis will be placed on addressing the challenging fabrication process, particularly the dicing of the transducer arrays and their assembly. In the early stages of development, integrating the transducer prototype directly onto a customized printed circuit board is a common approach. This allows the performance of the transducer array to be tested without having to spend years developing the entire chip.

Two prototypes have been designed, fabricated, and tested. The first prototype is a 256-element transducer array. This is a rectangular 8x32 array with an aperture of 2.78mmx11.42mm and a center frequency of 2MHz. An 8-layer stacked rigid PCB was used to directly integrate the array of elements onto it, and each element can be driven individually. The prototype transducer was fabricated using two kinds of piezoelectric materials separately. One is PZT, a widely studied and commercialized piezoelectric material. The other is <001> oriented PMN-0.3PT piezoelectric single crystal, a promising piezoelectric material that has yet to be widely studied or commercialized due to the difficulty of fabrication. Optimal recipes are constructed by exploring fabrication methods that maximize the retention of array integrity and minimize disruption to the piezoelectric properties of the material. After connecting the signal source, a plane wave output test is conducted to analyze the performance of the transducer.

The second prototype is a dual-frequency array designed to perform both imaging and neuromodu-lation functions on the same array. The array consists of two parts: an internal 6x6 array with 36 elements, operating at a center frequency of 4MHz for stimulation, and an external square peripheral-shaped array with 48 elements, operating at a center frequency of 2MHz for imaging.

Due to experimental instrumentation limitations, the phase-delay beamforming test, or imaging ca-pability test, are currently unavailable. Nevertheless, both prototypes are designed to be phase-delayed arrays, thus satisfying their parameter requirements. Currently, the effectiveness of plane wave generation is being tested to ensure optimal performance. In future work, the complete performance of the array can be tested by connecting the phase wave generator and the image processing unit.

## 1.4. Thesis Structure

Chapter 1 presents the medical application context of this study, including an overview of the latest developments in medical research and industry. It outlines the objectives and plans for this study.

Chapter 2 delivers the theoretical foundation encompassing the concepts of ultrasound, principles, and significant parameters of piezoelectric transducers. Further, it clarifies the properties of the two piezoelectric materials employed in this study. It discusses the principles and selection of phased array configurations as well as key considerations for 2D array parameters.

Chapter 3 delves into a detailed explanation of the process leading to the fabrication work, analyz-ing and choosing among multiple phased array fabrication methodologies and techniques. It also outlines the specifics of designing a custom PCB for integrating the transducer array.

Chapter 4 illuminates the core of this research, detailing the comprehensive process of prototyping two transducer arrays. This includes investigating the dicing process, its optimization, and the transducer assembly procedure.

Chapter 5 presents the results derived from the measurements, including an explanation of the ex-perimental setup, a multi-angle portrayal of the measured beams, and a comparison with the theoretically calculated values.

Lastly, Chapter 6 concludes by summarizing the findings and highlighting the experiment's limitations. It further suggests potential areas where future work can improve and optimize every aspect of the study.

# 2

# Theoretical Background

## 2.1. Basics of ultrasound

### 2.1.1. Ultrasound waves

Sound waves are the state of mechanical vibration of an object and the form of energy propagation. Sound frequency refers to the number of vibrations per second and is measured in hertz (Hz). The human ear is capable of perceiving sound waves within 20Hz to 20kHz. When the frequency exceeds 20kHz, it is classified as an ultrasonic wave.

Ultrasound has unique advantages in medicine. It has higher energy levels, frequencies, and shorter wavelengths, resulting in minimal diffraction. This allows them to travel in straight lines with good beam formation and directionality over a distance. Sound waves can be described in terms of frequency, wavelength, and wave speed as follows.

$$f = v/\lambda \tag{2.1}$$

$$v = \sqrt{\frac{K}{\rho}} \tag{2.2}$$

Where $\lambda$ is the wavelength, v is the speed of sound in the medium, and f is the frequency. The frequency is inversely proportional to wavelength. In medical ultrasound applications, wavelength determines the ultimate resolution of the image, while frequency determines the depth of tissue that can be imaged.

The speed of ultrasonic waves varies depending on the medium through which it travels, influenced by the density ($\rho$) and the medium's bulk modulus (K). The bulk modulus represents the medium's resistance to external pressure. Solids typically have a more significant sound speed than liquids, while ultrasound propagates the lowest in gases. Regarding human tissues, their propagation speed is generally close to water's. Table 2.1 presents the different media considered in this work along with their corresponding sound speeds.

Several wave propagation modes exist in a medium, such as longitudinal, transverse, and lamb waves. The medical ultrasound field is mainly associated with longitudinal and transverse waves.

Ultrasound is not only dependent on the medium to propagate but also interacts with the medium, resulting in various effects. For example, the acoustic energy will cause high-frequency vibration of the mass. That results in mechanical effects, such as speed, sound pressure, sound intensity, and other mechanical quantities changes; the acoustic energy also causes thermal effects due to energy absorption in the medium. When ultrasound acts on biological tissues, the physical effects produce specific biological effects. In the field of ultrasound neuro-modulation, low-intensity ultrasound (US) is transmitted to the nervous system tissue, leading to the transient modulation of neural activity [5]. Ultrasound can induce

either excitatory or inhibitory effects on the nerves at the stimulation site through various parameters such as intensity, frequency, pulse width, and duration. This leads to bidirectional and reversible changes in neural function.

**Table 2.1:** Speed of Sound in Different Media

| Medium | Speed of Sound (m/s) | Acoustic Impedance (MRayls) |
|---|---|---|
| Air | 330 | 0.00043 |
| Water | 1,480 | 1.48 |
| Soft Tissue (average) | 1,540 | 1.69 |
| Parylene | 2,350 | 2.58 |
| PZT | 4,350 | 33.71 |
| PMN-PT | 4,601 | 36.8 |
| Aluminum | 6,260 | 18 |

### 2.1.2. Interaction of Ultrasound waves

Sound waves will be reflected and transmitted when they travel through different media. As shown in figure 2.1, part of the energy is reflected at the interface, and the other part continues to propagate forward.
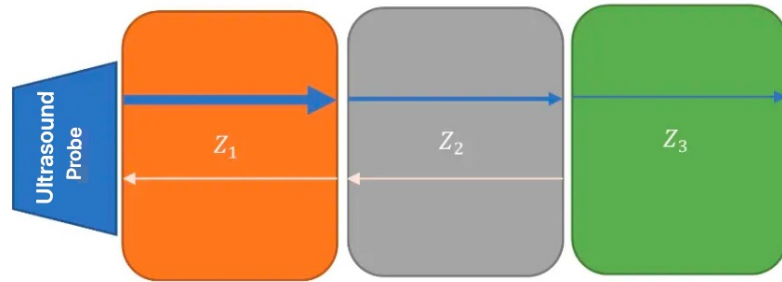


**Figure 2.1:** Ultrasound Reflection and Attenuation when Travel Through Different Media [6]

The propagation characteristics can be quantified by two parameters: the reflection and transmission coefficients. The Reflection coefficient refers to the proportion of energy that is reflected into the original medium at the interface. The transmission coefficient refers to the proportion of energy that continues to propagate into the next medium at the interface. Their values depend on the acoustic impedance mismatch between the two sides of the interface.

Reflection Coefficient:

$$R = \left( \frac{Z_2 + Z_1}{Z_2 - Z_1} \right)^2 \tag{2.3}$$

Transmission Coefficient:

$$T = 1 - R = \frac{4Z_1 Z_2}{(Z_2 + Z_1)^2} \tag{2.4}$$

$Z_1$ and $Z_2$ are the acoustic impedance of the first and second media, respectively. The acoustic impedance $Z_a$ is the resistance when the sound wave propagates through different materials. The density and stiffness of the material determine $Z_a$. The heavier and stiffer materials have higher acoustic impedance, and lighter and softer materials have lower acoustic impedance. The difference in acoustic impedance between two

materials is known as an impedance mismatch. The greater the acoustic impedance mismatch is, the more energy is reflected at the boundaries of the two mediums, and the less efficiently the acoustic energy transfer.

## 2.2. Piezoelectric Transducer

The ultrasound transducer is the core component of a medical ultrasound system because it converts the electrical signals from the system into ultrasound waves that are emitted. It also can receive ultrasound signals and convert them back to electrical signals. Piezoelectric materials realize these two functions. Therefore, this section will introduce the principles and properties of the piezoelectric effect, followed by a discussion of the piezoelectric parameters that are of interest. Then, the piezoelectric materials used in this work will be presented. Ultimately, the design considerations regarding the transducer profile based on the material parameters will be explained in detail.

### 2.2.1. Piezoelectric Effect

Piezoelectric transducers play a crucial role in generating ultrasonic waves. These transducers rely on the properties of piezoelectric materials, which can convert electrical energy into mechanical energy and vice versa. The term "piezo" originates from the Greek word for "pressure," highlighting the material's ability to respond to pressure changes. The discovery of piezoelectricity can be credited to the pioneering work of Jacques-Paul Curie and Pierre Curie in 1880 [7]. Their studies on various crystals showed that certain materials exhibited unique behaviour.
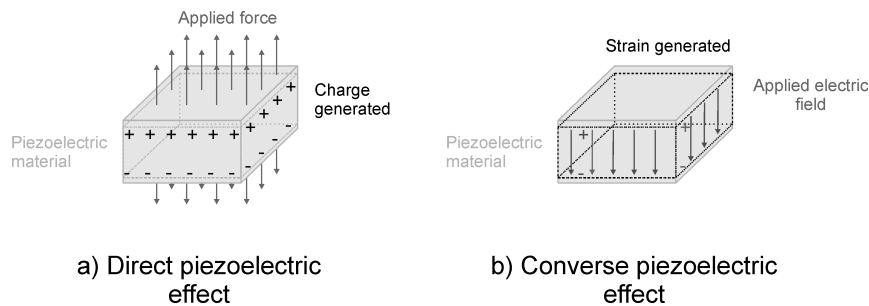


**Figure 2.2:** Schematic of Piezoelectric Effect [8]

When pressure is applied to piezoelectric materials, they undergo deformation, changing their internal lattice spacing. This separates the material's positive and negative charge centers, causing a polarization phenomenon. As a result, positive and negative charges accumulate on the opposite surfaces of the material. This effect is now known as the direct piezoelectric effect, as shown in Figure 2.2(a). When the external force is removed, it returns to an uncharged state; when the direction of the force is changed, the polarity of the charge is also changed.

These dielectrics are also deformed when an electric field is applied to the polarization. Under an alternating electric field, its internal stress and deformation will undergo periodic changes, thus generating mechanical vibration. This is known as the converse piezoelectric effect, as shown in Figure 2.2(b). The piezoelectric effect in materials occurs due to the induced polarization resulting from an external electric field. The magnitude and direction of this polarization are influenced by the material's properties, dimensions, and the strength and direction of the applied electric field. Ultrasonic transducers operate based on both converse and direct effects.

### 2.2.2. Piezoelectric Parameters

Various factors need to be considered to select the optimum piezoelectric material for a particular application, including dielectric, piezoelectric and acoustic properties [9]. These are explained in the following sections.

**Resonant frequency**

Theoretically, the resonant frequency is the optimal frequency at which a piezoelectric material vibrates most efficiently, thereby converting electrical energy into mechanical energy with the highest efficiency. At the circuit level, this frequency, where the impedance is at its minimum, is termed the series resonance frequency. Conversely, a scenario arises in the equivalent circuit where the impedance is theoretically infinite; this is known as the parallel resonance frequency, fp, often referred to as the anti-resonance frequency [10]. The resonant frequency is the specific frequency at which a piezoelectric material most efficiently vibrates, converting electrical energy into mechanical energy. The resonant frequency is also known as the half-wavelength resonant frequency. This is the frequency at which the wavelength of the sound wave inside the material is equal to half of its thickness. The formula is given by:

$$fa = \frac{V}{\lambda} = \frac{V}{2t} \tag{2.5}$$

Where v represents the speed of sound inside the material, $\lambda$ is the ultrasound wavelength, and t represents the thickness of the material.

When a sound wave of this frequency passes through a piezoelectric material, phase-length interference occurs, resulting in resonance [11]. This means the mechanical vibrations are in phase with the applied electrical signal, resulting in the largest and most efficient energy transfer.

**Piezoelectric Coefficient**

The piezoelectric coefficient d33 is the conversion factor between mechanical stress or strain and electric charge. It characterizes the magnitude of strain produced per unit voltage in the thickness direction. The piezoelectric coefficient has two subscripts; the first number, I, refers to the direction of the electric field and the second number, j, refers to the direction of the stress. The subscript of d33 indicates that the direction of polarization and the electric field applied is the same. The relationship between piezoelectric coupling coefficient $K_{33}$ and piezoelectric coefficient $d_{33}$ is:

$$d_{33} = k_{33} \cdot \varepsilon_0 \cdot \varepsilon_r \tag{2.6}$$

Where $\varepsilon_0$ is the vacuum permittivity, $\varepsilon_r$ is the relative dielectric constant.

**Piezoelectric Coupling Coefficient**

The electromechanical coupling coefficient k is the ratio of the energy gained from electromechanical conversion to the total energy input [12]. For the direct piezoelectric effect, if an external force is applied to the material, only a part of the external force can be converted into electrical energy, while the rest deforms the material and thus is stored as elastic energy; for the reverse piezoelectric effect, the total applied external electric field can only be partially converted into mechanical energy, while the rest polarizes the material and is stored in the form of electrical energy. The effective coupling factor, $k_{\text{eff}}$, quantifies the difference between the frequencies $f_r$ and $f_a$. It is defined as:

$$k_{eff} = \sqrt{\frac{f_a^2 - f_r^2}{f_a^2}} \tag{2.7}$$

This metric offers insights into the energy conversion efficiency between electrical and mechanical domains in a piezoelectric system. The closer $f_r$ and $f_a$ are, the higher the $k_{\text{eff}}$, indicating a more efficient transducer. The value of $k_{\text{eff}}$ ranges between 0 and 1. When $k_{\text{eff}} = 0$, it signifies the absence of any piezoelectric effect. Under the condition that the polarization direction is the same as the thickness direction, there are also several common electromechanical coupling coefficients, as shown bellow[13]:

- Planar electromechanical coupling coefficient Kp: characterizes the radial expansion vibration of a thin wafer-shaped piezoelectric material. The condition is that the wafer diameter is ≥ 3 times the wafer thickness t.

- Transverse vibration electromechanical coupling coefficient K31: Reflects the electromechanical coupling effect when the long lamellar piezoelectric material vibrates along the length direction. The condition is that the length of the wafer l ≥ 3 times the width and thickness of the wafer.

- Longitudinal vibration electromechanical coupling coefficient K33: Reflects the electromechanical coupling effect of the telescopic vibration along the length direction of the long and thin column-shaped piezoelectric crystal. The condition is that the length is l ≥ 3 times the rod's width and thickness or diameter. These are the vital parameters used in this work since the individual element of the transducer array is thin column-shaped. where s33 represent piezoelectric stress constant.

- Thickness vibration electromechanical coupling coefficient Kt reflects the electromechanical coupling effect of the stretching vibration along the thickness direction of the thin sheet piezoelectric crystal. When the piezoelectric material is operated in the thickness mode, kt value can be calculated based on the resonant and anti-resonant frequencies.

$$k_t = \sqrt{\frac{\pi}{2}\frac{f_r}{f_a}\tan\left(\frac{\pi}{2}\frac{f_a - f_r}{f_a}\right)} \tag{2.8}$$

The condition is that the wafer thickness is less than the wafer edge length or diameter, commonly used to characterize bulk transducers. In bulk-type transducers, the piezoelectric material operates in the thickness vibration mode. The transducer's electromechanical conversion performance, or sensitivity, is enhanced by a higher value of Kt. However, in addition to the thickness vibration, radial vibration is present in the piezoelectric wafer, represented by Kp. This radial vibration can interfere with the desired thickness vibration, which causes waveform distortion or increased clutter. Therefore, it is desirable to minimize the value of Kp.

**Clamped Capacitance**

The piezoelectric material itself can be considered as a capacitor. The clamp capacitance is determined by the clamp dielectric constant, the area, and the thickness.

$$C_{33} = \frac{\epsilon_{33} \cdot A}{t} \tag{2.9}$$

Where $\epsilon_{33}$ is the dielectric constant, A is the area, and t is the thickness of the piezoelectric material. Ultrasonic transducers primarily work in the MHz range. A small capacitance means a sizeable capacitive reactance suitable for use as a high-frequency piezoelectric element. Therefore, it is better to have a smaller ε. To maximize power transfer, the input resistance of the ultrasonic transducer should be true at the specified frequency, and its input resistance should match the electrical impedance of the source (typically 50Ω when terminated)[14].

**Quality Factor**

The quality factor Q reflects energy loss characteristics. It is defined as the ratio of the energy stored in the transducer to the energy lost per vibration cycle.

$$Qm = \frac{fr}{f2 - f1} \tag{2.10}$$

In the above equation, $fr$ is the resonance frequency, and $f1$ and $f2$ are the frequencies at -3 dB of the maximum admittance. The quality factor affects many aspects of transducer performance, such as bandwidth, sensitivity, and signal-to-noise ratio. A high Qm is generally preferred for imaging transducers as it leads to a narrower bandwidth and higher resolution. A high Qm means the transducer can more efficiently convert electrical energy into mechanical energy. For transmitting transducers, on the other hand, a lower Qm is often favourable. Because a lower Qm corresponds to a wider bandwidth of frequencies over which the transducer can operate efficiently. In the case of image-guided stimulation transducers, stimulation is the primary function, and imaging is secondary. Therefore, a higher Qm may be preferable for better stimulation efficiency and accuracy.

**Curie temperature**

The Curie temperature indicates the temperature at which a piezoelectric material undergoes a phase transition from a polarized to an unpolarized state. When the temperature exceeds Tc, the material loses

its piezoelectric properties and becomes unpolarized, making it impossible to generate or detect sound waves. The closer the ambient temperature to the Curie temperature, the more significant the property degradation. Therefore, in the fabrication process, the temperature must be kept well below the Curie temperature and better not exceed half of the Curie temperature.

### 2.2.3.  Principle of choosing parameters

For the application of this work, which involves a 2D piezoelectric transducer array for vagus nerve stimulation, several factors need to be carefully considered in the selection of piezoelectric materials

Firstly, miniaturization is a crucial consideration. The array aperture should be as small as possible to achieve a compact design for comfortable placement in the neck region. In order to generate strong ultrasound waves for effective nerve stimulation, it is important to prioritize a high k33 value. The higher the k33, the more efficient to convert electrical energy into mechanical vibrations. The d33 value is equally important as it determines the material's sensitivity and responsiveness to mechanical stress, directly impacting the transducer's ability to generate electrical charges effectively.

The first manufacturing consideration is the Curie temperature. The Curie temperature of the material should not exceed half the required operating temperature to ensure stability, so materials with higher Curie temperatures are more suitable for high-temperature manufacturing processes. In addition, mechanical strength and durability, cost, availability, and other practical factors must be considered to ensure the viability and scalability of the sensor array.

## 2.3.  Piezoelectric Materials

There are four types of piezoelectric materials, single crystals, ceramics, polymers and composites [12].

- Single crystal
  A single crystal is a naturally formed or artificially made, anisotropic single-crystal ferroelectric material, and its piezoelectric effect is caused by the relative position change of positive and negative ions on the lattice that makes up the crystal structure. Common materials include quartz ($SiO_2$), lithium niobate ($LiNbO_3$), lithium sulfate ($Li_2SO_4$), lead magnesium niobate-lead titanate (PMN-PT) etc.

- Ceramics
  Ceramics is a polycrystalline ferroelectric material made by artificial firing via powder sintering. Commonly used piezoelectric ceramics are barium titanate ($BaTiO_3$), lead zirconate titanate (PZT) etc.

- Polymer
  Polyvinylidene fluoride (PVDF) has the best performance; it is biocompatible and suitable for in-vivo application.

- Composite
  It is formed by dispersing and mixing ferroelectric ceramic particles in polymer materials, such as PVDF and PZT composite materials, as well as zinc oxide (ZnO) piezoelectric film.

Among these different types, the two materials chosen for this study are PZT (lead zirconate titanate) and PMN-PT (lead magnesium niobate-lead titanate). They have been widely recognized for their excellent piezoelectric properties and extensively studied and utilized in various applications. The specific features and advantages of PZT and PMN-PT are described in the following sections, highlighting their applicability to this work.

### 2.3.1.  PZT

PZT is a widely recognized ceramic material utilized in various applications for its excellent piezoelectric properties and cost-effectiveness. Compared to other piezoelectric ceramics, PZT offers higher sensitivity, high k33 ($\sim$0.7), d33(300$\sim$600 Pc/N), and dielectric constant($\sim$1300) [15]. It also has a relatively high Curie temperature ($\sim$300°C), making it suitable for high-temperature environments and compatible with different manufacturing processes.

PZT materials can be categorized into different types based on their physical and chemical properties. Hard materials include PZT-2, PZT-4, and PZT-8, while soft materials encompass variants like PZT-5, which further include PZT-5A, PZT-5D, PZT-5H, PZT-5X, and so on [16]. Each type offers unique characteristics suitable for specific applications.

For instance, PZT-8 is a Fe and Ca-modified binary system material known for its low strong-field dielectric loss and high mechanical strength. It is commonly used to produce large sonar-type transducers [17]. PZT-4, modified with iron platinum and manganese calcium, exhibits high electromechanical conversion efficiency, making it ideal for high-power ultrasonic generator applications, ultrasonic processing, and ultrasonic cleaning components [16].

**Table 2.2:** Property Comparison of Different Materials

| Property | Material | | | |
|---|---|---|---|---|
| | PZT-5A | PZT-5H | <001>PMN-0.3PT | PVDF polymer |
| $\epsilon_{33}$ | 1250 | 1460 | 965 | 6 |
| $d_{33}$ (pC/N) | 390 | 650 | 1285 | 33 |
| $k_{33}$ | 0.75 | 0.70 | 0.90 | N/A |
| $k_t$ | 0.49 | 0.55 | 0.46 | 0.3 |
| $Z_a$ (Mrayl) | 34 | 34 | 36.5 | 3.9 |
| $T_C$ (°C) | 350 | 225 | 143 | N/A |
| Reference | [15] | [15] | [18] | [19] |

Among these, PZT-5, a La and Nb-modified material, is distinguished by its high sensitivity. It finds applications in various receiving hydroacoustic transducers, general transducers, and medical ultrasound probes. In medical ultrasound fabrication, PZT-5A and PZT-5H are commonly used piezoelectric materials. Their piezoelectric properties are shown in table 2.2. PZT-5A is renowned for its high impedance at elevated temperatures and high sensitivity and stability [16]. On the other hand, PZT-5H has an even higher sensitivity and dielectric constant compared to PZT-5A. However, its curie temperature is much lower, limiting its compatibility with specific manufacturing processes [16].

PZT ceramics must undergo a polarization process before being used. Polarization refers to exerting an external electric field that aligns the dipoles within the polycrystalline material, thereby creating a piezoelectric effect. This is illustrated in the top half of the figure 2.4. The imperfect arrangement of the ceramic dipoles results in a polarization rate of about 70%. This leads to an upper limit on the electromechanical coupling efficiency of the material [20].

Due to their inherent lack of conductivity, ceramics are typically coated with a layer of conductive metal on the upper and lower surfaces in the direction where the electric field is applied. This metal coating serves as electrodes and allows for the transmission of electric signals in ceramics. Regrettably, PZT ceramics exhibit a relatively high acoustic impedance (34 MRayls) compared to soft tissue (1.69 MRayls). This substantial difference in acoustic impedance between the tissue and the active element leads to considerable transmission and reception losses. Additionally, PZT ceramics have a brittle nature, creating processing challenges when fabricating phased array focusing transducers or thin films. Careful handling and processing techniques are necessary to mitigate the risk of damage during fabrication.

### 2.3.2. PMN-PT

PMN-PT, a single-crystal relaxor-based piezoelectric material, stands out among other piezoelectric materials due to its attractive properties. It boasts a high d33 ($\sim$1300 Pc/N), significant K33 ($\sim$0.92), high dielectric constant, and low losses, all contributing to its superior performance [18] . As can be seen in Table 2.3, the PMN-PT coupling coefficients are higher than the PZT for both the longitudinal and thickness modes, as well as for the vibrational modes of the piller in epoxy between these two modes.
The widespread use of PMN-PT has been limited due to mass production challenges and its higher cost. Nonetheless, recent advancements in production technology have significantly improved the performance of transducers, making it feasible to utilize PMN-PT as a core piezoelectric material for medical ultrasound transducers.

The complete chemical formula of PMN-PT is (1-x)[Pb(Mg1/3Nb2/3)O3]-x[PbTiO3]. The properties of PMN-PT crystals are significantly influenced by their orientation, composition, and growth process. These crystals exhibit diverse vibrational modes with different orientations; each well-suited for specific applications [21]. PMN-PT demonstrates optimal piezoelectric properties for this particular application when the composition x is in the range of 0.28-0.3, and the crystal orientation is along the <001> direction[21].
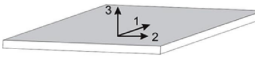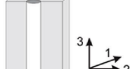
| thin flat plate | | long, thin rod in polymer matrix | | long, thin rod | |
|---|---|---|---|---|---|
| $k_t$ | | $\bar{k}_t$ | | $k_{33}$ | |
| PMN-30% PT | PZT | PMN-30% PT | PZT | PMN-30% PT | PZT |
| 0.62 | 0.49 | $k_t \leq \bar{k}_t < k_{33}$ | | 0.92 | 0.75 |
| $k_t = \dfrac{e_{33}}{\sqrt{c_{33}{}^D \epsilon_{33}{}^S}}$ $S_1 = 0, S_2 = 0, S_3 \neq 0$ $T_1 \neq 0, T_2 \neq 0, T_3 \neq 0$ | | $\bar{k}_t = \dfrac{\bar{e}_{33}}{\sqrt{\bar{c}_{33}{}^D \bar{\epsilon}_{33}{}^S}}$ $S_1 \neq 0, S_2 \neq 0, S_3 \neq 0$ $T_1 \neq 0, T_2 \neq 0, T_3 \neq 0$ | | $k_{33} = \dfrac{d_{33}}{\sqrt{s_{33}{}^E \epsilon_{33}{}^T}}$ $S_1 \neq 0, S_2 \neq 0, S_3 \neq 0$ $T_1 = 0, T_2 = 0, T_3 \neq 0$ | |
| (a) | | (b) | | (c) | |

**Figure 2.3:** K33 Comparison of PZT and PMN-PT Under Different Vibration Mode [22]

One of the contributing factors to the high $k_{33}$ value exhibited by PMN-PT is its single-crystal structure. The uniform structure of PMN-PT without grain boundaries enables superior polarization. PZT ceramics, with an irregular direction of the dipoles, hinder optimal dipole alignment during polarization, as shown in figure 2.4 [23]. This leads to reduced piezoelectric efficiency. While PMN-PT delivers higher ultrasonic energy per volume than other piezoelectric ceramics [15], a detailed comparison with PZT transducers remains to be conducted.

When preparing PMN-PT phased array transducers, the fabrication process often results in a significant decrease in the piezoelectric properties of PMN-PT. This decline in piezoelectricity hinders the optimal use of PMN-PT in transducers. The manufacturing challenges include:
Firstly, the absence of grain boundaries increases its brittleness. Due to the weak fracture toughness and high internal strength of PMN-PT, it is fragile and susceptible during processing [23]. Even during the initial dicing process, the yields are considerably lower than PZT ceramics when the wafer is cut into bulk pieces. Further phased array dicing requires optimization of the dicing conditions, including the dicing blade types, dicing speeds, and the selection of dicing modes. Companies such as Toshiba, Philips, and Tetrad, among others, have researched PMN-PT for its potential in medical ultrasonic applications. Currently, Philips states that their improved dicing technology has achieved the yields required for mass production of single crystal transducers but is still in the optimization phase due to cost and final performance considerations [24].
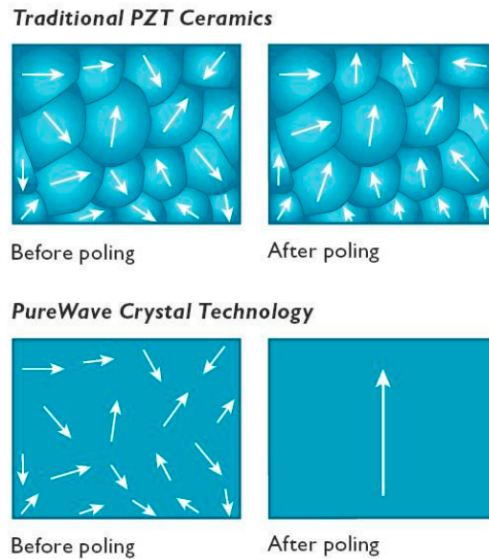
**Figure 2.4:** Dipole Modification Inside PZT and PMN-PT Crystals Before and After Polarization [23]

Secondly, PMN-PT has a low Tc (~150°C) and a low depolarization temperature Trt (~80°C), making it susceptible to depolarisation and loss of piezoelectricity. As shown in Figure 2.5, K33 and d33 of the PMN-PT sharply decrease when the ambient temperature is above Trt [25]. Before the Curie temperature has been reached, the k33 value is so low that the conversion of electrical to mechanical energy can no longer proceed, meaning that it no longer functions.
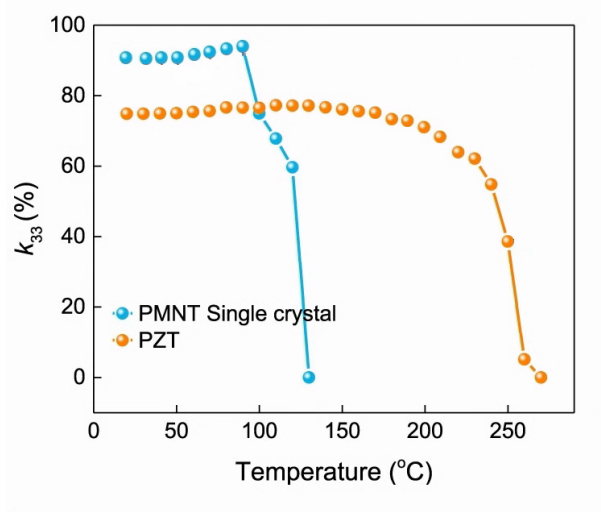


**Figure 2.5:** Temperature-dependent Piezoelectric Response of PZT and PMN-PT, revised from [25]

Although the ambient temperature for the final application is human body temperature (~37°C), processing often involves high temperatures. For example, integrating piezoelectric crystals onto chips or PCBs often involves a hot pressing process, and the blades' friction during array dicing also generates heat. In contrast, the piezoelectric properties of PZT ceramics remain unaffected and do not degrade throughout the manufacturing process, even when subjected to temperatures of 200°C. The choice of PMN-PT transducer fabricating and assembly processes is limited to avoid depolarisation.

One solution can be repolarisation after dicing the array. Repolarisation is a widely used procedure to

recover the degraded performance of PZT ceramic. This has also been used to enhance the performance of PMN-PT in several studies. The heat damage and the resulting depolarization can be corrected by re-applying specific electric fields, thereby recovering some of the piezoelectric properties. Repolarisation typically results in about 10% enhancement of piezoelectric properties, which are usually observed [26][27]. Another approach is to improve the crystal structure. Many research groups have been working on the development of high-temperature single crystal solutions such as Sc-doped PMN-PT, PIN-PMN-PT, and Mn-doped PIN-PMN-PT, etc. [24] [28]. These improved single-crystal materials can achieve higher Tc (200°C-300°C). However, their higher production costs, longer crystal manufacturing lead times, and incompletely optimized fabrication processes limit their more comprehensive application. Lastly, similar to PZT, the acoustic impedance difference between PMN-PT single crystal and biological tissue is large, leading to considerable energy transmission loss.

## 2.4. Phased array Transducer

Commercially available single-element transducer holds the capacity to consolidate an ultrasonic beam at its intrinsic focal point. Modifying the aperture dimensions and frequency generates a specific sound pressure level at this focal point. However, the limitation lies in the immutability of the natural focal point during operation, thus necessitating the displacement of the entire apparatus to attain focus at the required position. Conversely, an array transducer eliminates the need for manual repositioning and enables electronic control for meticulous focus manipulation.

This section describes the types of transducer arrays, their characteristics, and the choices for this work. It begins with an overview of the different shapes of array configurations and their appropriate working fields. Next, the principle of phased arrays and a brief explanation of how image-guided neural stimulation can be achieved with the array are presented. Next, the parameters of phased arrays are described, and finally, consideration and trade-offs of all these parameters define the array configuration used in this work.

### 2.4.1. Different Shapes of ultrasound array

Arrays come in various shapes, as shown in Figure 2.6. Individual array elements can be driven in various ways, such as simultaneously, one row at a time, or individually. When each array element can be controlled individually, it is termed a phased array.
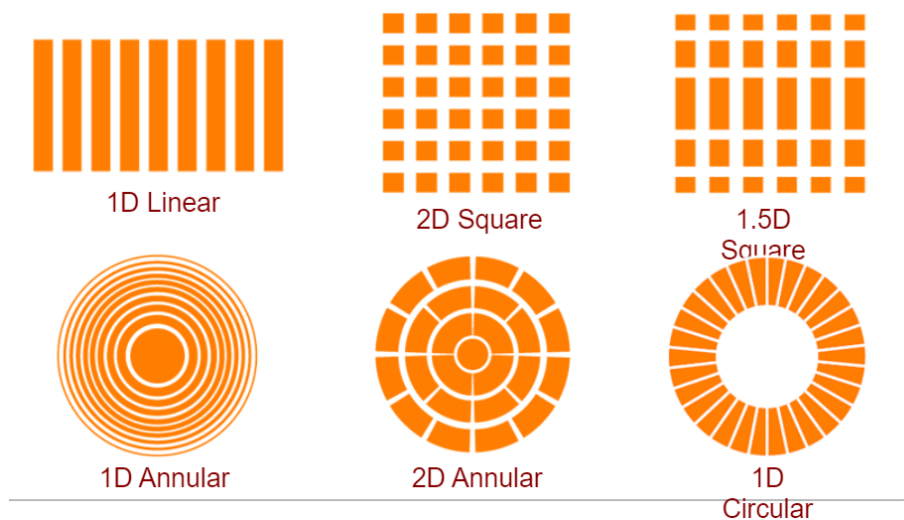


**Figure 2.6:** Different Transducer Array Configurations [29]

The different designs offer optimal performance for specific applications. Linear arrays are the simplest and most commonly used array configurations for imaging in multiple medical fields. Consisting of multiple

transducer elements arranged in a straight line, linear arrays have good axial resolution and are more feasible to manufacture. It has a relatively large size and element count, typically containing 128-512 elements [30]. However, the linear configuration gives a narrower field of view than other array shapes, leading to a lower lateral resolution. Curved arrays consist of transducer elements arranged in a bent shape. This curved shape allows for better focusing of the ultrasonic beam. This feature enables the use of the array in applications where imaging or treatment must be performed around a central point, such as eye or transcranial ultrasound imaging. At the same time, this shape introduces additional complexity to the fabrication and the electronic beam control algorithms.

Two-dimensional (2D) matrix arrays are considered to be favorable for focused beam formation compared to linear and circular arrays, especially when using phase-controlled delay techniques. It is also adapted to a variety of imaging modalities and transmission needs, and has numerous applications in medical imaging and therapeutics. It allows for better control of the steering and focusing of the ultrasound beam, enabling dynamic and precise beam control both horizontally and vertically. Most notably, the 2D Matrix Array has the highest element density of the above listed configurations within the same area. For this work, generating the highest possible sound pressure with miniaturized transducers requires the highest possible element density. It is also possible to realize features such as multi-frequency and multi-layer arrays by independently controlling different parts of the elements or by using elements of different sizes.

### 2.4.2.  2D Phased array
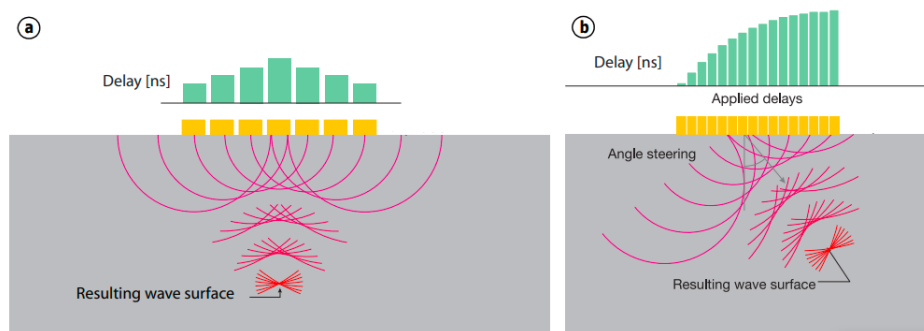


**Figure 2.7:** Schematic Phased Array Ultrasonics [31]

The basic concept of phased array ultrasound is derived from phased array radar [31]. A phased array transducer consists of a number of independent piezoelectric pillars arranged spatially in an array. Each pillar is called an array element, and each array element can be individually controlled for transmit delay. In axial focusing of a phased array, the acoustic travel distance of each array element to the desired focal point is individually calculated. This process determines the time required for the acoustic beam to propagate from each array element to the focal point. The difference between each element's calculated time and the maximum value yields the delay value for each array element. The focusing and deflection diagram of the phased array is illustrated in Figure 2.7. Figure 2.7 (a) represents the acoustic beam focused on the axis, while Figure 2.7 (b) illustrates the deflection of the acoustic beam at a certain angle.

### 2.4.3.  Simultaneous TX/RX

In image-guided neurostimulation, the piezoelectric element of the device is divided into two main modules: imaging and transmitting. Based on existing body data, the imaging module sends out ultrasound waves to roughly locate the vagus nerve. The same module then receives these waves, pinpointing the exact nerve location. Using this imaging feedback, the transmitting module emits continuous waves for neuro-modulation. However, the imaging module must persistently track the target location since the nerve's position can shift due to muscle movements or breathing. The transmitting module ensures consistent and effective neuromodulation by continuously updating the vagus nerve's position based on this feedback.

Since imaging relies on receiving a pulse wave, while modulation utilizes a continuous wave, imaging cannot function based on the reflected wave sent by modulation. The two must operate at different frequencies. Frequent partitioning and circuit design can achieve piezoelectric transducers achieving simultaneous imaging and neuromodulation in the same array. This technique is called dual-frequency transducer arrays [32]. Different functional array elements in the transducer array require different center frequencies. This can be achieved by using different piezoelectric thicknesses.

It is important to note that ultrasonic waves of different frequencies do not interact with each other when propagating in the same medium. This is because they are linear waves and follow the principle of linear superposition. The frequency of an ultrasonic wave is determined by the frequency of its emitting source or vibrating body. When waves of different frequencies propagate simultaneously, they maintain their respective waveforms and amplitudes and do not interfere with or affect each other.

Research findings with similar objectives have already emerged in recent years. Pashaei et al. designed an ultrasound patch with separate transmitters and receivers for image-guided vagal modulation [33]. The design utilizes a flexible printed circuit board that integrates two independent linear arrays. A 64-element linear PZT array used for imaging has a center frequency of 5 MHz, while an 8-element linear PZT array working at 1.3 MHz is used for modulation. The modulation and imaging array widths were 0.94 cm and 4.46 cm, respectively. The target depth of focus for the arrays was 10 mm to 20 mm to give margin to localize and modulate the vagus nerve. Due to limitations in array element count and emission frequency, the actual depth of focus was limited to 5 mm. Nerve localization was achieved using known anatomical landmarks and the HLL algorithm. Since the purpose of image guidance is to continually modify the focus point and focus it on the vagus nerve based on human activity, high-quality images are not required, and the goal is to maximize nerve stimulation pressure.

### 2.4.4. Array Configuration Selection In this work

This research aimed to develop a compact neck patch for image-guided neuromodulation, focusing on creating a small-sized wearable array. This array was designed to effectively reach the desired depth of the vagus nerve and generate adequate sound pressure to meet clinical needs.
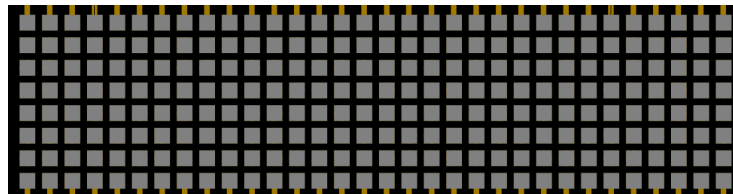


Prototype 1. Single Frequency Rectangular 2D Array
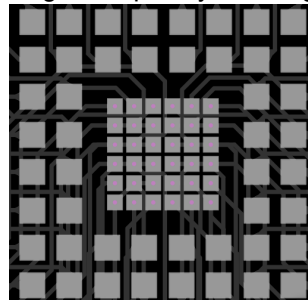


Prototype 2. Dual-Frequency 2D array

**Figure 2.8:** Selection of array configurations for two prototype designs.

To maximize the number of elements and the effective area within an allowable range, a 2D array configuration was adopted, given its superior component density within the same area. This configuration also offered

enhanced flexibility in focus steering, enabling more precise localization of the vagus nerve. This configuration also offers enhanced flexibility in focus steering, enabling more precise localization of the vagus nerve. The schematic of the first prototype, as depicted in Figure 2.8, showcases a rectangular array, with each element serving as a transceiver (TX/RX). While a square array might provide optimal focus compared to a rectangular one, this shape was chosen to integrate as many elements as possible onto a single board. The goal is to have a maximum number of active elements generating ultrasonic waves. This design decision is tied to considerations regarding the board design, which will be elaborated on in greater detail in section 3.4.

The design of the second prototype is shown in Figure 2.8. Dual-frequency arrays were incorporated into the design to address simultaneous imaging and stimulation needs. Given that the main goal is neuromodulation, the design must prioritize high frequencies and larger area stimulation regions with more elements. The imaging area can be smaller because its purpose is to localize the stimulation site and does not require high resolution. comprises an inner square array surrounded by a peripheral square array. In our work, the internal array operates at a high frequency and is used for stimulation, while the external array, operating at a lower frequency, is dedicated for imaging purposes. The selection of frequency, the number of components, and the array size are still intricately related to the capabilities of PCB board manufacturing, which will be elaborated in the following chapter.

## 2.4.5. Parameter Selection for the Transducer Array

The design of transducer parameters is critical. Factors influencing the acoustic beam characteristics include the number of transducer elements, the spacing between these elements, and the width of the elements.

The primary consideration is the target frequency of the transducer. In a thickness-mode piezoelectric transducer, the resonant frequency is related to the thickness of the piezoelectric material. Thinner materials yield higher resonant frequencies, while thicker materials yield lower frequencies. The equation for calculating the necessary thickness based on the desired frequency is given below.

$$t = \frac{V}{2fr}$$

(2.11)

This study used commercially available piezoelectric materials, offering a range of thickness options corresponding to different resonant frequencies.

The selection of array parameters begins with an understanding of the geometry parameters of the 2D array.
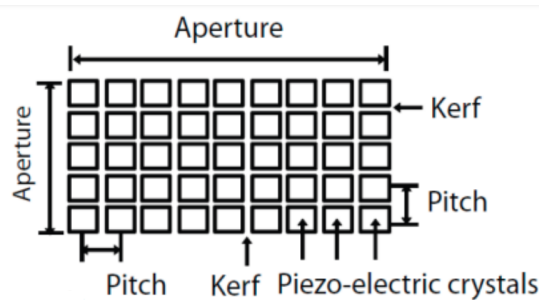


**Figure 2.9:** Geometry Parameters of the 2D Array [34]

- Aperture
  As illustrated in Figure 2.9, the aperture refers to the effective area of the transducer responsible for transmitting or receiving ultrasound. For 2D arrays, the aperture encompasses the total length and width of all elements operating concurrently. It is crucial for the aperture size to be considerably larger than the wavelength to facilitate a high-quality beam transmission.
- Pitch
  The array pitch, or the distance between the center points of adjacent elements in an array, is another

critical parameter. A smaller pitch often results in higher resolution and superior focusing capabilities but can also amplify the complexity of fabrication and electrical connections.

The key rule regarding the pitch of an array is to ensure it is equal to half the wavelength of the ultrasonic signal. This is aimed at minimizing the harmful effects of grating lobes. Grating lobes are side beams that appear next to the main beam. This occurs because the neighboring signals will overlap in frequency. These grating lobes may interfere with the primary beam and affect localization and resolution. As the pitch is close to the half wavelength of the signal, the phase difference between neighboring signals is 180 degrees, and the interference will be canceled out between them, thus eliminating the grating lobes.

- Kerf
  Kerf refers to the spacing between individual elements in an array. It represents an inactive area where the material is removed during fabrication to establish acoustic isolation between the elements.

- Volume fraction

$$VF = \frac{\text{Pillar width}^2}{(\text{Pillar width} + \text{kerf})^2} \tag{2.12}$$

The volume fraction is the ratio of the area of the element that can work to the total area of the aperture [35]. A larger effective piezoelectric area, achieved by having a smaller kerf, leads to a higher ultrasonic density across the transducer.

- Aspect ratio
  The aspect ratio (AR) represents the ratio of the pillar's height to its width. To prevent mode coupling and ensure that keff dominates, it is necessary for the aspect ratio to be higher than three [36] [37]. Therefore, the preferred characteristics are high aspect ratios and geometrical shapes of high and thin columns.

- Focus Spot
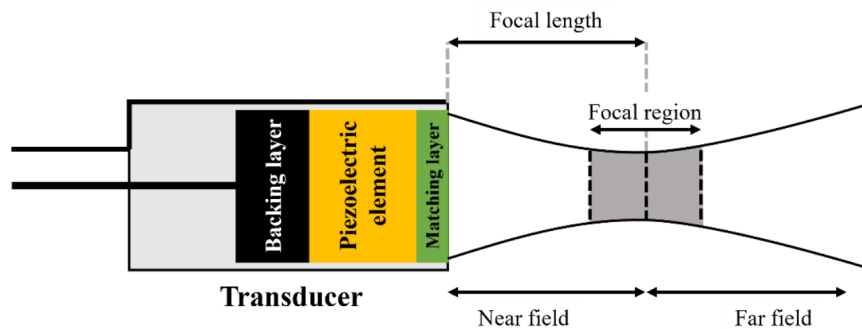


**Figure 2.10:** Different Ragions of Ultrasound Beam [38]

At each location of the sound field, the sound pressure is the sum of the contributions from all of the transducer elements.

The ultrasonic beam can be divided into two regions: the near-field and far-field regions. In the near-field region, the beam has the profile of a converging beam. In this region, the sound pressure repeatedly reaches the maximum and minimum values several times. The end of this

region is the position on the axis where the maximum sound pressure value last occurred. The beam begins to diverge in the far-field region, and the ultrasound intensity gradually decreases.

The transition point between the two regions is the maximum signal intensity position, also known as the focal region. The distance from this position to the probe surface is N, the near-field distance. The near-field distance N represents the natural focal length of the probe. It can be calculated for square or rectangular wafers commonly used in phased array inspection using the following equation[39]:

$$N = \frac{kL^2}{4\lambda} \tag{2.13}$$

Where k is the aspect ratio constant, and L is the length of the element. The aspect ratio constant is calculated based on the ratio of the lengths of the short and long sides of the transducer element or aperture, as indicated in table 2.3.

| Ratio of shorter/longer side | aspect ratio constant k |
|:---:|:---:|
| 1.0 | 1.37 |
| 0.9 | 1.25 |
| 0.8 | 1.15 |
| 0.7 | 1.09 |
| 0.6 | 1.04 |
| 0.5 | 1.01 |
| 0.4 | 1.00 |
| 0.3 or smaller | 0.99 |

**Table 2.3:** Values of Aspect Ratio Constant

<div style="text-align: right; font-size: 3em;">3</div>

# Development of 2D Array Transducer

This chapter describes the process of designing and developing a two-dimensional array transducer. This includes the selection of array parameters, the introduction and final selection of different array shapes, and the listing of fabrication methods and their selection according to the requirements of this thesis.

In the first part, different shapes of 2D array transducers are studied. Their characteristics, as well as their advantages and limitations, are presented. The second part describes the fabrication methods used in different studies to fabricate 2D array transducers. The various dicing techniques, electrical interconnection methods, and packaging options are described in detail. Finally, the challenges of achieving the desired performance characteristics and optimizing the fabrication process are addressed, and trade-offs are made to determine the fabrication methods.

The exploration of transducer fabrication considerations led to the finalization of the array configuration and fabrication method selected for this work. In this study, achieving high-quality vagus nerve stimulation was challenging regarding transducer prototype shape selection. A well-optimized shape maximizes the spatial resolution, beam-forming capability, and overall performance of the transducer. Higher frequency piezoelectric materials and larger area arrays can provide excellent stimulation range and pressure. Better electrical interconnections allow for stable device operation.

## 3.1. Array Fabrication Technology

### 3.1.1. Dice and Fill

Dice and Fill are one of the most commonly used and well-established processes to fabricate piezoelectric transducer arrays with an operating frequency of less than 15 MHz. It involves cutting the piezoelectric material into separate elements and filling them with an insulating material to maintain spacing and electrical isolation between them.

The following schematic Figure 3.1 is a complete description of the Dice and Fill process.As shown in Figure3.1 (b), it begins with a piezoelectric wafer, which is diced in two perpendicular directions using a mechanical dicing saw. This dicing process cuts out separate elements, usually regular shapes. The accuracy and size of the cut depend on the desired array structure and design requirements. Next, fill the kerf with an insulating material, usually epoxy, as shown in Figure3.1 (c). The purpose of a filling is to maintain spacing between components, prevent electrical interference between neighbouring components, and, most importantly, provide structural support and stability. It undergoes a curing process by heating the epoxy to make it rigid, thus creating a strong and long-lasting bond between the component within the filler material.

<div style="text-align: center;">19</div>

After that, the unwanted bottom piezoelectric material and top epoxy were removed by lapping, as shown in Figure3.1 (d) (e). Only the bare piezoelectric columns were retained, and the desired thickness of the composite sample was achieved.
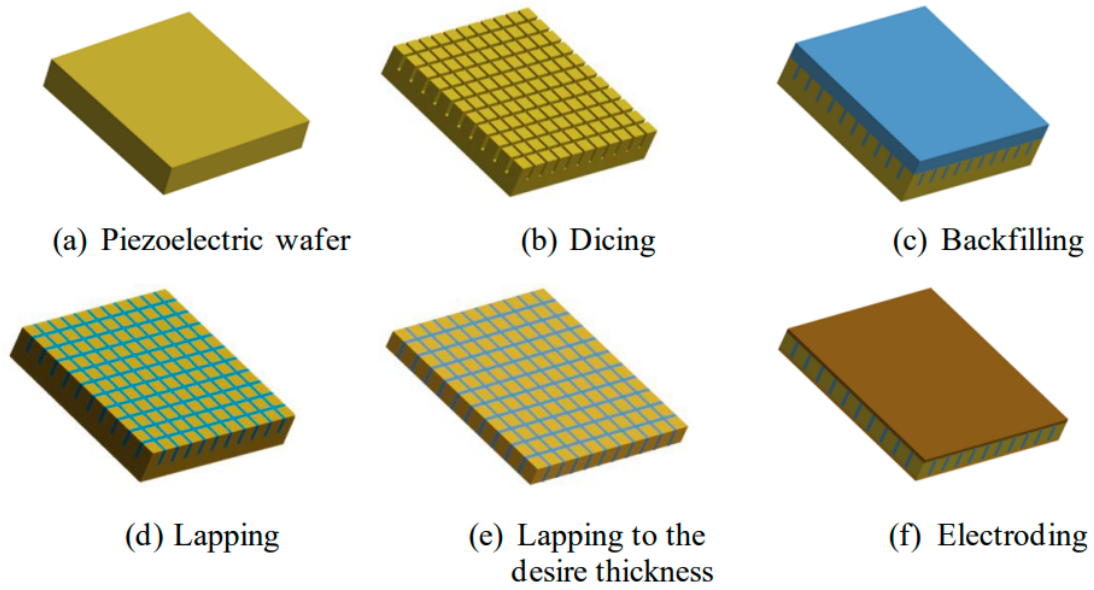


**Figure 3.1:** The Standard Dice and Fill Process [40]

The final step is plating. Electroplating is depositing a thin, uniform layer of metal onto the bare surfaces of the cut elements and filler materials. Electroplating provides a protective layer, but more importantly, the deposited metal layer provides the device's conductivity. Piezoelectric materials must have upper and lower electrodes to realize the piezoelectric effect.

The Dice and Fill process allows the fabrication of independently controlled arrays of piezoelectric elements with tightly spaced alignments. In the standard Dice and Fill process, there are various dicing schemes.

**Horizontal-Vertical Dice and Fill**
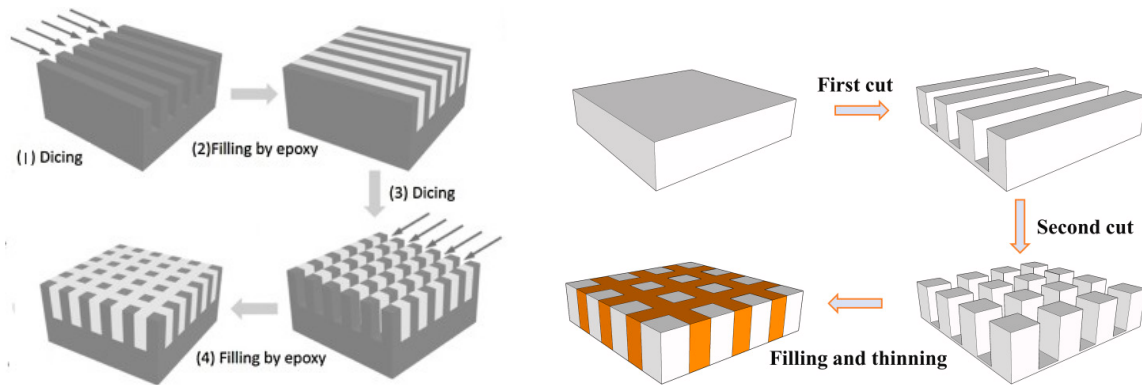


**Figure 3.2:** (a) Horizontal-Vertical Dice and Fill [41] and (b) Cross-Dice and Sequential Fill [42]

Traditional fabrication often adheres to the horizontal-vertical dice-and-fill method as delineated in Li et al.'s work [41]. As illustrated in Figure 3.2 (a), the process begins with the dicing of the piezoelectric material

into rows of elements in one direction. These kerfs are subsequently filled with an insulating material. Following this, the material is diced in a direction perpendicular to the initial cuts, and the resultant gaps are filled with the insulating material. This procedure ensures controlled spacing and alignment of the diced pillars, thereby maintaining the electrical isolation between the elements.

**Cross-Dice and Sequential Fill**

An alternate dicing technique, termed the cross-dice and sequential fill method, is outlined in Ma et al.'s study [42]. As represented in Figure 3.2 (b), the procedure initiates with a cut in one direction, succeeded by a second cut made perpendicular to the first, and culminates in the filling step. This technique offers an expedited production process, potentially increasing manufacturing efficiency.

**Triple-Step Subdivision Dicing**

For composites with high aspect ratios or highly brittle single-crystal materials, the elements are too thin to be easily flushed away by the flash water of the dicer during the dicing process, resulting in low element integrity. A modified dice-and-fill method can also be used to dice the frame before subdividing [43]. The process is demonstrated in Figure 3.3. The fabrication process involves an intricate, three-step dicing approach. Firstly, we perform dicing at four times the final target pitch and fill the resulting kerfs with epoxy. Due to the lower aspect ratio of the array at this stage, the diced pillars can stand independently. Next, the composite panel is diced again at the same pitch and depth, resulting in the insertion of epoxy right in the center of each pillar. This effectively subdivides each pillar into four equal areas. The width of the pillar at this juncture is twice the target pitch. In the final step, we further dice the center of each element into four equal parts to achieve the final target pitch. This unique strategy improves the structural stability of the components by maintaining specific gaps during the dicing process, ensuring the elements remain intact and functional.
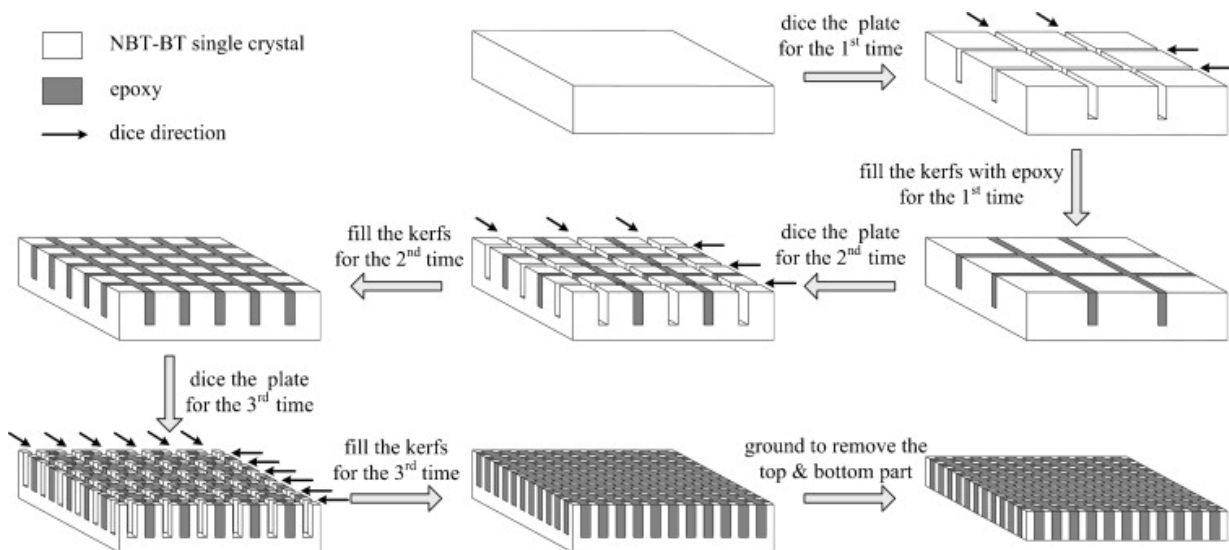


**Figure 3.3:** Triple-Step Subdivision Dice and Fill [43]

**Interdigital pair bonding**

In the prior section, the width of the kerf was determined by the width of the dicing saw kerf. Typical minimum widths of current dicing saw kerf are about 10 µm. However, some applications require high-frequency and high ceramic phase volume fractions to obtain higher relevant, effective physical parameters, such as dielectric constant and longitudinal sound velocity. A fabrication called Interdigital pair bonding is introduced for this propose [44]. The fabrication process of this technology involves several steps. It begins with four plates of piezoelectric material, all of the same size, divided into two groups. Within each group, two samples are diced horizontally. The kerf is broad, slightly larger than its element width. One of

the two samples was flipped, with its component rows aligned to the kerf rows of its other, and spliced. The spliced assemblies had minimal gaps filled with epoxy resin to create the desired separation between them.
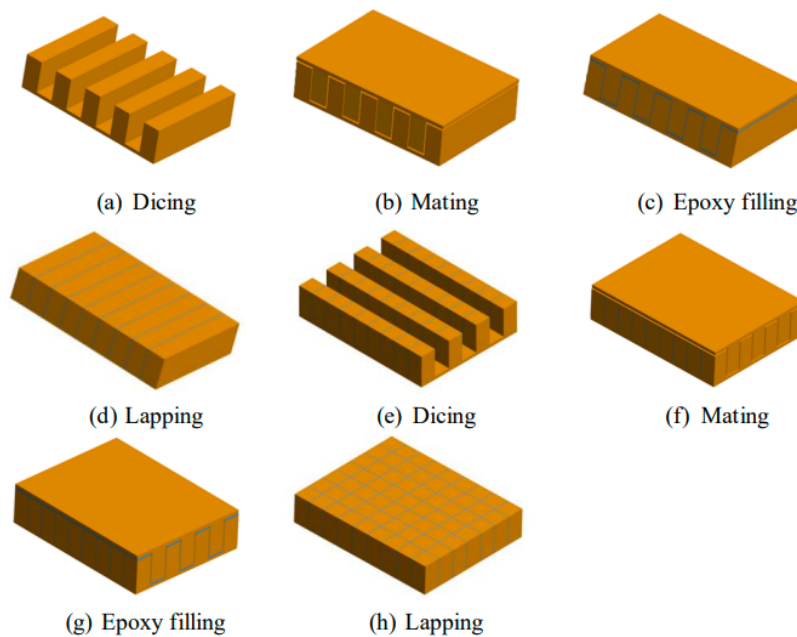


**Figure 3.4:** Interdigital Pair Bonding [44]

After the epoxy was fully cured, the samples were ground to expose the slices and form a 2-2 composite structure. Next, the two pieces of the 2-2 composite are cut perpendicular to the initial cut direction. These cut pieces are then paired using the same method, filled with epoxy, and lapped to create the final 1-3 structure. This process reduces the cutout size between the plates to 4-12 µm. While this fabrication method can be time-consuming and challenging for mass production, it offers high piezoelectric material volume fractions, ranging from 81.5% to 90%. Additionally, the small notch size helps to prevent spurious modes, allowing the 1-3 piezoelectric material to resonate in a pure fundamental thickness mode.

**Laser Dicing**

Laser micromachining is a potential solution for fabricating high-frequency 1-3 composite materials, especially when kerf is less than 10 um. To prevent the laser heat generation that depolarizes the material, a cold ablation process method was applied by lv et al. [45]. The metal electrode was first coated on the surface, then repeatedly etched at very low amounts (5%) each time using a picosecond ultraviolet (UV) laser, then finally, epoxy resin was filled into the incisions of the etched PMN-PT.

**Micromachining**

Micromachining techniques such as photolithography and laser processing are widely used in micro-electromechanical systems (MEMS) technology. Since 2001, they have also been used to fabricate high-performance single components and arrays of piezoelectric composites, especially 1-3. A significant advantage of the micromachining approach is achieving extremely fine notches, typically in the 5-10 µm range, for micro-ultrasonic (µUS) arrays. This fine separation of columns has the advantage of reducing column chipping and microcracking, which are common challenges in dice-and-fill methods when working with single-crystal materials. One example is the combination of photolithography and deep reactive ion etching (DRIE) [46]. As shown in Figure 3.5, a positive photoresist is deposited as a sacrificial mask using photolithography, including photoresist coating, baking, UV exposure, and stripping. A metal layer is used as a hard mask and is electroplated to replicate the sacrificial mask pattern. After removal of the

photoresist, the sample is subjected to DRIE to form a bristle block structure. Subsequent steps include epoxy filling, grinding, and plating to complete the composite material.
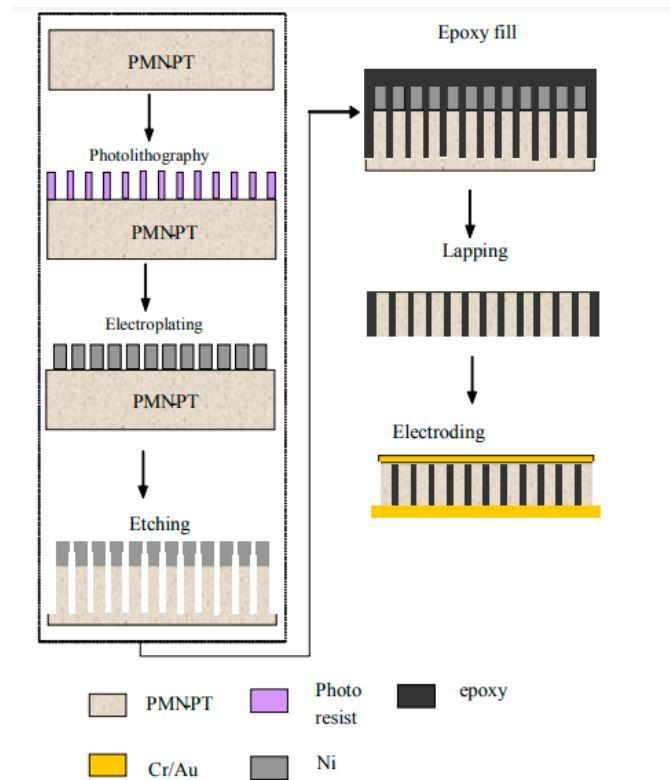


**Figure 3.5:** The Micromachining Techniques [46]

## 3.1.2. Flip-chip Dicing

The conventional Dice-and-fill method involves dicing an array of piezoelectric material of a specific thickness without dicing through it. After that, the material is lapped from the back side, removing the uncut portions until the desired thickness is achieved while simultaneously exposing all the pillars. The piezoelectric pillars are surrounded by epoxy, which acts as a 1-3 composite. In the final integration step, the 1-3 composite is aligned as a whole block.

Costa et al. presented an innovative and efficacious approach for directly integrating piezoelectric materials onto corresponding chips or PCBs, where they can be diced and processed [47]. Initially, the factory-affixed electrode layer on both sides of the material is eradicated. The electrode contact shape, which mirrors the pads on the chip, is directly coated on both sides of the piezoelectric block via lift-off photolithography and e-beam evaporation, as depicted in Figure 3.6 (i), (ii). Subsequently, the PZT5A wafers were pre-diced into 2D arrays from the side oriented towards the chip, with merely 20% of the thickness diced off, as illustrated in Figure 3.6 (iii). Pre-dicing serves to avert potential damage to the chip's surface. If the piezoelectric blocks were directly attached to the chip and diced to the block's thickness, the dicing blade would level with the chip's surface, making it susceptible to damage. Subsequently, the CMOS chip and PZT-5A were aligned with sub-micron precision and bonded via an anisotropic conductive film, with the PZT5A's pre-diced surface facing the CMOS chip surface, as depicted in Figure 3.6 (iv). Next is the definitive cut, in which the PZT5A is diced from the top, the blade traversing 90% of the initial thickness. This procedure generates discrete PZT5A pillars without inflicting damage on the CMOS chip surface. The 10% allowance further guarantees that all pillars are distinct and adequately diced. The column kerf is suffused with an epoxy resin in the final stage.

**Figure 3.6:** Fabrication Flow of Flip-chip Dicing Method

### 3.1.3.  Interconnect

**Anisotropic Conductive film**

Anisotropic Conductive film is an alternative to solder interconnects in electronic packaging and is often used in flip-chip packages. ACF is characterized by providing unidirectional conductivity in the vertica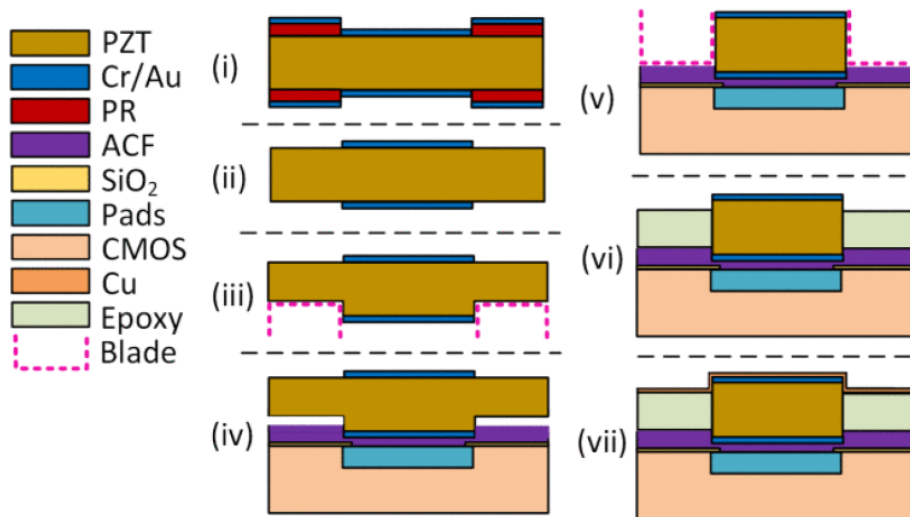l direction (Z-axis). Lateral connectivity in the X- and Y-axis directions is minimized or completely blocked. This feature is achieved by the fact that the body of the ACF is an adhesive, which has conductive particles with a low volume load, typically 5-20% volume fraction.

The ACF application method is described as follows. First, place it between two electrode surfaces. For this work, this corresponds to the electrodes on the surface of the piezoelectric material and the bottom PCB conductive plate. When not being used, the conductive particles are uniformly distributed in the resin, as shown in figure 3.7. Applying heat and pressure makes the resin soft, tacky, and flattened until the thickness is pressed to the same diameter as the conductive particles. At this point, the conductive particles stuck on the surface of the upper and lower electrodes realize their electrical interconnection. The conductive particles outside the electrode surfaces are not connected and are isolated between the resins, achieving lateral electrical isolation.

**Isotropic conductive adhesive**

Conductive silver epoxy is an isotropic conductive adhesive (ICA). It consists of silver flakes and powder suspended in an epoxy binder. It is a metal particle adhesive that conducts electricity. It can be placed on many different surfaces, whereas solder cannot.  This is an excellent advantage for parts that are more temperature sensitive. Silver epoxy offers a relatively low-temperature curing option compared to soldering to prevent heat damage to circuit components. During manufacturing, silver epoxy connects the component pads patterned on thin layers of piezoelectric material, and the copper wires are soldered to the external connector.

**Wire Bonding**

Using fan-out pads for wire bonding is a feasible method for interconnecting array elements . Fan-out wire bonding is primarily utilized for bonding linear arrays. However, it can also be applied to 2D arrays that have a smaller number of elements. This approach involves using silver wires to establish connections between the transducer's solder joints and the circuit board. Fan-out wire bonding can be effectively employed for CMUT arrays with limited components and linear arrays [48]. An example of this interconnection technique is demonstrated in Figure 3.8. Fan-out wire bonding has specific drawbacks that limit its applicability in certain scenarios. It is not suitable for microfabrication processes that involve a large number of components

and extremely small sizes. Also, when assembling linear arrays with components and interconnects on opposite sides, an additional adhesive is needed to secure the interconnects. This additional adhesive layer can introduce uneven surfaces, potentially affecting image processing accuracy. Non-uniform surfaces may lead to variations in acoustic coupling and could impact the overall performance of the array.
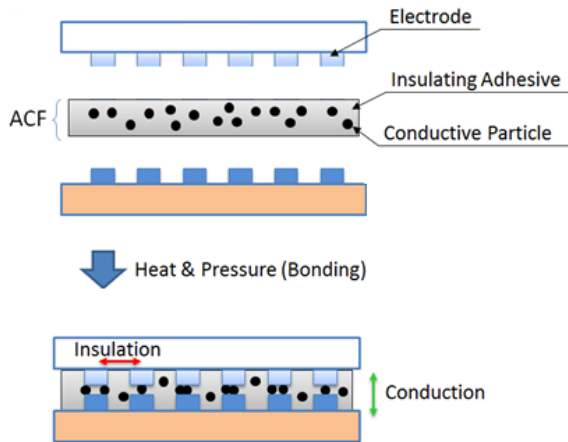


**Figure 3.7:** ACF Bonding [49]
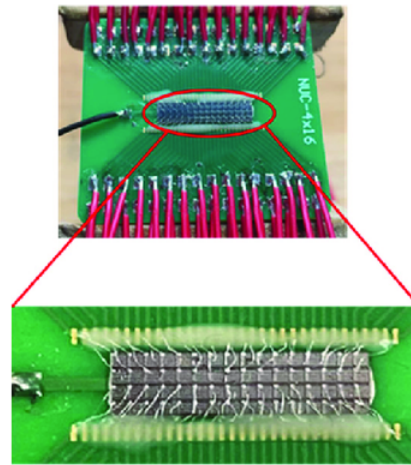


**Figure 3.8:** Wire Bonding [48]

### 3.1.4. Encapsulation

Encapsulation layers are essential in medical ultrasound applications as they serve multiple purposes. These layers provide insulation, waterproofing, and extension of the device's lifespan, making them mandatory in such applications. The encapsulant should be biocompatible and has a minimal impact on output pressure. Polymers are frequently employed as encapsulation materials owing to their mechanical attributes.

**PDMS coating**

Polydimethylsiloxane (PDMS) is an excellent choice. It is biocompatible and has an acoustic impedance similar to human tissue (1.5 Mrayl). As a softer elastomer interfacing the transducer and tissue, it can preclude tissue damage.
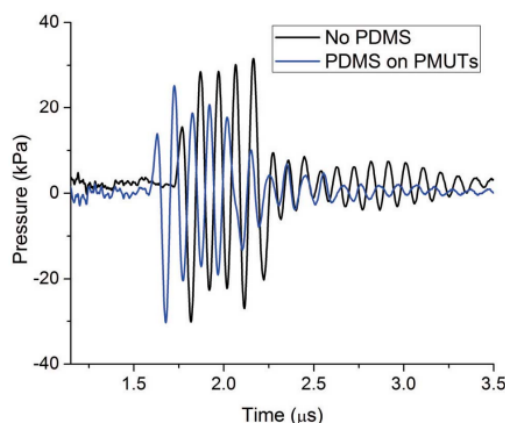


**Figure 3.9:** Impact of PDMS Encapsulation on Pressure Amplitude [50]

In a study undertaken by Y. Lu et al., an evaluation was performed to investigate the influence of a PDMS

layer on the output pressure of a 9x9 PZT PMUT array [50].  A PDMS layer of 250 µm thickness was applied to one set of arrays while another set remained devoid of any coating. The experimental outcomes, as represented in Figure 13, indicated that the PDMS encapsulation exerted only a minimal effect on the pressure amplitude. The slight discrepancy in the arrival time of the acoustic wave can be attributed to the variant sound speeds in PDMS and the surrounding fluid. This inference indicates that PDMS can serve as a protective encapsulation without detriment to the performance of the transducers, thus classifying it as an acoustically transparent material.

**Parylene coating**

Parylene can be used to encapsulate medical implants such as stents, pacemakers and nerve probes because of its good isolating properties and biologically inertness [51].  The thickness of the Parylene layer is precisely controlled by a vapour phase deposition procedure to ensure consistency and uniform coverage feasibility [52].  This coating process is both efficient and stable and is suitable for preparing large areas for layer deposition. The acoustic impedance is approximately 2.7 to 3.7 Mrayl, which is in the middle of the range between that of water and that of piezoelectric materials [53]. It is worth noting that all encapsulant experience a reduction in resonant frequency due to increased sealing. Thus, there is a trade-off between maintaining a thin coating and ensuring adequate hermeticity [54].

## 3.2. Design Considerations and Final Choice

This thesis aimed to streamline the fabrication process to ensure consistency and efficiency in Standard Operating Procedures (SOP). We prioritized creating a process that could be easily replicated in other labs. Given this emphasis on simplicity, we decided not to use micromachining, as it would add undue complexity to the procedure and extend the manufacturing cycle time. Additionally, the transducer array did not require high frequency. As a result, mechanical cutting was sufficient for achieving the necessary kerf width for this project, negating the need for laser cutting. While laser cutting is commonly utilized for precise incisions in high-frequency settings, its single-cut depth is relatively shallow, making it unsuitable for thicker low-frequency piezoelectric materials.

Given our choice to utilize the mechanical dicing method, several steps from the traditional 'cut and fill' method were omitted.  For instance, instead of filling with epoxy to enable the piezoelectric pillar to vibrate more effectively and generate a higher ultrasonic density, we opted for air-filling, albeit it is more challenging to implement. Steps like grinding and polishing post-filling were also excluded. Additionally, our collaborative manufacturer offers a range of piezoelectric materials with thicknesses commonly used in experiments, allowing us to purchase materials that match the required frequencies directly. As for the final electrode plating, the piezo sheets provided by the manufacturer come pre-plated with metal electrodes, which meets the needs at the prototype stage.

Given our specific criteria, flip-chip dicing emerged as the most viable and suitable option. The merit of this technique lies in its straightforwardness and precision, ensuring that each piezoelectric element aligns accurately with the contact pad beneath it. Most notably, for the low-frequency, thick piezoelectric material utilized in this work, the thickness of the piezoelectric material was already approaching the exposed thickness of the dicing saw blade. Pre-dicing a portion from the bottom could enhance the smoothness of the upper part's cutting kerf and concurrently safeguard the blade.

For this study, the option of no kerf filler was selected.  While kerf fillers are essential for the dice-and-fill method, the flip-chip technique provides greater flexibility.  It must be acknowledged that the absence of filler support can complicate the dicing process. Precisely, cutting in alternate directions may render the pillars more unstable and prone to collapse, mainly when the aspect ratio is high. However, this challenge can be mitigated through optimization of the cutting process. A key advantage of forgoing a filler is the resultant enhancement in performance. Wang et al. analyzed the impact of various kerf fillers on overall performance through a mathematical model [55]. Figure 3.10 displays the aspect ratio dependency of keff for PMN-0.3PT and PZT with differing types of kerf fillers, with the aspect ratio designed as 4 in this study. Compared to various kerf-filling materials and air filling (i.e., no filling), PZT and PMN-PT exhibit the largest keff when unfilled. This implies the most effective generation of ultrasonic waves.
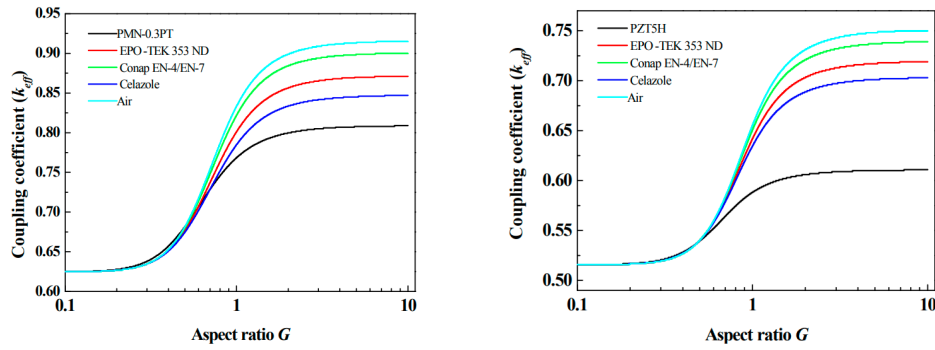
**Figure 3.10:** The Aspect Ratio Dependency of keff for PMN-0.3PT and PZT with Differing types of kerf Fillers

Concerning interconnections, ACF was selected. This decision was based on the necessity for the 2D array to accommodate as many elements as possible while maintaining electrical isolation between each one. Although there are various ACF options, typically made from a thermosetting resin, this work involved PM-PT, a material known for its limited resistance to high temperatures. Therefore, an ACF option suitable for room-temperature interconnections was employed for this study. The ICA is used to connect the ground plane metal situated at the top of the piezoelectric materials. This adhesive has conductive properties in all directions and is capable of creating a reliable and effective electrical connection

Parylene was chosen as the encapsulation material. One of the most compelling advantages of Parylene is its ability to create highly uniform and conformal coatings through the Plasma Enhanced Chemical Vapor Deposition (PECVD) process. This ensures excellent coverage, even on complex geometries, edges, gaps, and recesses. Given the resources at our disposal, this process allows for precise control and repeatability in the coating process.

## 3.3. Customized PCB design

This chapter delineates the design specifics of customized PCBs for the integrated transducer array. Designing the transducer prototype necessitates a delicate balance between shape selection and manufacturing feasibility, ensuring the selected form is effectively realized during the actual fabrication and assembly process. The preeminent consideration pertains to the manufacturing capacity of the custom PCB. Each transducer element requires connection to PCB pads for autonomous control in this endeavor. Thus, the configuration, dimensions, and interstitial spacing of the pad arrays on the custom PCB must mirror those of the transducer arrays. An essential directive in phased array design is maintaining component spacing at or below the half-wavelength spacing to avert any potential interference from grating side lobes affecting the beamforming performance. This dictates that the PCB pad array must adhere to the same rule, presenting an upper limit to the manufacturer's precision, specifically regarding the minimal pad spacing and line width. Consequently, the minimal pitch of the transducer array is restricted by the maximum accuracy capabilities of the manufacturer.

The design of the PCB employs Altium Designer. The first prototype iteration aims to fabricate a conventional 2D array by optimizing the manufacturing process to yield a successful and comprehensive prototype. At the same time, a comparative analysis of the performance of two different piezoelectric materials, PZT and PMN-PT single crystal materials, is planned. The second prototype iteration aims to construct a dual-frequency array, potentially capable of simultaneous imaging and stimulation.

Phased-array transducers integrated with PCBs for prototyping offer several advantages over the design of specialized chips. The main benefit is the potential for a reduced development cycle. Developing a phased array transducer chip involves a lengthy research, design, and manufacturing process. In

contrast, PCB prototyping and testing can be executed within a few months, accelerating the iteration and development of phased array systems. Moreover, it is a more cost-effective approach. For low-volume prototyping, the manufacturing cost and complexity of PCBs are significantly lower than chips. Finally, programmability and flexibility are key advantages. PCBs can be readily interfaced with programmable platforms such as Verasonics, enabling the testing of the ultrasonic beamforming capabilities of fabricated phased arrays for flexible optimization of the performance and functionality of phased array sensors.

### 3.3.1. Design Consideration and Manufacturing Feasibility Trade-offs

During the prototype stage, we encountered the challenge of finding an optimal balance concerning the PCB manufacturing capabilities. The density of the elements in the design is contingent on the minimum spacing that can be achieved in the PCB and on effective routing to ensure each element connects to an individual trace. However, increasing the number of rows would necessitate the use of more layered PCBs. While technically feasible, this solution presents a significant cost increase and additional manufacturing complexities. Not many manufacturers are equipped or willing to produce such highly layered PCBs. Therefore, in this early prototype phase, we needed to strike a compromise between design sophistication and practical manufacturing considerations.

**Manufacturing Feasibility**

After thoroughly evaluating both process capability and cost, PCBway was chosen as the first PCB prototype manufacturer, and Beton tech as the secondary PCB manufacturer. Their advanced manufacturing capabilities are summarized in the table below. The initial version was an 8-layer rigid board, while the second prototype was a 4-layer flexible board. This decision was based on cost considerations. Given that the rigid PCB process becomes difficult and expensive at 10 layers or more, and the flexible PCB process is inherently challenging and costly, the final compromise was a 4-layer design based on the performance requirements of this work.Compared to rigid PCBs, flexible PCBs can achieve a smaller minimum alignment width and spacing, thanks to their material properties and manufacturing process. Flexible PCBs use polymer materials as substrates, while rigid PCBs utilize FR4 materials. The former has a smaller dielectric constant, allowing for narrower alignments and higher line density. Additionally, flexible PCBs can realize finer lines using thinner copper foils and higher precision lithography processes.

|  | PCBway | Beton Tech |
|---|---|---|
| PCB type | HDI PCB | Flexible PCB |
| Number of Layers | 2-64 | 1-30 |
| Minimum track line | 100um-inner and 100um-outer | 50um-inner and 50um-outer |
| Minimum Spacing line | 100um-inner and 100um-outer | 25um-inner and 25um-outer |
| Laser via hole | 100um(Laser Blind/buried vias) | 50um(Laser Blind/buried vias) |
| Min. annular ring for via | 75um | 50um |
| Min. via in pad size | 250um | 170um |

**Escaping Routing method**

During the prototyping phase, finding the optimal balance between PCB manufacturing capability and component performance presents a significant challenge. The density of the components determines the performance of the transducer, with optimal results obtainable within a specific range. However, practical constraints such as the minimum achievable spacing on the PCB and efficient routing to ensure each element is connected to a distinct trace need to be considered.

The escape routing method for BGAs (Ball Grid Arrays) provides a reference when designing PCB routing. Escape routing aims to route each pad beyond the edge of the device, thus making routing connections easier. A crucial rule in 2D phased array design is that the pitch should be less than or equal to half a wavelength. This needs to consider the feasibility of the PCB manufacturer regarding the minimum trace width/space and pad diameter. According to the standard routing method, if the trace is routed in the same layer as the contact pad, as shown in Figure 3.11 (a) below, the contact pad in the array of the outermost circle (i.e., pads ABC) can be directly fanned out through the alignment. To connect the inner contact pad D, the spacing of pads AB must be double the width of the alignment plus twice the spacing of the alignment. Using the rigid board parameters from PCBway as an example, this results in a minimum pitch of a minimum pad width (250um) plus double the alignment width (100um) plus double the spacing (200um), which totals 550um. According to the formula, this corresponds to a maximum allowable frequency of 1.27MHz, which needs to be higher for this project. This routing strategy also complicates the fanning out of the trace in the more centrally located pad E, thereby limiting the total number of phased array components.
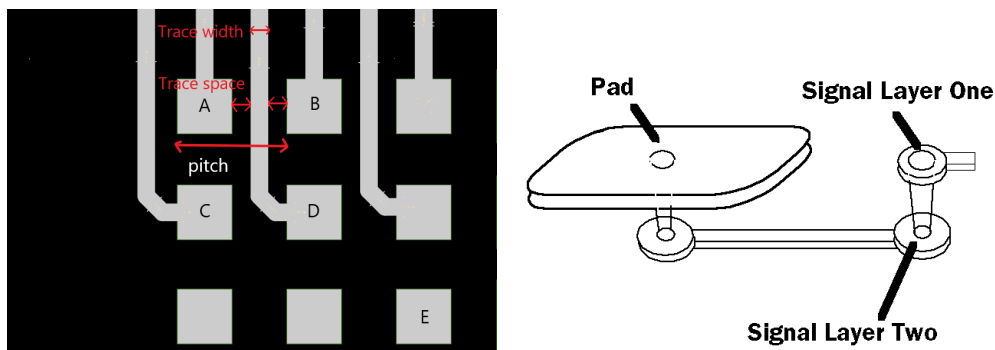


**Figure 3.11:** (a) The Standard Routing Strategy (b) The Via-in-pad Strategy Demonstration

Via-in-pad technology is applied in these high-frequency, high-density applications. This technology involves placing a via directly within the pad of the component, as shown in Figure 3.11 (b). Via-in-pad overcoming the space constraints posed by small pitch arrays, as it negates the need to find space for vias between pads. This approach is particularly beneficial when dealing with the pads located in the center of the array, like pad E in the description. By positioning via holes directly in the pads, traces can be rapidly routed from the first layer to the inter-layer. Within the inter-layer, traces can be extended to the edge of the board. Signals are then exported from the via holes back to the first layer, which can be interconnected with external cables. This strategy frees up space in the original layer for additional components while only routing the necessary wiring, optimizing the use of the PCB's space and design efficiency.

### 3.3.2. Design of the Prototype 1

The first manufacturer permitted a minimum contact pad width of 250um and a minimum pad-to-pad pitch of 100um without an intervening trace. This constrains the minimum pitch size to 350um, corresponding to a permissible emission frequency of 2MHz. The quantity of components in the array is contingent on the number of layers in the stacked PCB. After several wiring trials, it was ultimately decided that the fan-out should proceed from both the top and bottom of the array, with each row of components connected to an inner layer for subsequent fan-out.

**First version**

The first version, as depicted in Figure 3.12 (a), is an 8x8 array. The aperture of the array measures 2.78 mm by 2.78 mm. The top layer of the eight-layer stacked PCB houses the contact pads. The contact pads of the first and eighth rows fan out from the surface using traces. Via-in-pad technology connects six of the layers, along with the bottom layer, to the pads of the second through seventh rows, and this connection serves as a fan-out channel.
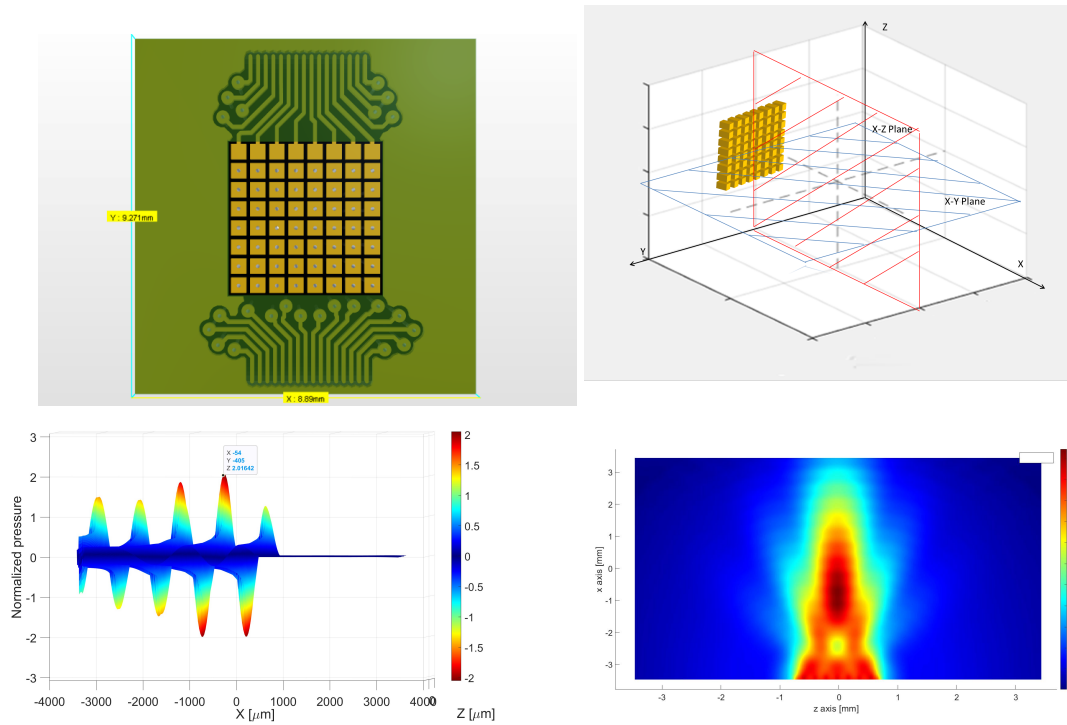
**Figure 3.12:** (a)The First version PCB Layout Visualized in Altium Designer (b)The Positioning of the Transducer Array Within k-wave (c) Intensity of Ultrasound Wave Propagation along the X-Y Plane (d) Beam Pattern Simulation Result on the X-Y Plane (depicted in blue)

In addition to the physical design process, k-wave simulation was employed to simulate the results of a plane wave emission. At the present juncture of the research, plane waves are simulated rather than beamforming, given that the existing experimental setup is not yet prepared to evaluate focused ultrasound, only plane waves. Thus, the adopted simulation strategy harmonizes with the current testing capabilities. As derived from equation (2.11), the projected near-field natural focusing distance for this prototype is 3.44 mm, which aligns with the K-wave simulation result of 3.8mm. This focal distance, however, have not meet the specific requirements of vagus nerve stimulation for our current application. Additionally, a larger aperture housing more active elements can significantly augment the pressure produced, thus stimulating the pursuit of increasing the element count without adding extra layers to the array.

**Second version**

At this point, inner-layer routing has reached its limit, and any further increase in array rows would necessitate a cost-prohibitive expansion of PCB layers. Hence, an alternative approach has been adopted by extending the number of array columns. The second version was engineered through careful circuit routing as an 8x16 array comprising 128 components, as depicted in Figure 3.13 (a). This design doubles the component count from the first version while preserving the same 8-layer PCB configuration.

In the K-wave simulation outcomes, due to the discrepancy in element count between rows and columns, the propagation profile of the ultrasound is unconventional. Thus, wave propagation profiles in the X-Y and X-Z planes have been independently simulated. As evidenced in Figure 3.13 (d), the maximal acoustic pressure point for the rectangular arrangement is not centrally located, but rather dispersed across three distinct points. As derived from equation (2.11), the projected near-field natural focusing distance for this prototype is 5.07 mm. In the K-wave simulation, higher sound pressure is seen from 2mm to 4mm from the transducer. The highest point is around 2.8mm.
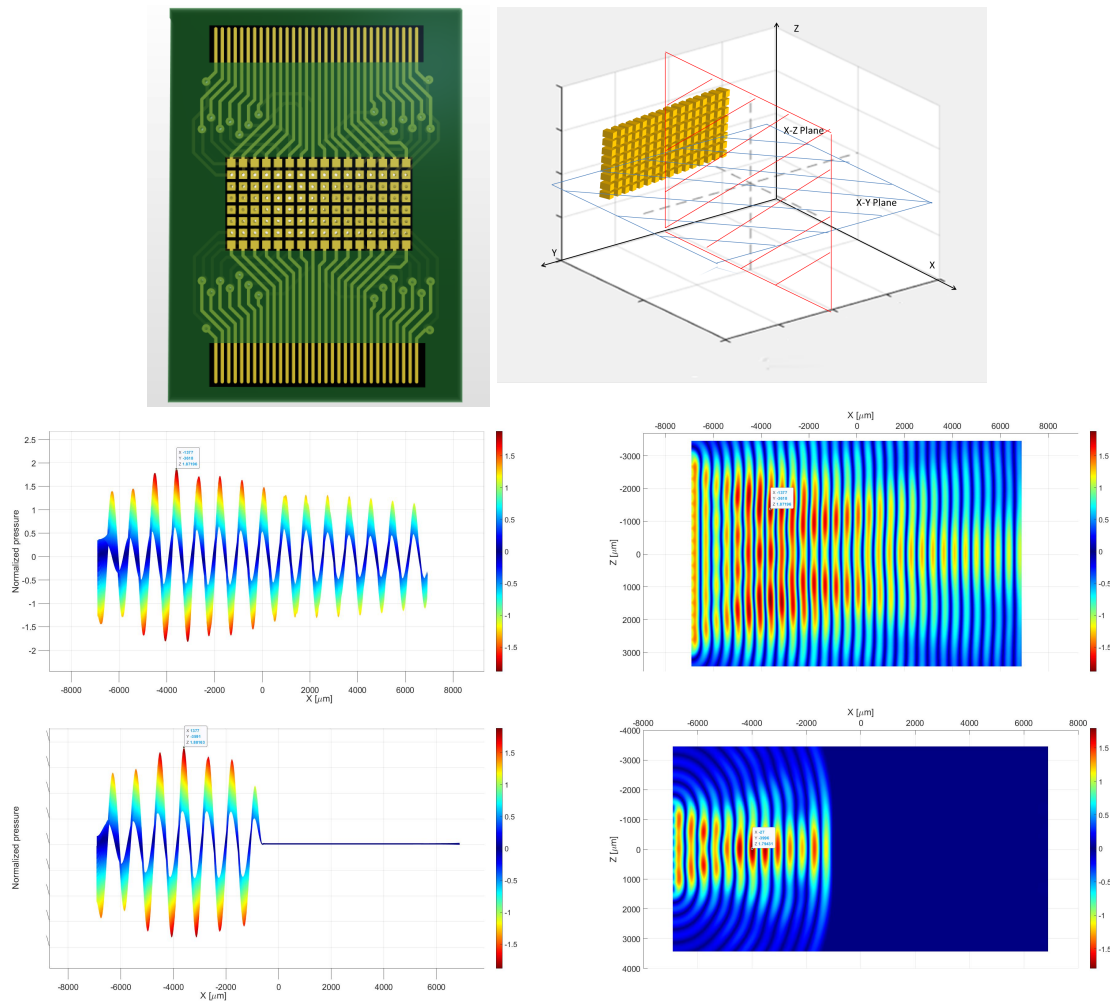
**Figure 3.13:** (a)The Second version PCB Layout (b)The Positioning of the Transducer Array Within k-wave (c) Intensity of Ultrasound Wave Propagation along the X-Y Plane (d) Beam Pattern Simulation Result on the X-Y Plane (depicted in blue)(e) Intensity of Ultrasound Wave Propagation along the X-Z Plane (f) Beam Pattern Simulation Result on the X-Z Plane (depicted in red)

It is feasible to achieve the single and centralized focus beam by electronic control of the phase delay.

**Third version**

The layout epicted in Figure 3.14 is the final version of the array, comprising an 8*32 configuration with a total of 256 active elements. The pitch is 360μm, and each element spans a width of 260μm, leading to a central frequency of 2.13MHz for focused emission, absent any grating lobe effects. The aperture of the array measures 2.78mm by 11.42mm, while the total dimensions of the PCB board are 14mm by 17.8mm, sustaining a substantial thickness of 1.6mm. As derived from equation (2.11), the projected near-field natural focusing distance for this prototype is 9.937 mm. In the Matlab simulation, the plane wave generated by the intersection of the transducers can be observed, and it is more difficult to observe the natural focusing point. In Figure 3.15 (d), two wave peaks are observed closer to the transducer, one at 2.56 mm and one at 4.37 mm. The third wave peak is located at 6.6mm. However, it can be seen from the x-y plane simulation that the highest point of pressure at 2.56 mm is not located at the centre of the transducer, but at the sides. This serves as a preliminary simulation of the final plane wave test results. It's important to note that generating the plane wave isn't the ultimate objective; the purpose of the plane wave test is primarily to assess whether the fabricated array functions properly.
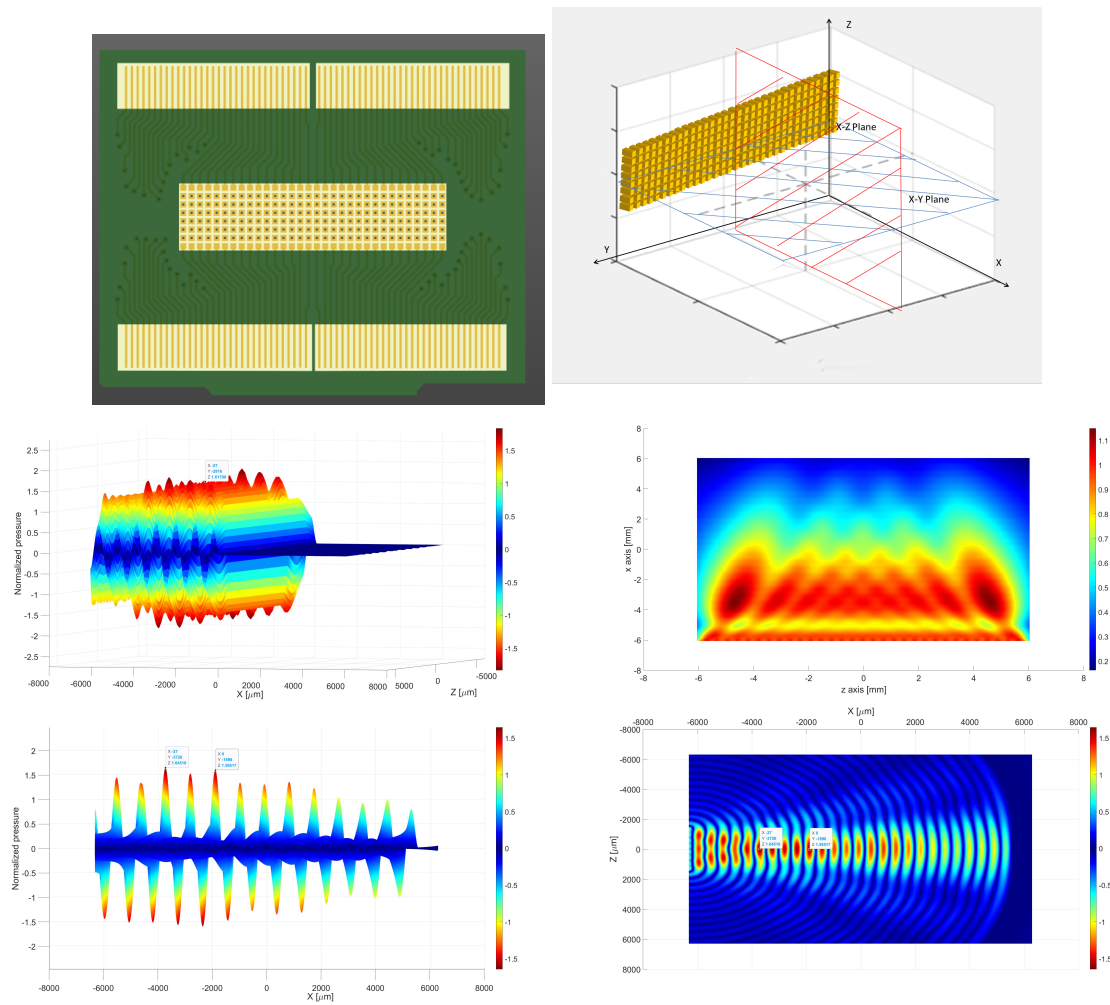
**Figure 3.14:** (a)The Third version PCB Layout (b)The Positioning of the Transducer Array Within k-wave (c) Intensity of Ultrasound Wave Propagation along the X-Y Plane (d) Beam Pattern Simulation Result on the X-Y Plane (depicted in blue)(e) Intensity of Ultrasound Wave Propagation along the X-Z Plane (f) Beam Pattern Simulation Result on the X-Z Plane (depicted in red)
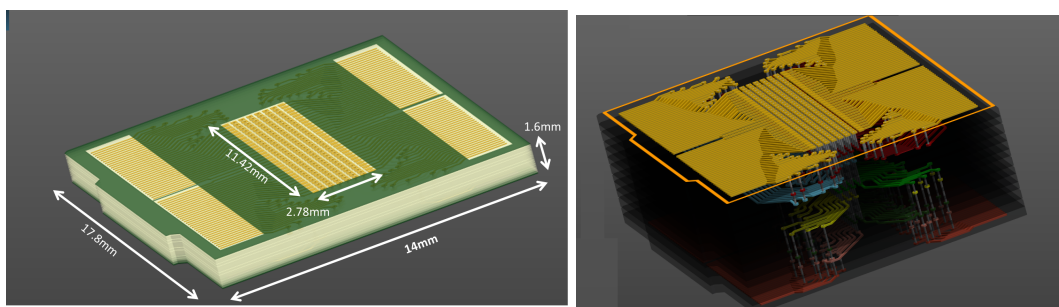


**Figure 3.15:** (a)PCB Profile (b)Illustration of Interlayer Connections

This design is primed for future phased-controlled focusing tests, utilizing the Verasonics Vantage 256 programmable platform. The chosen method maximizes the number of controllable elements, keeping in sync with the 256-port capability of the Verasonics device.

The final 3D appearance of the board is shown in Figure 3.15. The board features 256 fan-out traces, complemented by soldermask exposures located along the longer sides on both the upper and lower surfaces, as well as the front and back aspects of the board. These are specifically designed to facilitate the connection of cables to allow for the intake of external signals. The cross-sectional schematic underscores the presence of a high-density network of well-organized interconnections housed within the inner layers of the board. Each row of pads features a group of in-pad vias connected to the same inner layer.

All of the interactions between the layers enabled by the vias are shown in Figure 3.16 (g), where Figure 3.16 (g) demonstrates the color of each layer. The signal input fan-outs on the upper surface of the PCB cater to the first two and last two rows of the eight-row pad arrangement. The third to sixth rows of pads connect to the bottom surface of the PCB. This bottom surface also features a symmetrical array of trace contacts along the board edges, designed to align with the top surface for external signal reception.
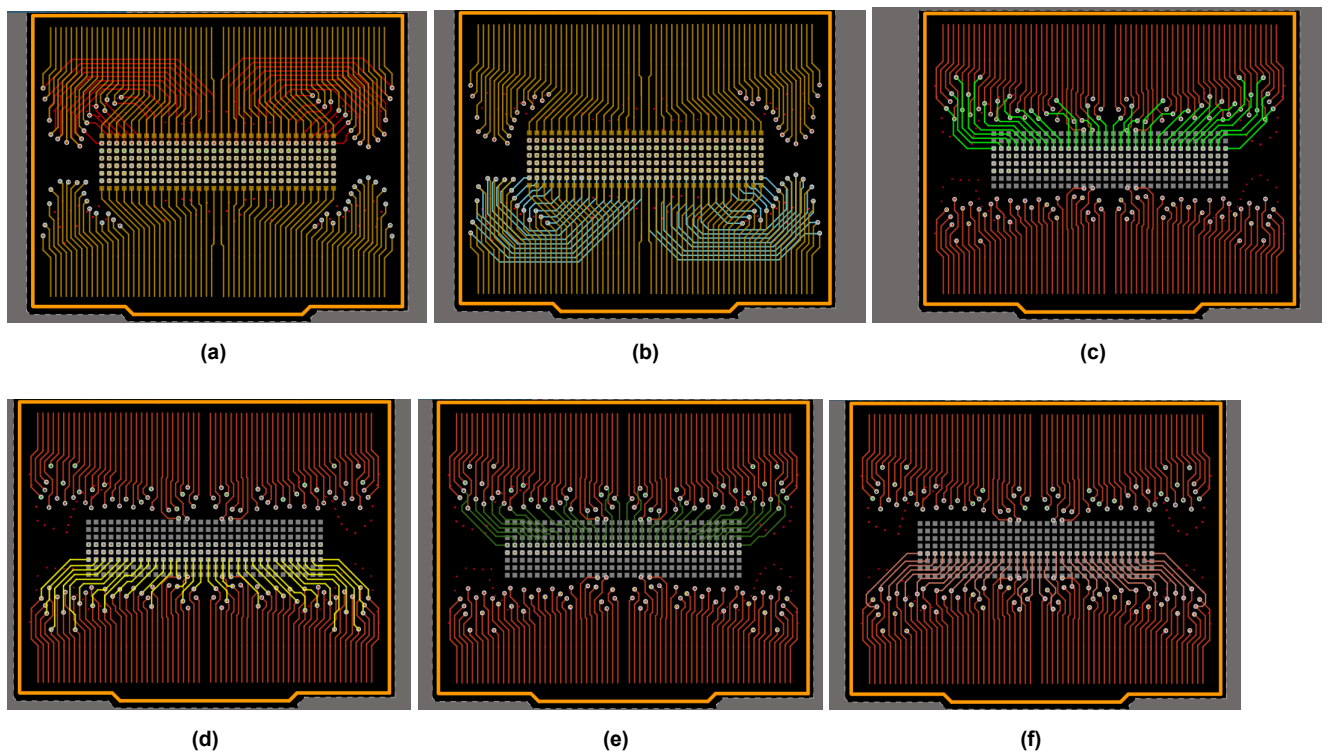


Figure 3.16: Interconnection Between Different Layers

Figure 3.16 (a) presents the first and eighth rows of components, wired directly from the top layer to the exposed trace positioned at the top and bottom edge of the PCB.
Meanwhile, the second row of elements connects to the second layer via vias (illustrated in red), routed within the second layer to locations above the left and right sides of the array. Subsequently, these are reconnected to the first layer via vias and routed outwards. The seventh row is routed within the third layer (illustrated in blue) and connected to the bottom of the PCB in the same way, as shown in Figure 3.16 (b). The contact pads of the third through sixth rows are connected from their respective pad locations to the fourth and seventh layers internally, as shown in Figure 3.16 (c)-(f). Following this, they are routed from these specific internal layers to designated locations, transitioning to the bottom layer and extending to the externally exposed trace locations.
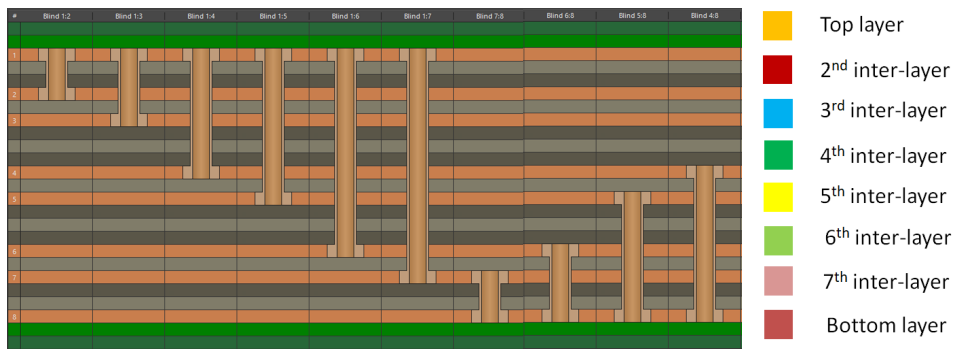
**Figure 3.17:** The Blind vias Inside PCBs

### 3.3.3. Design Progress of the Prototype 2

The second flexible manufacturer allows a minimum contact pad width of 150um and a minimum pad-to-pad distance of 25um. The maximum contact pad width is 300um, as a larger pad may lead to PCB damage on a flexible substrate. In this study, an internal array width of 150um is selected, with a pad distance of 25um, equivalent to a pitch of 195um, allowing an emission frequency of 4MHz. The external array width is 250um, with a pad distance of 100um, equal to a pitch of 350um, permitting an emission frequency of 2MHz. The first version of the flexible PCB was designed to have a length of 55mm, aimed at facilitating a patch-like fit when wrapped around the neck, as shown in Figure 3.18 (a). Taking into account both manufacturing costs and the need for miniaturization, the design was revised for the final model. The result is a 4-layer stacked flexible version with dimensions measuring 36mm along the longer side and 22mm on the shorter side, as illustrated in Figure 3.18 (b). The inner array spans a width of 1.145mm, while the outer array extends across a width of 2.7mm.
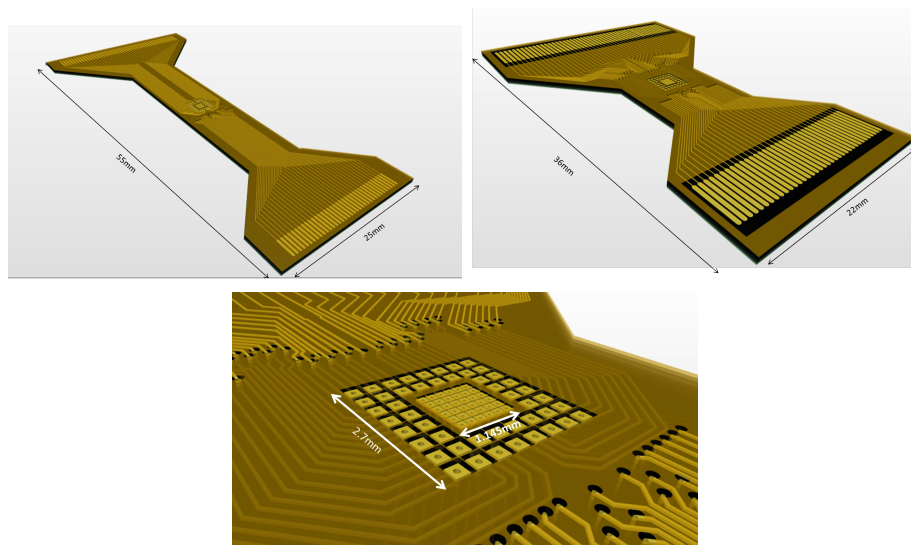


**Figure 3.18:** (a)Profile of the First version Flaxible PCB (b)Profile of the Final Flaxible PCB Layout (c) A
Close-Up View of the Contact Pad Array

The following details pertain to inter-layer connections. To prevent damage to the traces during assembly, the first layer doesn't have wires close to the contact pads; all wiring is contained within the inner layer. The outermost 48 components are connected to the second layer through vias ( shown as the blue trace) and routed to the right side in Figure 3.19 (b). The connections then pass from the second layer through vias to the first layer, eventually linking with the trace array on the far right side of the FPCB. The internal

36 components are routed on the third and bottom layers. The first two columns, as well as the fifth and sixth columns, are linked to the third layer through via connections (red trace); while the third and fourth columns are connected to the bottom layer (purple trace).
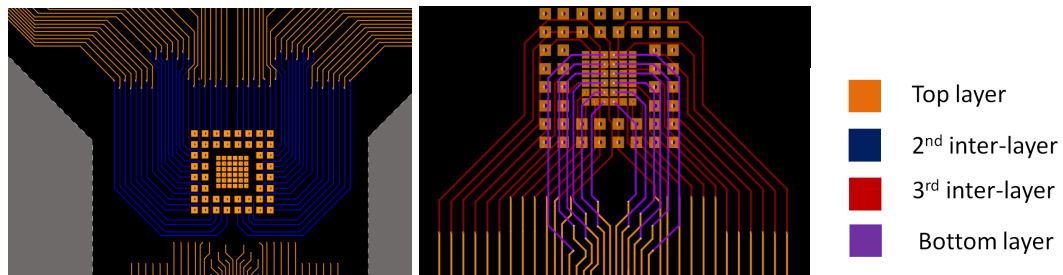


**Figure 3.19:** (a)The Flexible PCB Layout (b)Color Representation of Each Layer (c)Peripheral Arrays Interlinked with Second Layer via Vias, Subsequently Fanning Out (d)Internal Arrays Interlinked with Third and Bottom Layers via Vias, Subsequently Fanning Out

In the end, the internal array is connected to the 36 trace array on the far left side of the FPCB for receiving signals.

<div style="text-align: right;">

# 4

</div>

# Fabrication

## 4.1. Method of Fabrication and Employed Materials/Devices

The fabrication process of the prototype involves the following:
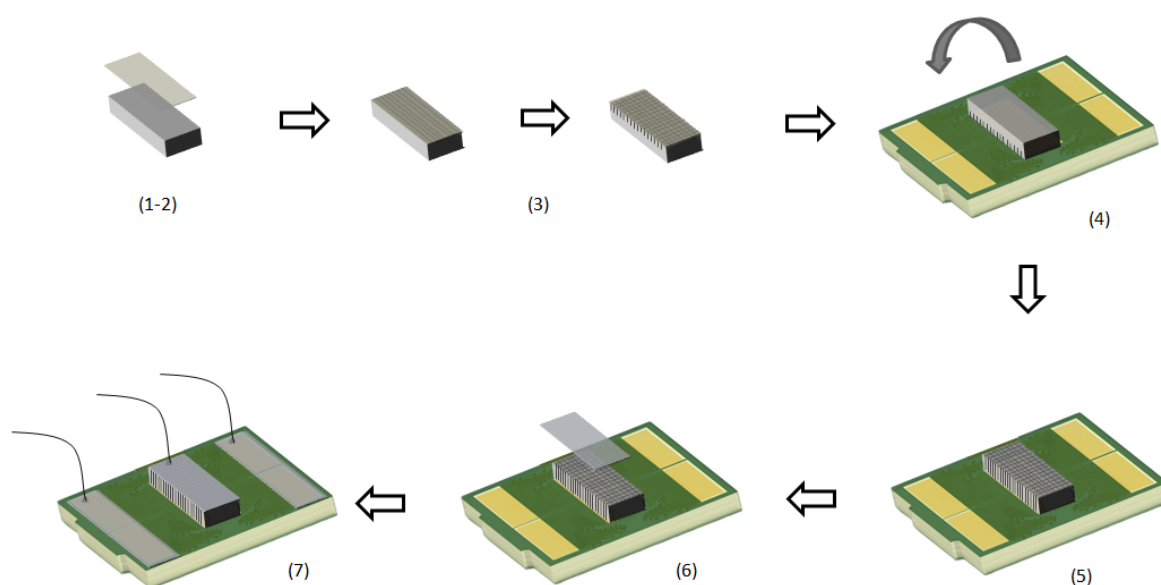


**Figure 4.1:** The Fabrication and Assembly Process of the Prototypes

1. **Dicing an aperture-sized piezoelectric block from a large sheet of piezoelectric material.** The first prototype made use of the 2MHz PZT-5A (Commercially available from PIEZO.COM) and the 2.13MHz <001>PMN-PT (Customized ordered from JFE Mineral Co.). The second prototype used a 2MHz PZT-5A and a 4MHz PZT-5A (PIEZO.COM). The piezoelectric materials arrive from the supplier pre-sputtered with a thin layer of metal electrodes along their thickness. This arrangement offers sufficient and reliable electrical connections in this work. All piezoelectric materials operate in thickness mode: the 2MHz PZT has a thickness of 1016um, the 4MHz PZT measures 495um in thickness, and the 2.13MHz PMN-PT is 890um thick. The dicing procedure is performed using DAD3240 dicing saw (Disco Corp.), by using Diamond blade (Z09-SD2000-Y1-60 51.4x0.04ASx40).

2. **Pre-bonding the ACF on the PCB-facing side (back side) of the piezo block.** Two types of ACF were applied and tested separately.
   Pressure-sensitive ACF (ARclad 9032-70, Adhesive Research, Inc.):

   - Composition: Acrylic and is filled with conductive particles.

   - Thickness: 25 µm

   - Adhesion Process: Bonding is achieved at room temperature by exerting pressure. This can be done with either a hand roller or the Flip-Chip tool (Die-bonder T3000 pro, TRESKY).

   Thermocompression Bonding ACF (TFA22023-30 HS HighTech Corp.):

   - Composition: This ACF comprises 3um gold-plated polymer beads that are dispersed in a binder.

   - Thickness: 25 µm

   - Adhesion Process: This adhesive requires a heat-based process known as thermocompression bonding Pre-bonding Conditions:

   - Temperature: 80°C

   - Pressure: 0.2-3 MPa

   - Duration: 3-5 seconds

3. **Pre-Dicing (20% - 30%) the back side following the array pattern with ACF adhered.**
   Pre-dicing is performed using a DAD3240 dicing saw. The first reason for pre-dicing is to protect the circuits underneath the piezoelectric array. If cuts were made directly from the top surface down to the bottom, precise control of the piezoelectric material to be cut entirely without damage to the neighboring circuits would be difficult, as the ACF between the two surfaces is only a few micrometers thick. The second reason is that the material thickness is 1.016mm for 2MHz PZT, and the latest loaded blade on the dicing saw has an exposure amount of 998mm. Therefore the dicing capability is not available from the hardware perspective. Lastly, in addition to the ACF, which is only connected vertically but not horizontally, this serves as an additional assurance that each component remains electrically discrete from its neighbors.

4. **Final-bonding with the backside of piezo block facing the PCB.**
   The piezoelectric material is integrated onto the PCB through either the pressure-sensitive ACF or the thermocompression bonding ACF.
   Final-bonding conditions of thermocompression bonding ACF:

   - Temperature: 180°C

   - Pressure: 50-150 MPa

   - Duration: 20 seconds

5. **Dicing out electrically isolated arrays by machine dicing.**

6. **Placing the ground plane at the top of the array.**
   The ground layer, located above the arrays, is a layer of aluminum foil with isotropic conductive silver paste (Alfa Aesar) for bonding and electrical connection. A very thin layer of conductive silver paste is brushed onto aluminum foil, and the transducer is flipped over to place the array upside down on the foil, preventing the liquid silver paste from flowing into the kerf. The silver paste can be cured on a hotplate (ThermoScientific SP88857107) at 93°C for 15 minutes.

7. **Connecting the ground plane and the signal traces to the external connectors.**
   The tungsten wire is glued to the ground plane and connected to the ground connection of the function generator using silver paste. Meanwhile, the eight outlying signal traces on the PCB edges are interconnected via silver paste, and an aluminum foil overlay is applied to enhance this electrical connection. The tungsten filaments are bonded to the aluminum foil using silver paste. The assembly was then connected to the signal input of the function generator.

8. **Encapsulating the device to ensure that no water can leak into the transducer and the array kerf is air-filled.**

The encapsulation process sealed the entire device, exposing only the wires for signal input and grounding. The encapsulation utilizes two different materials: PDMS and paraxylene.

For the PDMS encapsulation, the method involved pouring and heating. Given the device's thickness is around 2.7mm, a 3mm mold was 3D printed. The transducer was placed inside, filled with liquid PDMS, and then kept in a vacuum desiccator for an hour to remove air bubbles. It was then cured on a hotplate at 120°C for an hour to cure .

The Parylene layer was applied by chemical vapor deposition. Initially, the transducer is placed in the deposition chamber, and the Parylene C particles are introduced into an adjacent heated chamber. Both chambers were then vacuumed. In the vacuum environment, the Parylene C particles were thermally excited to 690°C to convert them to a vapor state. Following this, the vapors undergo thermal decomposition and become gaseous polymers. Then the gaseous polymer deposits as a uniform thin layer that adheres to all surfaces. Once the Parylene particles are fully vaporized, the deposition chamber begins to cool down gradually and back to atmospheric pressure so that the encapsulated transducer can be taken out. The process lasts approximately 2-3 hours.

Creating smaller arrays is fraught with difficulties due to the design's high aspect ratio, the sheer number of components, the requirement for direct PCB integration, and the encapsulation process.

- Using air-filled kerfs instead of epoxy filling causes the pillars to lose support, making them rely solely on the ACF's adhesive properties to stay upright. Nevertheless, the adhesive quality and stability of room temperature bonding ACF are notably lower than that of thermo-compression ACF. This leading to many pillars falling off or even the entire block becoming detached during dicing. Therefore, optimizing the cutting method is necessary to retain the maximum number of pillars on the PCB.

- Accurate alignment is crucial for the flip-chip bonding, to ensure that the pre-dicing kerf perfectly matches the top dicing kerf. This alignment is essential to obtain well-defined pillars. Due to the differences between the designed kerf and the actual width of the dicing saw blade, meticulous calculations are necessary to center the kerf within the pad spacing on the PCB. Concurrently, the pre-diced arrays should be secured using a die-bonder for precise positioning.

- The PMN-PT single crystal exhibits considerable fragility and temperature sensitivity, making it more susceptible to fractures compared to PZT. This inherent delicacy poses significant challenges during dicing, particularly the potential for edge damage. Additionally, the heat generated by the dicing blade during fabrication, combined with the temperature requirements of bonding ground plane and wires, can elevate the material's temperature dangerously close to its $T_{rt}$. Such exposure risks depolarization, leading to diminished piezoelectric performance.

## 4.2. Dicing Optimization

In mechanical cutting, the dicing saw is the primary tool that uses a high-speed rotating blade to cut the specified substrate. Although simple in principle, the process is critically dependent on optimizing various parameters to ensure efficiency, accuracy, and minimal substrate degradation. This study approached optimisation from two perspectives: firstly, to improve the operating parameters of the dicing machine; and secondly, to develop a strategy for the dicing methodology.

As shown in the operating diagram of the dicing saw in Figure 4.2, the parameters that can be modified include:

- Spindle speed (rpm): This parameter indicates the angular speed of the dicing blade. The higher the spindle speed, the smoother the cut. However, high speeds have thermal effects that may cause damage to the piezoelectric properties of thermally sensitive materials such as PMN-PT. The heat generated by this friction remains challenging to quantify. On the other hand, a too-low spindle speed may not provide optimum cutting efficiency and may damage the integrity of the blades.

- Feed rate (mm/s): Feed speed refers to the speed of the substrate entering the cutting blade. In the case of small array pitches, fast feed speeds may cause unstable columns to fly off, which can cause the array to shatter and lead to a low yield rate. In addition, it could also cause chipping of the

material. Conversely, slow feed rates can lengthen machining time, thereby increasing the risk of column debonding due to long-term exposure to water flow. Our goal is to strike a balance between speed and accuracy.

- Coolant flow (L/min): During the dicing process, friction between the blade and the materials generates significant heat, signaling potential substrate damage. The coolant mitigates this thermal effect and maintains the integrity of the material. The flow rate of the coolant remains adjustable. Excessive flow rates may endanger the stability of the array, causing them to become misaligned when subjected to stress or even fall off from the substrate.
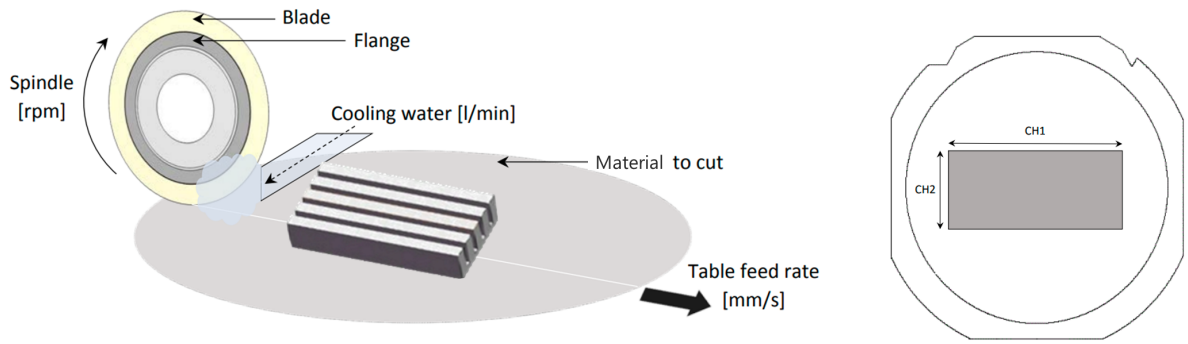


**Figure 4.2:** Conceptual Diagram of the Operation of a Dicing Saw

To fabricate the 2D array, cuts were made in both horizontal and vertical directions from right to left. The rectangular piezoelectric block was secured to the tape in the working area using a wafer mounter. As depicted in the diagram on the right in Figure 4.2, the transverse channel is denoted as CH1, while the longitudinal channel is labeled CH2. The dicing strategy is adapted to the different configurations of the two prototypes, described in the following two sections.

## 4.3. Prototype 1 Fabrication

This section provides a comprehensive approach to the fabrication process, detailing the modifications and optimization made at each stage and leading up to the final fabrication selection.

The initial prototype is a 256-element transducer array, configured as an 8x32 rectangular matrix with aperture dimensions of 2.78mm x 11.42mm. With a design pitch of 360µm, and following the half-wavelength rule, the highest achievable central frequency is 2.13MHz. The rigid PCB, used for the integration of piezoelectric material, has a contact pad width of 260µm and a pitch of 100µm. Considering the dicing saw's blade thickness is 40µm and its maximum cutting kerf is 50µm, the array was designed with a 310µm pillar width and a 50µm kerf. This doesn't perfectly align with the size of the contact pad at the base but ensures electrical separation between the components. For manufacturing the prototype transducer, two types of piezoelectric materials were used: a 2MHz PZT and an <001> oriented 2.13MHz PMN-0.3PT piezoelectric single crystal. The fabrication process is shown in Figure 4.1, and the specific optimization procedure is described below.

### 4.3.1. Gradual Steps in Process Optimization

**Step (1)-(3) ACF bonding and Pre-dicing**

Pressure-sensitive ACF was chosen as the bonding material over thermo-compression ACF for two main reasons. First, thermo-compression ACF demands a pressure range of 50-150 MPa during the final bonding stage. Considering the lower limit of this range, given a desired pressure 50MPa and an area

$A = 2.78 \times 10^{-3}\,\text{m} \times 11.42 \times 10^{-3}\,\text{m} = 31.7656 \times 10^{-6}\,\text{m}^2$, the force $F$ needed is:

$$F = P \times A \tag{4.1}$$

Given the gravitational acceleration $g \approx 9.81\,\text{m/s}^2$, the equivalent mass $m$ to exert this force is:

$$m = \frac{F}{g} \approx \frac{1588.28\,\text{N}}{9.81\,\text{m/s}^2} \approx 162.006\,\text{kg}. \tag{4.2}$$

The Die-Bounder has a maximum force output of 50kg, which experimental results have shown is inadequate for effective bonding. The second reason is that the final bonding for thermo-compression ACF necessitates a temperature of 180°C. This is significantly above the Curie temperature (Tc) of approximately 140°C for PMN-PT, resulting in a total loss of its piezoelectric properties.

The pressure-sensitive ACF demands multiple adjustments and iterations, as its application is entirely manual, as illustrated in the subsequent table detailing three different applications leading to the ultimate array cut outcomes. This ACF has dual liners, first removes the primary liner, adheres the now-exposed ACF side to the material, applies uniform force across the opposite liner surface, and subsequently discards the latter liner.
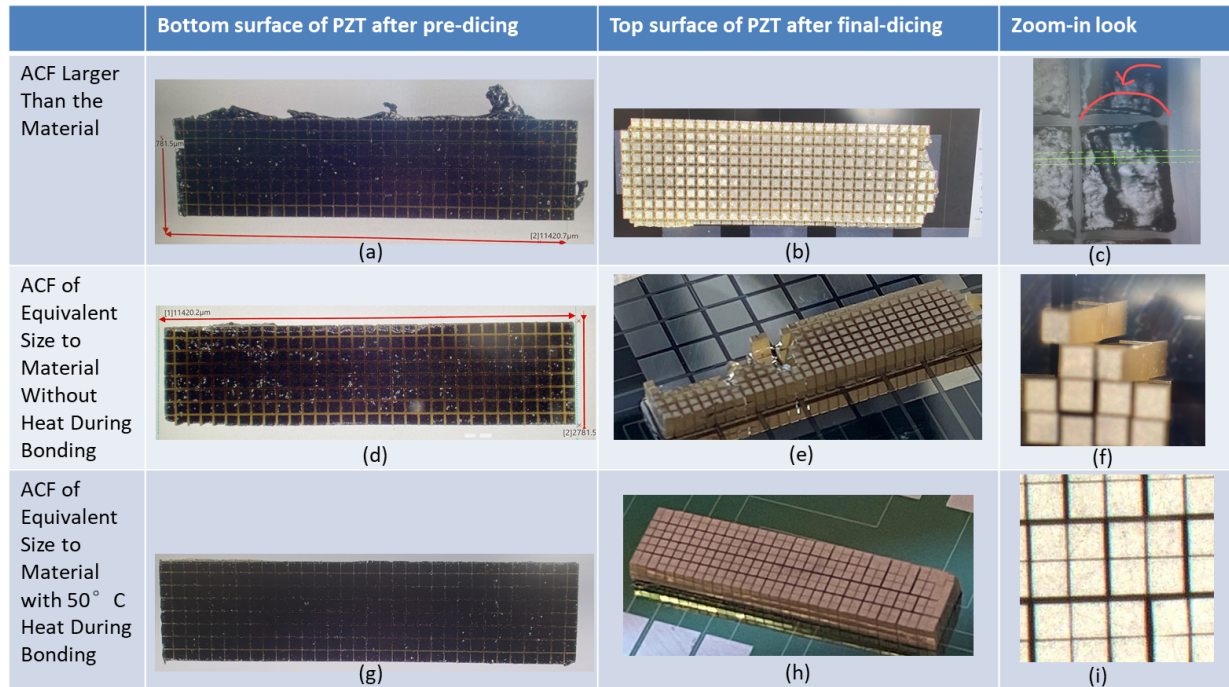
|  | Bottom surface of PZT after pre-dicing | Top surface of PZT after final-dicing | Zoom-in look |
|---|---|---|---|
| ACF Larger Than the Material | (a) | (b) | (c) |
| ACF of Equivalent Size to Material Without Heat During Bonding | (d) | (e) | (f) |
| ACF of Equivalent Size to Material with 50°C Heat During Bonding | (g) | (h) | (i) |

**Figure 4.3:** Optimization of Step(1)-(3)

The ACF must align precisely with the material surface. If the ACF is slightly larger than the material, it may warp during the pre-dicing phase, as the black film in Figure 4.3 (a) depicts. Consequently, the excess ACF may fold onto the surface of the pre-cut pillar, also illustrated in Figure 4.3 (c). This warping can lead to an incomplete ACF adherence to the surface. It may cause instability in the pillar sections covered by the ACF, resulting in pillars detaching after the final array cut. As illustrated in Figure 4.3 (b), out of 256 elements, only 222 remained intact.When the ACF is adhered to the material, removing the secondary liner from the ACF's surface can exert a peeling force, potentially dislodging the previously attached ACF from the material. As depicted in Figure 4.3 (d), the white reflection amidst the black ACF arises because the ACF at this position has been slightly stretched, potentially leading to internal water accumulation or inflation, causing it to hover over the material's surface after pre-dicing due to nonconformity. Consequently, during the final dicing, the non-adhered sections of the pillars are eroded by water. As illustrated in Figure 4.3 (e),

**Table 4.1:** Dicing Parameters for Pre-dicing

|      | Work Length | Cut Line | Work Thickness | Index    | Feed Speed | Spindle Speed |
|------|-------------|----------|----------------|----------|------------|---------------|
| CH1  | 11.42 mm    | 7        | 0.2 mm         | 0.36 mm  | 0.8 mm/s   | 20000 rpm     |
| CH2  | 2.78 mm     | 31       | 0.2 mm         | 0.36 mm  | 0.8 mm/s   | 20000 rpm     |

out of 256, only 202 elements remained intact.

Refining involves introducing specific heat during the pre-bonding force application to the ACF. In this instance, a 50°C hot plate was employed to facilitate this. While not specified in the ACF instructions, introducing heat aids in achieving more uniform and robust adhesion. The appearance of the material during pre-dicing, when bonded using this method, is presented in Figure 4.3 (g). The ACF firmly adheres to each pillar, and the array is shaped with minimized damage. The ultimate array presentation post final-dicing is depicted in Figure 4.3(h), preserving all 256 elements. Some clusters are evident between the elements, but these aspects will be refined in subsequent sections.

Pre-dicing is conducted at a rotational speed of 20,000 rpm and a feed rate of 0.8mm/s. The complete parameters are shown in Table 4.1 below. The reduced speed ensures the integrity of the ACF is maintained. The cutting depth is set at 200µm, which corresponds to 20% of the material's thickness. This percentage guarantees an adequate margin between the blade and the substrate, ensuring the blade avoids contact with the circuits during the final cut. Simultaneously, exposing twenty percent of the array ensures it remains robust enough to withstand the force applied during the final bonding without fracturing.

**Step (5) Final dicing strategy and parameter optimization**

The final cut attempt was challenging and required many iterations of optimisation and testing. Due to the limited adhesive capacity of the ACF and the high aspect ratio, pillars reaching heights of 1016µm, anchored only by 25µm of ACF, risked dislodgement, resulting in incomplete arrays. Existing SOPs dictate standard PZT cutting parameters: a spindle speed of 30,000 and a feed rate of 6 mm/s, accompanied by a coolant flow rate of 1 L/min. While these parameters facilitate efficient cutting of PZT, they do not ensure the structural integrity of air-filled kerf PZT arrays throughout the process.

There are three challenges highlighted in Figure 4.5 that require attention.

- Firstly, the limited adhesive strength of the ACF can result in significant portions of the PZT block dislodging during the cutting procedure, or certain pillars detaching in the final stages of cutting the PZT travel pillars. This detachment of PZT is primarily due to the effects of condensate washout. As illustrated in the third figure in Figure 4.5, condensate is directed across the array counter to the direction of the blade's movement, aiding in the removal of debris. Owing to the array's narrow apertures, directing condensate towards the PZT sidewall is tantamount to a continuous force being exerted on the pillars. Considering that the blades progress from right to left, the leftmost section of the array undergoes extended exposure to this flushing, making it particularly vulnerable to being dislodged. The challenge is exacerbated when cutting CH2, which consists of 32 columns of elements. This implies 31 cuts are needed, heightening the risk of the edge pillars clustering more than any other pillar section.
- The second challenge highlighted is the misalignment between pre-dicing and final-dicing. Absent a consistent alignment marker for both stages, reliance is primarily on memory and adjusting the starting position of the cuts. The width of the cutting kerf, around 55µm, contrasts with the spacing of the contact pad, which is 100µm. The final bonding phase aligns the PZT's edge with the outermost edge of its corresponding contact pad. Consequently, if the commencement positions of both cuts align with the top and bottom surfaces of the PZT, a notable misalignment between the two kerfs will ensue. As demonstrated in Fig. 4.5.4, such misalignment can result in an incomplete cut through the entire PZT block, rendering it non-functional.
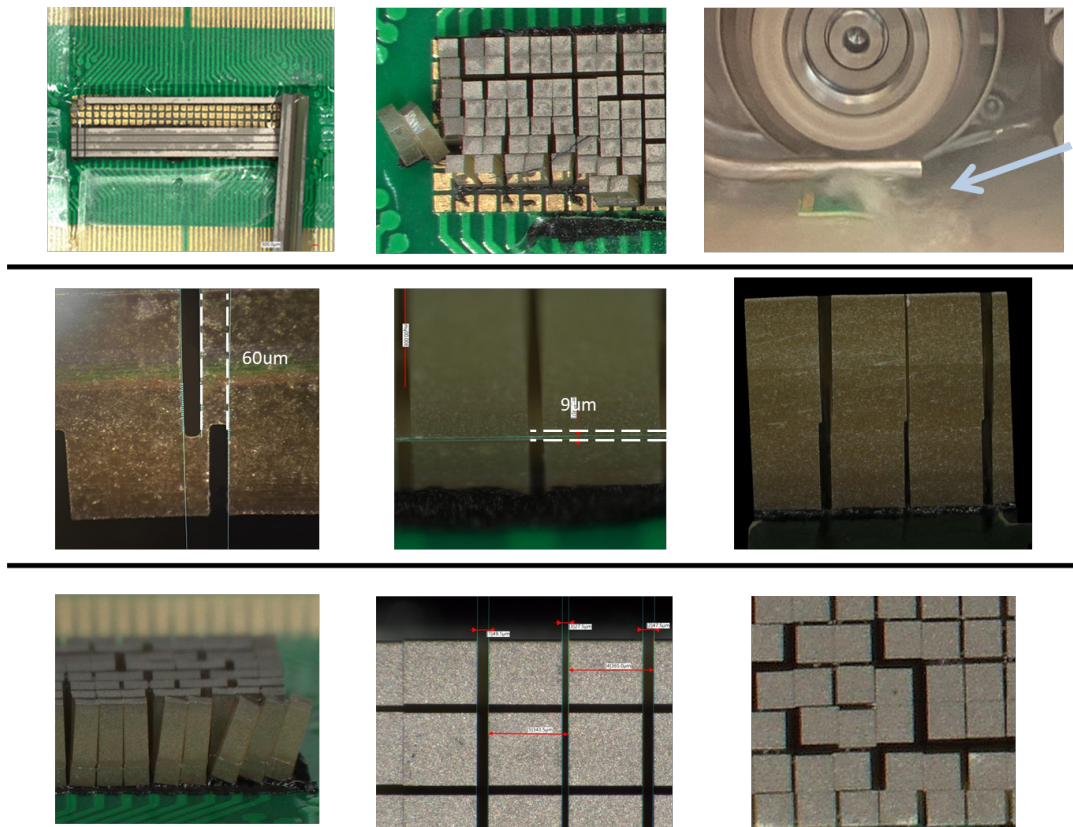
**Figure 4.4:** Challenges Encountered: Top Row - PZT Block Detachment During Cutting; Middle Row -

Misalignment Between Pre-Dicing and Final-Dicing; Bottom Row - Pillar Skew and Clustering Issues.

Ensuring complete cut-through after addressing the misalignment is the next step. As illustrated in the subsequent figure, even with perfect alignment between the upper and lower kerfs, there remains an uncut segment measuring 9µm out of 1016µm due to a computation oversight. This arises because the cutter only gauges the distance from the blade to the table surface. Hence, the cutting depth should be determined by subtracting the height of the blade above the table surface from the sample's overall height. In the case of final-dicing, the entire sample height comprises the bottom tape (70µm), PCB ( 1600µm), PZT (1016µm), and ACF ( 30µm). Given the irregularity of the PCB and the fluctuation in ACF, there's an approximate 0.5% height variance across the sample's surface. If the height measurement taken corresponds to a higher point on the sample's surface, it's plausible that the blade won't cut through at a lower point. A viable remedy is to allocate a more generous margin, ensuring that the blade penetrates deep enough to pre-dice the kerf within a depth range of 50µm to 100µm, guaranteeing a thorough cut-through, as shown in Figure 4.5, the sixth figure.

- The final concerns pertain to pillar skew and clustering, as depicted in the last three images. Such issues can manifest in compromised electrical connections and certain locations failing to satisfy the stipulation of a pitch surpassing half a wavelength. Additionally, they can compromise the overall stability of the device.

Addressing these challenges necessitates a two-pronged approach: optimizing the ACF and refining the cutting protocol.The initial approach involved placing the diced sample on a hot plate post-cutting to aid in moisture evaporation. Given that the entire workspace was damp with coolant by the end of the dicing operation, and the clustering visibly worsened due to water escaping the array gaps. The reason can be that the progression of the clusters was linked to the flow dynamics of the evaporating water. As a result, an experimental procedure was initiated to place the diced sample on a hot plate set at 50°C for two minutes to facilitate water evaporation. Nonetheless, as illustrated in the accompany-

ing figure, this process only exacerbated the clustering issue. Consequently, this method was discontinued.

The second approach involved using themo-pressed ACF, known for its superior bonding capabilities. Though the specifications for this piezoelectric block called for a pressure of 160kg to achieve the minimum ACF bonding requirements, only the die-bonder's maximum force of 50kg was utilized in practice. Another noticeable issue was the limitation of the die-bonder's tip diameter. It wasn't as wide as the sample's width, which meant that when pressure was applied, it was localized at the tip. This led to two observable cracks in the PZT block, with the left and right ends of the bar buckling upwards. Despite these setbacks, the final dicing achieved a 100% pillar retention rate. However, during the final test, no ultrasonic waves were detected, attributed to electrical connection issues caused by the uneven height. An alternative method might have been to bisect the piezoelectric material into two equal segments and bond them separately. Unfortunately, this potential solution wasn't pursued due to time constraints.
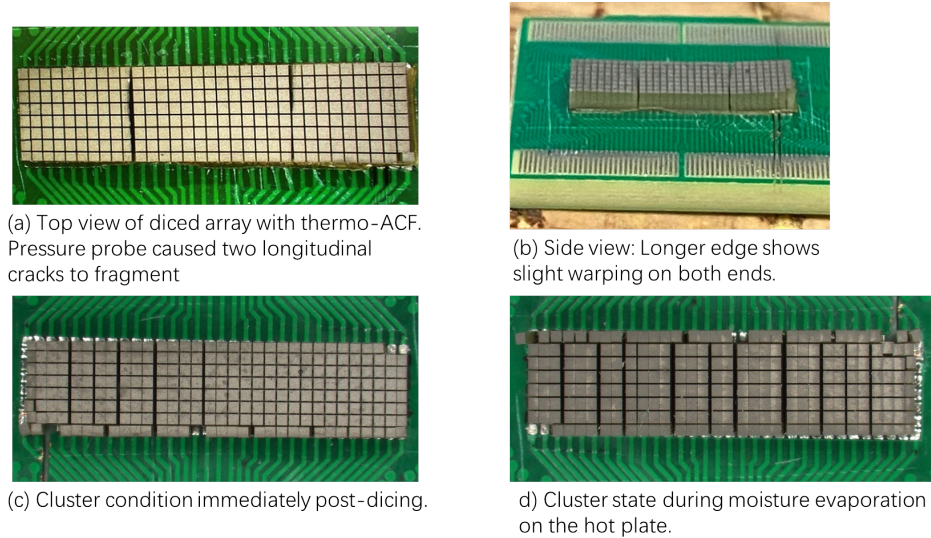
(a) Top view of diced array with thermo-ACF. Pressure probe caused two longitudinal cracks to fragment

(b) Side view: Longer edge shows slight warping on both ends.

(c) Cluster condition immediately post-dicing.

d) Cluster state during moisture evaporation on the hot plate.

**Figure 4.5:** Two Approaches to Address the Insufficient Adhesiveness of ACF.

Optimization primarily revolved around refining cutting parameters and strategy. Based on the research conducted, the production parameters detailed by T Costa et al. are an important benchmark, as listed in Table 4.2. Not only was their production methodology influential, but the dicing techniques they employed provided valuable insights. However, direct replication is not feasible given the differences between their study and this work in terms of material frequencies, ACF type differences and substrate differences. Instead, optimization is necessary to tailor these parameters to our specific requirements and environment.

**Table 4.2:** Dicing Parameters Sourced from T. Costa's SOP [47]

|  | Back side dicing | Final Dicing |
|---|---|---|
| Dicing Percentage | 20% | 80% |
| Pitch(mm) | 0.135 | 0.135 |
| Feed Rate CH1(mm/s) | 3 | 1 |
| Feed Rate CH2(mm/s) | 3 | 0.5 |
| Spindle Speed(rpm) | 14000 | 14000 |

Five distinct strategies were implemented, with their respective cutting parameters and end results show-

cased in Figure 4.7. These methods drew inspiration from hands-on laboratory experience, collaborative discussions, and existing literature. In the end, the most effective approach was identified, yielding a commendable 100 pillar retention and a cluster rate below 5%.

- The inaugural strategy involved cutting horizontally first, then vertically, as displayed in Figure 4.7, titled 'Sequential Dicing, CH2 before CH1'. This method produced 32 shorter columns before creating eight longer rows. The goal was to minimize the cluster ratio. Given that clustering predominantly occurs at sites flushed by the coolant during the CH2 cut, the thought was to cut CH2 first. This would then produce a strip eight times the length of a pillar, hypothesized to be sturdier than individual pillars. However, the results, as depicted on the right, indicated a complete dislocation of the entire array, resulting in a clustering rate of 100%.

- In the second methodology, CH1 is diced in two separate stages, followed by CH2, also diced in two separate stages. This sub-dicing approach was inspired by the work of W. Wu and colleagues [23]. When crafting a kerf 10μm wide and 1mm deep for 1-3 composite PMN-PT materials, they employed five sub-dicing passes. This strategy was to counteract blade jitter, which could lead to a kerf width greater than anticipated in relation to the blade. For the purpose of maintaining pillar stability, as illustrated in the second row of Fig. 4.7 labeled "Sequential Dicing," this work also uses two sub-dicing passes. This is employed to manage the remaining 740μm thickness after an initial 280μm pre-cut. However, an obstacle arose: following the dicing of CH1 and subsequent dicing of CH2, the entire PZT block detached.

- As outlined in Figure 4.7, the third strategy revolved around the fine-tuning of both spindle speed and feed rate. The available spectrum for spindle speed adjustments ranged from 6,000 to 60,000 rpm. Conventionally, in our laboratory settings, PZT is diced at 20,000 RPM, whereas silicon cutting is performed at a slightly higher rate of 30,000 rpm. Several external research initiatives have embraced lower spindle speeds, reporting promising results [56] [47]. Moreover, finding from studies indicates that speeds exceeding 20,000 rpm can precipitate a marked uptick in component failure rates [23] [57]. With these realizations, this attempt (shown in the third row of Fig. 4.7) began with a three sub-cutting process. In the final sub-cutting stage, a low spindle speed and feed rate was used to minimize potential damage, achieving a 100% pillar retention rate, and 20% cluster rate.

- The fourth strategy, as outlined in Figure 4.7, builds upon the foundational principles of the third approach. In the initial phase of the third sub-dicing, the blade index is set to 720um. This configuration results in a 4 by 16 array, with a width of 670um and thickness of 1016um.
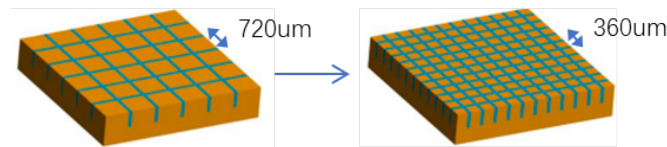


Next, each of the thicker pillars in the previously cut array is bisected, allowing us to achieve our desired pitch of 360um. This double-pitch methodology, which was inspired by relevant literature, is recognized for its efficacy in bolstering the structural integrity of the array[58] [59] [60].

- The ultimate approach to dicing, as depicted in the last line of Figure 4.7, is a refined version of the fourth strategy. By further decreasing the spindle speed, significant improvements were observed in the clustering rate. As a result, a fully air-filled piezoelectric array was achieved with a completion rate of 100%. The only minor clustering was observed in the upper right corner, showcasing the efficacy of this optimized method.

## Sequential Dicing: CH2 Before CH1 - Utilizing Dual Sub-Dicing

| | Pre-dice CH1/CH2 | Sub-dice 1 CH2/CH1 | Sub-dice2 CH2/CH1 |
|---|---|---|---|
| Cutting depth | 280um(730um left) | 400um(330um left) | 780um(-50um) |
| Blade speed (mm/s) | 3/3 | 2/1.5 | 0.3/0.15 |
| Spindle speed (rpm) | 20000 | 20000 | 20000 |
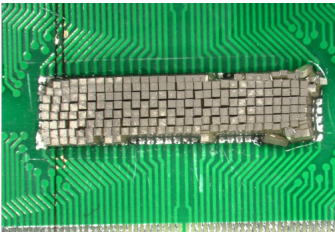
**Retention Rate:** 237/256
**Cluster rate：** 100%

## Sequential Dicing: Dice through CH1, then CH2, Each in Two Sub-Dicing Steps.

| | Pre-dice CH1/CH2 | Sub-dice 1 CH1 | Sub-dice 2 CH1 | Sub-dice 3 CH2 | Sub-dice 2 CH2 |
|---|---|---|---|---|---|
| Cutting depth | 280um(730um left) | 400um(330um left) | 380um(-50um left) | 400um(330um left) | 380um(-50um left) |
| Blade speed(mm/s) | 3/3 | 2 | 1.5 | 2 | 1.5 |
| Spindle speed (rpm) | 20000 | 20000 | 20000 | 20000 | 20000 |
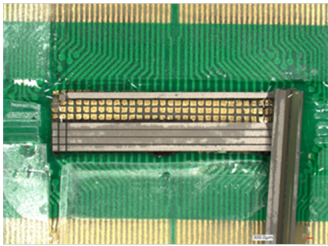
**Retention Rate:** - - -
**Cluster rate：** - - -

## Triple Sub-Dicing

| | Pre-dice CH1/CH2 | Sub-dice 1 CH1/CH2 | Sub-dice 2 CH1/CH2 | Sub-dice3 CH1/CH2 |
|---|---|---|---|---|
| Cutting depth | 280um(730um left) | 300um(430um left) | 580um(150um left) | 780um(-50um) |
| Blade speed (mm/s) | 3/3 | 2/1.5 | 2/1.5 | 0.3/0.15 |
| Spindle speed (rpm) | 20000 | 15000 | 15000 | 12000 |
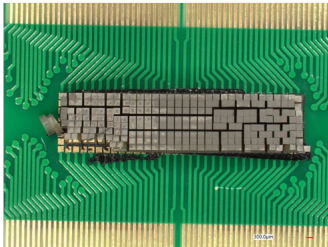
**Retention Rate:** 245/256
**Cluster rate：** 80%

## Triple Sub-Dicing with Double-Pitch : In the 3rd sub-dicing, Cut at Double the Target Pitch, Then Halve to Desired Pitch.

| | Pre-dice CH1/CH2 | Sub-dice 1 CH1/CH2 | Sub-dice 2 CH1/CH2 | Sub-dice3 Double pitch 720um | Sub-dice3 Double pitch 720um |
|---|---|---|---|---|---|
| Cutting depth | 300um(720um left) | 300um(520um left) | 300um(120um left) | 150um (-30um) | 150um (-30um) |
| Blade speed (mm/s) | 4/4 | 2/2 | 2/2 | 0.25/0.25 | 0.25/0.15 |
| Spindle speed(rpm) | 20000 | 15000 | 15000 | 12000 | 12000 |

**Retention Rate:** 256/256
**Cluster rate：** 17.2%

## Triple Sub-Dicing with Double-Pitch with Decreased spindle speed

| | Pre-dice CH1/CH2 | Sub-dice 1 CH1/CH2 | Sub-dice 2 CH1/CH2 | Sub-dice3 Double pitch 720um | Sub-dice3 Double pitch 720um |
|---|---|---|---|---|---|
| Cutting depth | 300um(720um left) | 300um(520um left) | 300um(120um left) | 150um (-30um) | 150um (-30um) |
| Blade speed (mm/s) | 4/4 | 2/2 | 2/2 | 0.25/0.25 | 0.25/0.15 |
| Spindle speed(rpm) | 20000 | 12000 | 10000 | 8000 | 8000 |
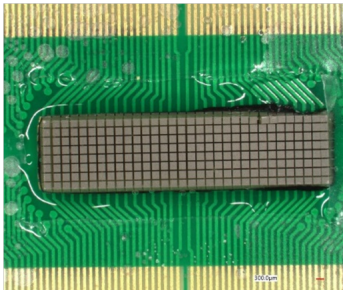
**Retention Rate:** 256/256
**Cluster rate：** 4.6%

**Figure 4.6:** Refining Dicing Strategies and Parameters for Enhanced Precision
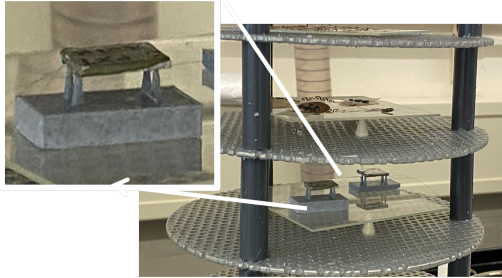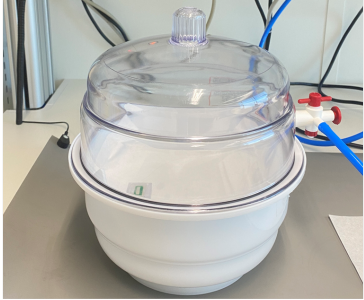
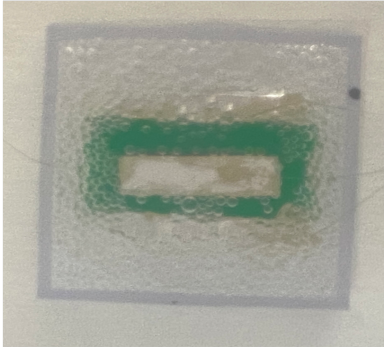**Step (5) Encapsulation Method Selection**
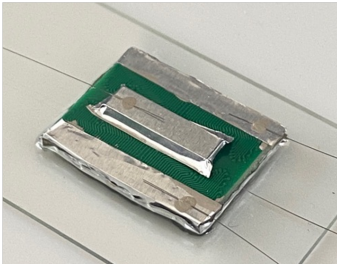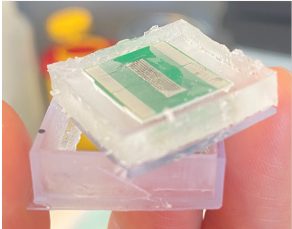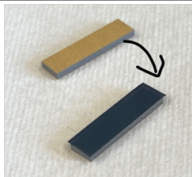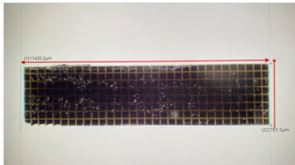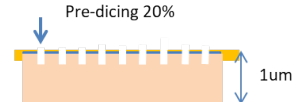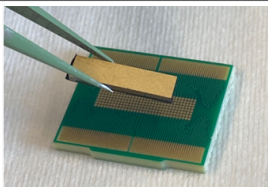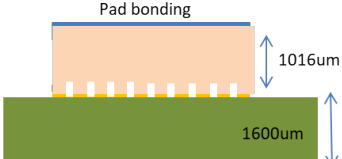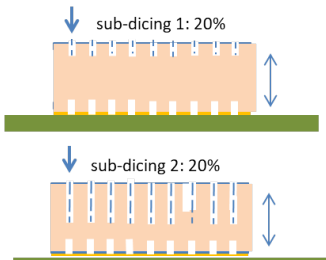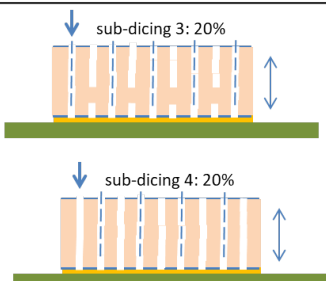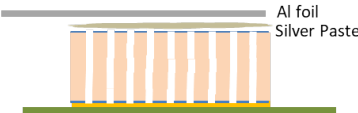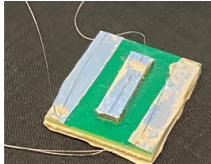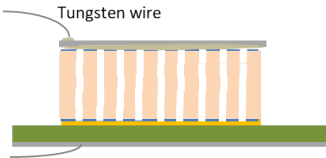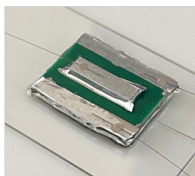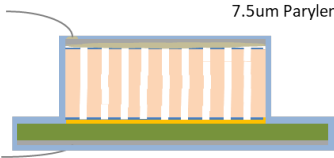
| Encapsulation using Parylene | Encapsulation using PDMS |
|---|---|
| A 3D-printed fixture with four protrusions ensures that the device is adequately suspended within the CVD chamber, allowing for comprehensive encapsulation by the parylene environment. | Pour the prepared liquid PDMS into a 3D printed mold along with the device and put it inside the vacuum desiccator for one hour to remove the air bubbles inside the PDMS. |
| The samples were placed in the parylene coater containing 15 grams of parylene particles, corresponding to 7.5 um of attachment. | From a top perspective, the appearance of the sample after five minutes within the desiccator reveals significant bubble formation. |
| The final product has 7.5um of transparent parylene attached to it, which appears invisible in comparison to the 2.7mm thick sample. | The mold was heated on a hot plate at 120° C for 1 hour. Afterward, the device was removed from the mold. With a total thickness of 3mm, the PDMS layer measures between 200μm and 300μm. |

**Figure 4.7:** Methodology and Outcomes for Both Encapsulation Techniques

Both Parylene and PDMS encapsulation methods were evaluated independently, with the procedure and resulting products illustrated in Figure 4.8. The CVD-coated parylene demonstrated uniform and high-quality films. In contrast, when curing PDMS to form a film, it's challenging to regulate the encapsulation thickness. Furthermore, during testing in an aqueous environment, a significant number of bubbles emerged on the transducer's surface over time. It's postulated that the piezoelectric material experienced a fracture at a certain point due to oscillations, rendering it unsuitable for further use. Consequently, the Parylene coating was selected as the preferred encapsulation method.

## 4.3.2 The Optimized Fabrication Flow

| Explanation of the steps | | Side View Schematic |
|---|---|---|
| • Cut strips of 2.78mm x 11.42mm from the large PZT block.<br>• Remove one liner from the ACF and place it on the side of the PZT that will face the PCB.<br>• Press firmly on the hot plate at 50°C for 5 seconds. |  | <br>25um<br>1016um<br>ACF tacking |

| Pre-dicing | CH1 | CH2 |
|---|---|---|
| Cutting depth | 300um | 300um |
| Blade speed (mm/s) | 4 | 4 |
| Spindle speed (rpm) | 20000 | 20000 |




Pre-dicing 20%
1um

| | Side View |
|---|---|
| • Bake the PCB at 120°C for 3 hours to eliminate moisture.<br>• Apply even pressure on the hot plate at 50°C for 5 seconds. |  |

Pad bonding
1016um
1600um


| | Sub-dicing 1 | | Sub-dicing 2 | |
|---|---|---|---|---|
| Index: 360um | CH1 | CH2 | CH1 | CH2 |
| Cutting depth | 300um | 300um | 300um | 300um |
| Blade speed (mm/s) | 2 | 2 | 2 | 2 |
| Spindle speed (rpm) | 12000 | 12000 | 10000 | 10000 |

sub-dicing 1: 20%
sub-dicing 2: 20%


| | Sub-dicing 3 | | Sub-dicing 4 | |
|---|---|---|---|---|
| Index: 720um | CH1 | CH2 | CH1 | CH2 |
| Cutting depth | 150um | 150um | 150um | 150um |
| Blade speed (mm/s) | 0.25 | 0.25 | 0.25 | 0.15 |
| Spindle speed (rpm) | 8000 | 8000 | 8000 | 8000 |

sub-dicing 3: 20%
sub-dicing 4: 20%


| Explanation | | Schematic |
|---|---|---|
| • Place aluminum foil as a ground layer and connect with silver epoxy.<br>• Heat on a hot plate at 93°C for 15 minutes to cure the epoxy.<br>• Use the same method to short-circuit the traces on the PCB. |  | <br>Al foil<br>Silver Paste |
| • Attach tungsten wires to the Al foil using a minimal amount of silver epoxy.<br>• Place the ground wire on one side of the PCB tray and the three signal wires on the opposite side to avoid future short-circuits. |  | Tungsten wire<br> |
| • Coat the sample with 7.5 um of parylene.<br>• Scraped off the parylene layer at tip of the tungsten wire using a blade to facilitate upcoming electrical tests. |  | 7.5um Parylene<br> |

### 4.3.3 PMN-PT dicing attempt

This study presents a comprehensive literature review on the micro-scale machining of PMN-PT. Various publications propose distinct optimal parameters, contingent upon the specific equipment employed in their research. For instance, Michau et al. identified a cutting speed of 0.6 mm/s as optimal, noting the absence of chipping [48]. Conversely, M. Rachael et al., while working with PIN-PMN-PT of 0.5mm pitch and 0.25mm thickness, discerned optimal conditions to be 0.12 mm/s at 12000 rpm, maintaining a water flow rate of 0.6 L/min [57]. Additionally, W. Wu et al., processing PMN-PT with a thickness of 1mm, opted for a speed of 0.4 mm/s and 20000 rpm, executing the operation in five stages [23].

| Spindle speed | Feed rate | num. of cracks | Average depth of cracks |
|---|---|---|---|
| 8000rpm | 0.1mm/s | 8 | 5.28um |
|  | 0.25mm/s | 12 | 5.76um |
|  | 0.5mm/s | 10 | 5.69um |
|  | 0.8mm/s | 17 | 6.91um |
|  | 1.0mm/s | 17 | 7.81um |
| 6000rpm | 0.1mm/s | 7 | 4.29um |
| 8000rpm |  | 8 | 5.28um |
| 10000rpm |  | 9 | 4.96um |
| 15000rpm |  | 6 | 3.83um |
| 20000rpm |  | 8 | 4.22um |

- Reference image on quantifying the degree of crack
- Shape of the crack on the sidewall
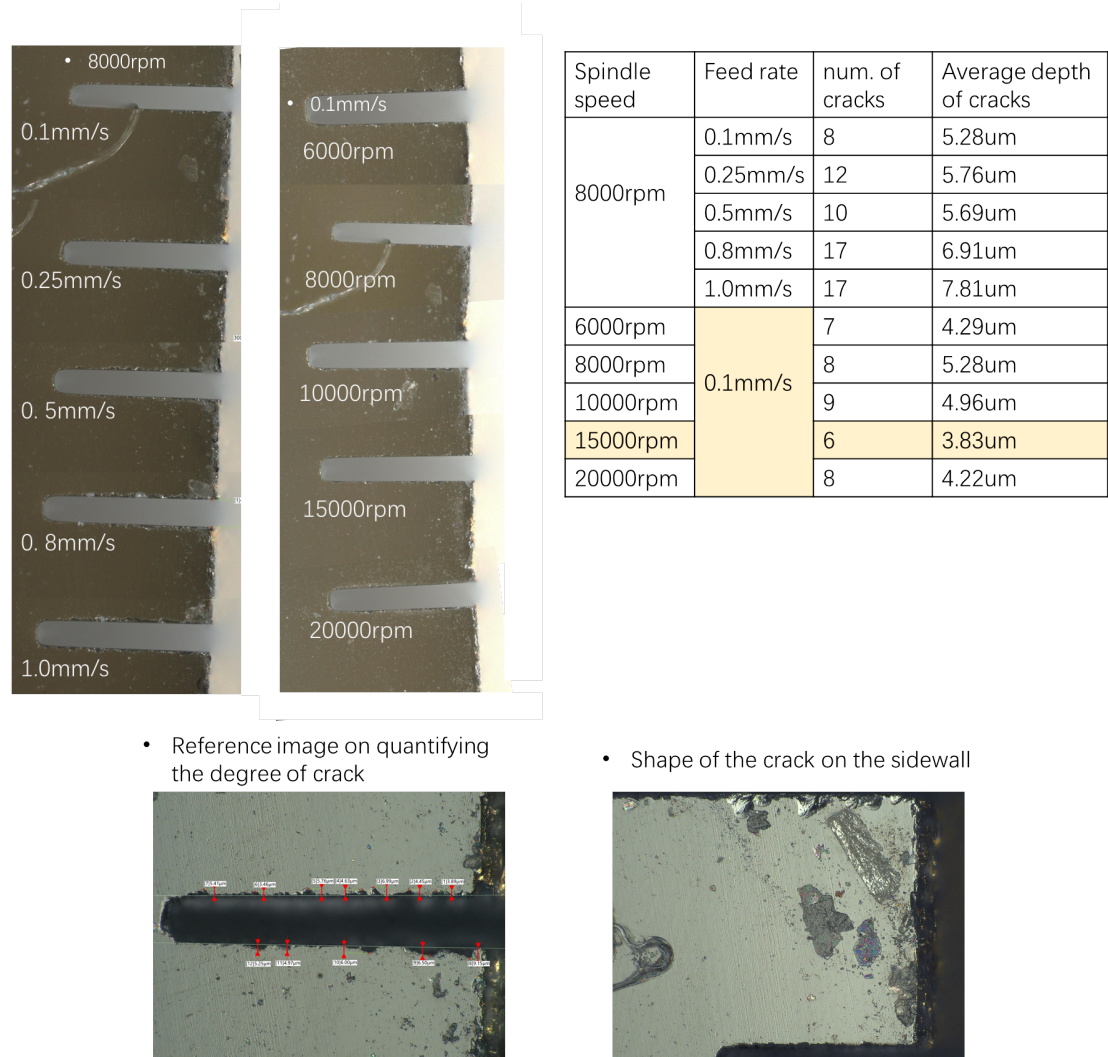
**Figure 4.8:** Determination of the Optimal Parameter for Minimal Cutting Damage

Building upon substantial expertise in PZT machining, this study posits that reduced feed and spindle speeds contribute more effectively to preserving array integrity. Consequently, cuts of 200µm depth were executed employing a notably low feed speed bracket (0.1mm/s to 1mm/s) and a spindle speed range of 8000rpm to 20000rpm. A comparative analysis of kerf-induced fractures is illustrated in Figure 4.9. This research introduces a criterion for assessing the magnitude of cut loss, determining the optimal parameter for minimal cutting damage. The evaluation involves counting incisions on the sidewall exceeding 3µm in depth and ascertaining their mean depth. The cutting parameters that result in the fewest of these defects and the most modest average depth are regarded as optimal. This criterion is not ideal, as evident from the bottom right figure. The morphology of cracks on the sidewall indicates that the damage isn't confined to the periphery. Instead, the crystals delaminate in layers along the inner wall. Yet, the inner kerf wall's

profile remains unexamined in existing literature. In any case, this measurement is still informative. From the tabulated data, the optimal parameters derived are: a spindle speed of 15,000rpm, a feed rate of 0.1mm/s, and a coolant water flow rate of 0.5L/min.

The PMN-PT manufacturer was consulted for their endorsed protocols, especially since they've introduced a novel spindle tailored for PMN-PT. Other academic and research institutions have also been sourced for single crystals, some of which have seen successful fabrication and consequent publication. The manufacturer advised a spindle speed of 30,000 rpm, a feed rate of 0.7 mm/s, and a coolant water flow rate of 1 L/min. This study incorporated these parameters in a cutting test. For a holistic understanding, suboptimal cuts were also analyzed, as delineated in Fig. 4.10. Evidently, the parameter optimization undertaken in this research considerably enhanced the uniformity of PMN-PT cuts.



The optimized parameter founded :
- 15000rpm, 0.1mm/s, 0.5L/min
- 3 sub -dice

Manufacturer suggestions:
- 30000rpm, 0.7mm/s, 1L/min
- 3 sub-dice

Worst case
- 8000rpm, 0.8mm/s, 0.5L/min
- no sub-dice
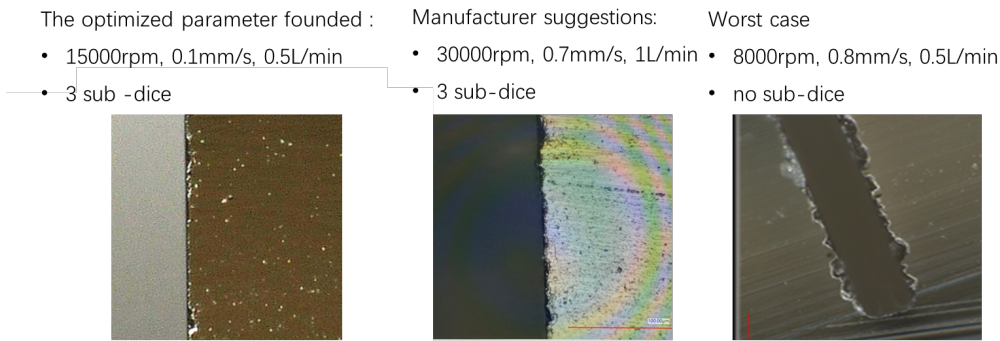
**Figure 4.9:** Comparison of cuts Using Optimal Parameters from this Study, Supplier Recommendations, and Worst-case Parameters

The endeavor to fabricate the PMN-PT transducer array was not realized due to the crystal's inherent brittleness.



(a)

(b)

(c)

(d)
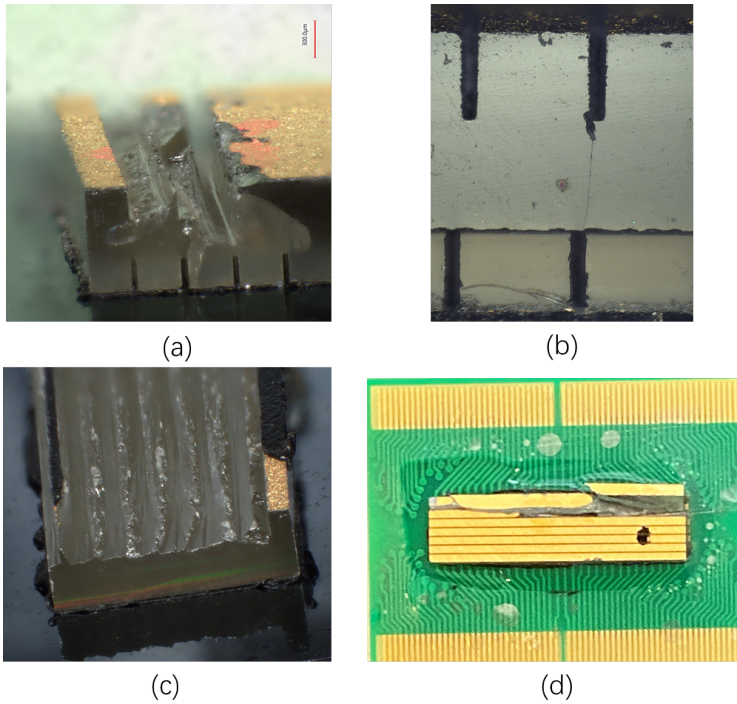
**Figure 4.10:** PMN-PT Dicing Failures

As observed in Figure 4.11 (a), post the completion of the 200um pre-dicing of the 890um PMN-PT and bonding, the dicing started from left to right. However, by the second and third rows, an entire strip of crystals detached, halting the operation, possibly due to latent internal cracks. Figure 4.11 (b) presents another attempt: even though the initial 200um sub-dicing remained intact, a discernible crack formed between the sub-dicing and pre-dicing kerfs, foretelling the subsequent collapse of the piezoelectric block during any future sub-dicing. Given these outcomes, pre-dicing was eschewed to circumvent potential micro-cracks. In Figure 4.11 (c), the entire top layer, inclusive of the gold electrodes, disintegrated. Meanwhile, Figure 4.11 (d) showcases an abrupt fissure in the last two rows of cut CH2, inflicting blade damage and causing extensive areas of the array to dislodge during the cut. Such recurrent array damage culminated in repeated destruction of the cutting saw blade. Fiscal considerations and the associated challenges deterred further attempts. Consequently, only entire PMN-PTs were employed for assembly and evaluation.

## 4.4. Prototype 2 Fabrication

The flexible PCB's design is depicted in Figure 4.12. It has a length of 36 mm and a width of 22 mm on its shorter side, featuring a bend tailored to fit the neck's shape. The inner array has a width of 1.145 mm, a trace width of 150um, a pad spacing of 25um, and a pitch of 195um, supporting a transmit frequency of 4MHz. In contrast, the outer array spans a width of 2.7 mm with a pitch of 350um, and it is configured to transmit at a frequency of 2MHz.
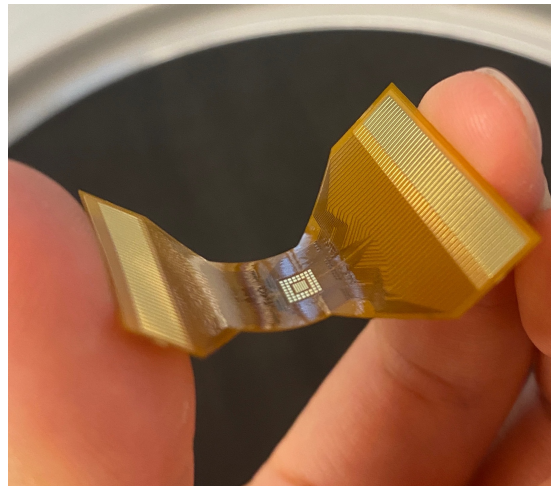


**Figure 4.11:** The Appearance of the Flexible PCB

The design of the flexible PCB is illustrated in Figure 4.12. Measuring 36 mm in length and 22 mm in width on its shorter side, the PCB is inherently flexible, enabling it to have a bend specifically designed to match the neck's contour. The inner array of the PCB features a width of 1.145 mm, a trace width of 150μm, a pad spacing of 25μm, and a pitch of 195μm. This setup supports a transmission frequency of 4MHz. On the other hand, the outer array extends across a width of 2.7 mm with a pitch of 350μm, and is designed to transmit at a frequency of 2MHz. The assembly sequence follows the one shown in Figure 4.1 In the fabrication process, two primary challenges were encountered. The first challenge was the minute size of the components. The second was the varying thicknesss of the inner and outer arrays: the 4MHz inner array's piezoelectric material has a thickness of 490μm, whereas the outer array's thickness measures 1016μm. The dicing saws used for mechanical dicing can only make a single pass from the far left to the far right of the material, prohibiting mid-material cuts. After extensive consideration, a sequence of material bonds and cuts was established to successfully fabricate the arrays.

### 4.4.1. Material Bonds and Dices Flow Chart

The material contact pad is illustrated in grey, while the PZT material is depicted in purple. The fabrication process starts with bonding the 4MHz PZT, which has been pre-diced at its bottom by 20%, to the internal array. Following this, it's segmented into 6x6 arrays, each having an element width of 1145μm. A kerf of 50μm is employed, corresponding to the width of the cutting blade. For the peripheral array's PZT placement, the 2MHz PZTs are initially sectioned into four compact blocks, each measuring 2.050mm by 650μm and having a material thickness of 1016μm. The reverse side of these blocks undergoes predicing to form a 2x6 block pattern, with a predicing depth either equating to 50% of the material or 20% of the established standard. These blocks are then meticulously bonded to the contact pad in sequence, adhering to the layout depicted in figure 4.13. The completed assembly can be viewed in figure 4.13 (7).



1. Contact pads on FPC

2. Mount the pre-diced 4MHz PZT on (490um)

3. Dice

4. Mount a quarter of 2MHz PZT (1016um)

5. Mount the 2nd quarter

6. Mount the 3rd quarter

7. Mount the 4th quarter

8. Dice the peripheral element to strips

9. Dice out the peripheral array

Finished array
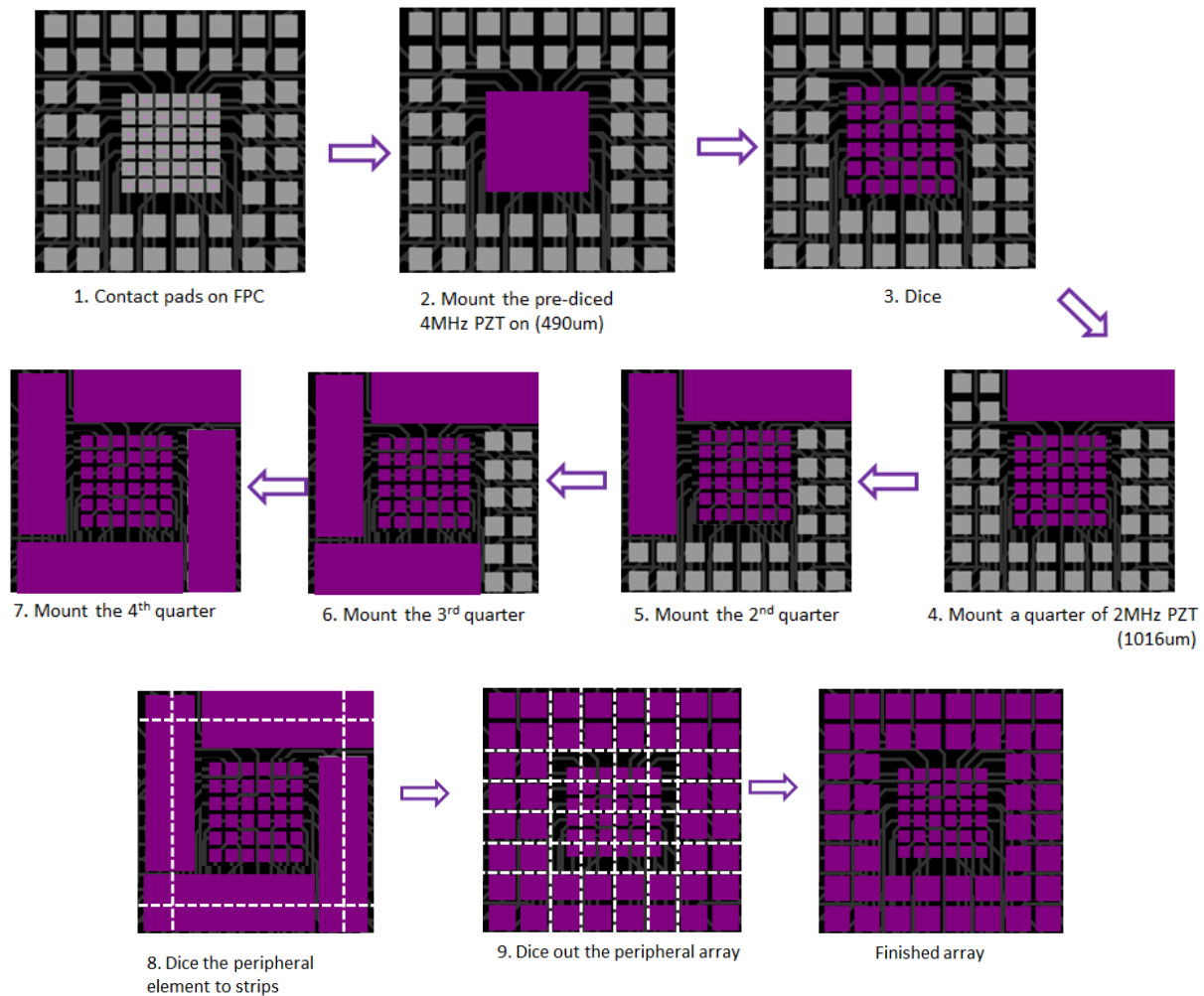
**Figure 4.12:** Material Bonds and Dices Flow Chart

Subsequently, two dicing actions were performed at both CH1 and CH2 along the white dashed lines, splitting the four rectangular blocks longitudinally down their longer sides. Following this, five additional dicing actions were carried out along the white dashed lines at each of CH1 and CH2. This alignment was strategically determined during the FPCB pad layout phase to ensure that the kerfs of the peripheral arrays align seamlessly with the internal arrays.

If the 2MHz PZT has been pre-diced by 50% prior to the commencement of the fourth step, meaning the reverse side of the 508μm has already been sliced, then considerations arise. Given that the thickness of the internal array is 490μm, only dicing the upper half ensures the ten dicing actions won't interfere with the

internal pads. Even in a scenario where only 20% of the 2MHz PZT is pre-diced, the blades during the ten dicing actions will glide smoothly through the pre-existing kerf of the internal array, hypothetically causing no damage. Through these meticulous procedures, a dual-band array can be successfully constructed.

### 4.4.2. Process Flow

Firstly, the ACF was pre-bonded to the piezoelectric block using a pick-and-place tool. This pre-bonding process utilized parameters of $T = 80°C$ and a pressing force of $3MPa$. First is the internal array bonding, with an area of :

$$A = 1.142 \times 10^{-3}\,\text{m} \times 1.142 \times 10^{-3}\,\text{m} = 1.305664 \times 10^{-6}\,\text{m}^2$$

Given the gravitational acceleration $g \approx 9.81\,\text{m/s}^2$, the equivalent mass $m$ to exert this force is:

$$m = \frac{F}{g} = \frac{P \times A}{g} =\approx \frac{3.916992\,\text{N}}{9.81\,\text{m/s}^2} \approx 0.399\,\text{kg}. \tag{4.3}$$

Bonding was performed using a 1mm diameter tip, as shown in Figure 4.14. The back side is subsequently pre-dice to a depth of 100um out of the 490um. The final bonding process is executed using the pick and place tool, at a temperature of 180°C and pressure of 50MPa. This equates to a weight applied to the sample of

$$m = \frac{F}{g} = \frac{P \times A}{g} =\approx \frac{65.2832\,\text{N}}{9.81\,\text{m/s}^2} \approx 6.659\,\text{kg}. \tag{4.4}$$



(a) Pre-bond ACF on the back side of PZT

(b) Pre-dice 20% PZT from back side

(c) Final-bond the diced side onto FPCB

(d) Top view after final-bonding

(e) Top view after final-dicing

(f) FPCB with Internal Array Assembled

(g) FPCB with both Array Assembled

(h) Side view showing thickness difference between the two arrays

(i) Silver paste for both grounding plane and connecting wires
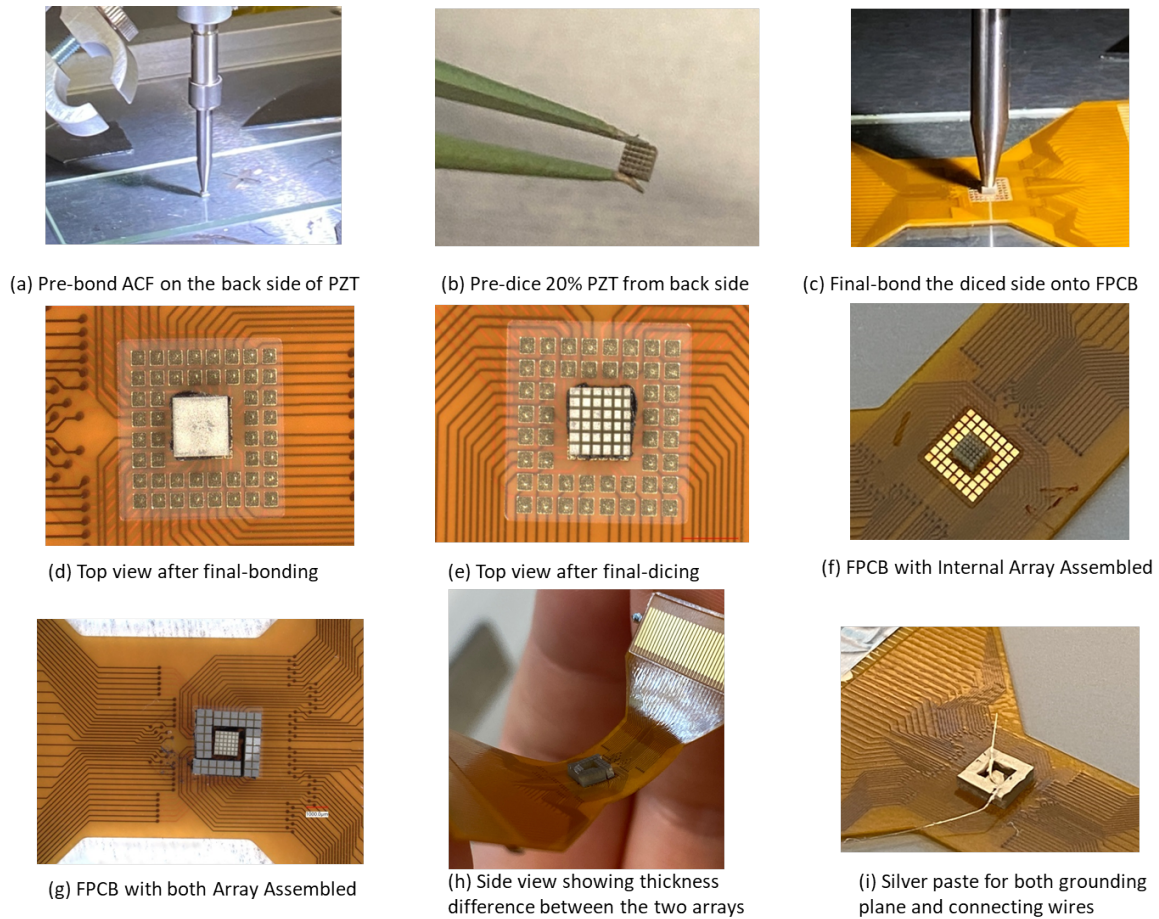
**Figure 4.13:** FPCB Fabrication and Assembly Process Flow

Given the final-bonding pressure guidelines of 50MPa-150MPa provided by the ACF supplier, larger weights of 8kg, 10kg, and 15kg were tested to determine if higher pressure would yield a stronger bond.

However, testing revealed that 15kg crushed the PZT entirely, puncturing the FPCB substrate, while 8kg caused cracks in the center of PZT. Consequently, the minimum recommended pressure was adopted. Still, a slight bulge was observed on the board's backside from the compression. The impact of this on electrical connections will be assessed in future tests. The results and procedure of the final bonding can be seen in Figure 4.14, panels (c) and (d). Figure 4.14 (e) depict the appearance after final dicing. It is noticeable that the pillar width on the left is slightly larger, a misalignment resulting from the difference between the 50μm blade width and the 25μm pad space of the substrate. The dicing parameters are shown in Table 4.3.

**Table 4.3:** Dicing Parameters for Internal Array

| | Back side dicing | Final Dicing | |
|---|---|---|---|
| | | sub-dicing 1 | sub-dicing 2 |
| Dicing Percentage | 100um (20%) | 200um (40%) | 200um (40%) |
| Pitch(mm) | 0.195 | 0.195 | 0.195 |
| Feed Rate CH1(mm/s) | 4 | 2 | 0.8 |
| Feed Rate CH2(mm/s) | 4 | 2 | 0.8 |
| Spindle Speed(rpm) | 20000 | 20000 | 15000 |

Fabricating of the peripheral array was not continued due to time constraints and equipment limitations. Firstly, since the die-bonder's tip picks up samples through vacuum suction, the smallest tip diameter is 1mm. However, the short side length of this sample is 0.73mm, which cannot cover the vacuum pad of the tip and thus cannot be picked up. As a result, bonding of the peripheral array can only be done manually using ambient temperature ACF for alignment and bonding. Secondly, the dicer malfunctioned, preventing further final-dicing.

Nevertheless, to showcase the entire fabrication process, the peripheral array was manually mounted using room temperature ACF. The final result can be seen in Fig. 4.14(e) F. It's important to note that the peripheral array wasn't fully cut; the predicing side is merely facing upwards to display the intended final shape of the peripheral array. The side view highlights the thickness difference between the 1mm thick peripheral array and the 490um thick inner array.

The unique shape of the external array and its thickness difference from the internal array present significant challenges for the common ground bonding wire process. Given its small dimensions, aluminium foil isn't a suitable ground plane. Instead, we used a thin layer of silver paste for the ground plane. During the curing process, the device was inverted to prevent the silver paste from flowing downward and causing a short circuit. Subsequently, bendable tungsten wire was bent at a specific angle to simultaneously touch the ground planes of both the inner and outer arrays.

Finally, the entire device is encapsulated in 5um parylene.

# Results

## 5.1. Measurement Setup

The following schematic illustrates the acoustic pressure measurement setup. A function generator (RIGOL DG4202) serves as the acoustic source, and the device's specific signal and ground wires connect to receive signals. Ultrasonic evaluations are conducted within a water-filled chamber, capitalizing on water's acoustic properties that mirror those of soft tissue. The device is positioned on the tank's far left, and a 10um Fibre-optic hydrophone (Precision Acoustics) is employed for ultrasound reception. Above the tank, a three-axis positioning mechanism facilitates controlled movements of the hydrophone, enabling spatial ultrasound scanning. The hydrophone's amplified output interfaces with an oscilloscope (InfiniiVision DSO-X 3032A) aligned with the output from the function generator. These components are orchestrated through MATLAB software developed by our research group.



(a)

(b)
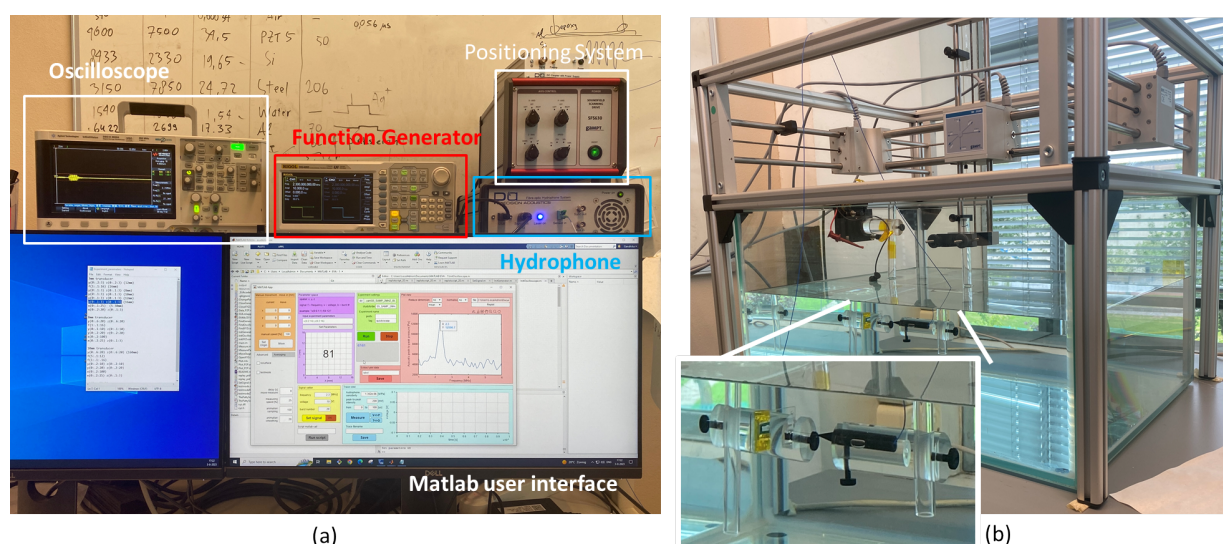
**Figure 5.1:** Measurement Setup

Figure 5.1(b) depicts the sample within the testing environment. Both the sample and the hydrophone are secured by acrylic holders and fully submerged in DI water. The hydrophone can measure distances as close as 2μm from the sample. The device is attached to a glass substrate using an epoxy (EPOTEK

301-2f, two-part epoxy). The acoustic signal consists of a 20-times oscillation of a 20V sine pulse. The hydrophone captures this signal, converting it into voltage values at a specified location, which could range from a single point to an entire spatial plane. These voltage readings are then directly translated to pressure measurements based on the hydrophone's frequency sensitivity. Therefore, a calibration is essential at the start of each test session, especially given that transducers exhibit varying sensitivities across different frequencies.

## 5.2. Measurement Result

For Prototype 1, two sets of measurements are conducted: one for the 2MHz bulk PMN-PT and the 2MHz PZT. Another set is for a fully fabricated 2MHz PZT array. Only plane wave tests are performed, as focused beam tests are restricted due to laboratory limitations.

### 5.2.1. 2MHz Bulk PMN-PT and PZT Transducer Performance Results

**Impedance Measurement**

At the physical level, the resonant frequency is calculated using equation (2.5). Accordingly, the resonant frequency of the 1016um thick PZT with a propagation speed of 4350m/s is calculated to be 2MHz. Meanwhile, the resonant frequency of the 890um thick PMN-PT with a propagation speed of 4601m/s is calculated to be 2.13MHz. The precise resonant frequency is identified by the phase peak in the electrical impedance curve. Tests are conducted using the impedance analyzer (E4990A, KEYSIGHT).



2.14MHz PMN-PT Strip      2.13MHz PMN-PT on PCB

2MHz PZT Strip      2MHz PZT on PCB
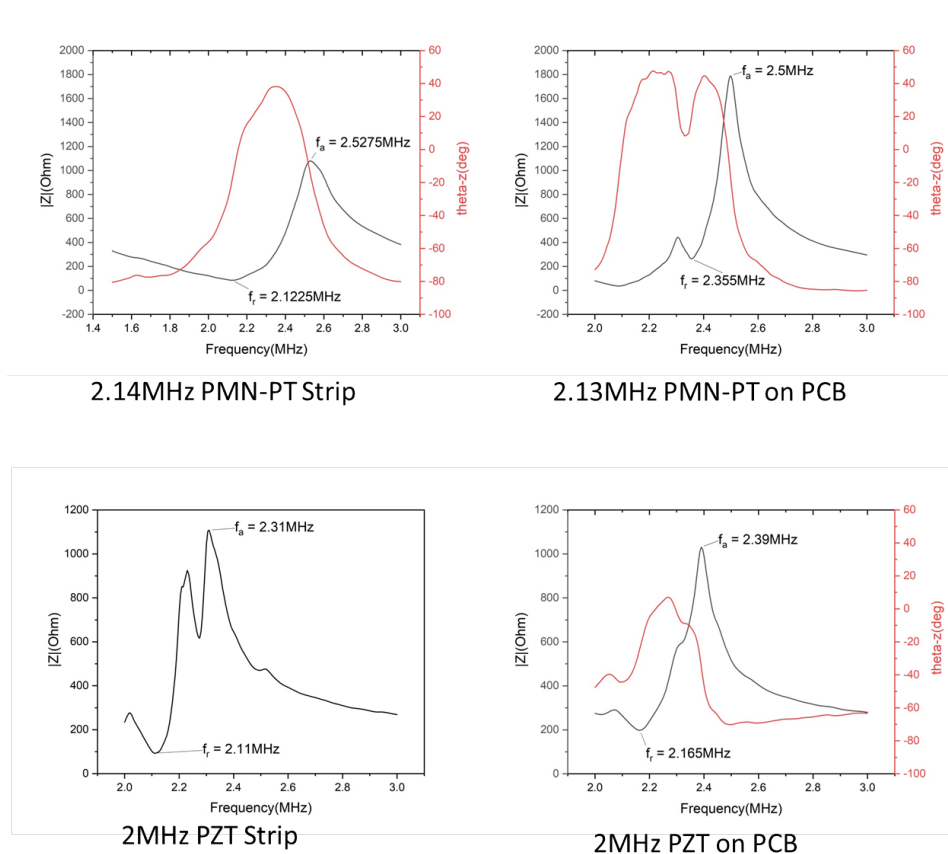
**Figure 5.2:** Impedance measurements on piezoelectric materials in air and on the fully functional devices

Impedance analysis was conducted on the bulk form piezoelectric transducer of prototype 1. Additionally, tests were performed on metal electrodes separately attached to the ends of piezoelectric samples with

the same dimensions to observe any changes in their characteristics post-assembly. Impedance testing on individual pillars of the array was not feasible due to the extremely small surface area of the material's top and bottom surfaces, which made wire bonding challenging. The results are shown in Figure 5.2.

There are numerous factors that can influence the discrepancy between the calculated resonance frequency and the fr measured with the impedance analyzer. For instance, real vibration modes might deviate from the theoretical model due to the sample's non-standard shape. Inconsistencies in the material and imperfections from the manufacturing process can further influence the results. Moreover, the effects of the electrodes and wiring cannot be disregarded. Metal electrodes on the piezoelectric material's upper and lower surfaces, along with the attached wires, can introduce additional impedance, capacitance, and other factors.

The difference in resonance frequency between measurements taken from the piezoelectric element alone and the entire device can be attributed to the following factors:
Mounting stresses and thermal effects during the assembly of the device, mechanical coupling between the PCB and the piezoelectric element, parasitic capacitance and parasitic inductance of the conductors, contact impedance between the conductors and the material electrodes, and the addition of silver epoxy to the top of the piezoelectric material, which increases mass and thereby affects the vibration characteristics. Maximum power transfer is achieved when the transducer load and the power drive source are matched. Impedance matching is not covered in this work.

### 2MHz Bulk PZT Transducer

Acoustic pressure tests can be executed using multiple methodologies, encompassing frequency sweeps to identify the resonant frequency, pinpoint measurements to ascertain distance from the transducer, and spatial plane scans to observe the trajectory of the ultrasonic beam. In light of the Matlab simulation outcomes presented in the PCB design section, it becomes evident that the acoustic wave propagation patterns of a rectangular piezoelectric block differ between the planes perpendicular to its longitudinal and lateral edges. Hence, both planes are empirically characterized in the subsequent measurements.

The empirical assessment commenced with the scanning of the plane orthogonal to the lateral edge, denoted as the X-Z plane, depicted in Figure 5.2 (b). Spatial points are rendered in varying shades, with the yellow region demarcating the zones of peak ultrasonic acoustic pressure. The peak acoustic pressure reached approximately 263 kPa. It is crucial to highlight that the origin (point 0) on the X-axis does not represent an immediate proximity to the transducer but is offset by several millimeters. This precaution ensures the hydrophone does not inadvertently contact the instrument's surface, potentially causing damage.

Subsequently, the hydrophone was repositioned to the region exhibiting the most robust acoustic pressure, inherently signifying the focal point, and a frequency sweep was conducted. The findings are illustrated in Figure 5.2 (c). Amongst the evaluated frequencies, 2.3MHz manifested the most potent acoustic pressure, designating it as the resonant frequency of the transducer. Concurrently, a range determination was undertaken at this focal juncture, as depicted in Figure 5.2 (d), revealing a focal separation of 8.7um from the transducer.

Upon establishing this distance, a spatial scan, conducted parallelly to the transducer's surface at this ascertained distance, is delineated in Figure 5.2 (f). The piezoelectric block, extending a length of 11.42mm, exhibits a central focal point, flanked by additional focal points situated 2mm to its left and right. This triad of natural focal spots appears slightly misaligned, as a result of the sensors not being perfectly parallel to the horizontal datum when fixed to the mount.
Figure (e) shows a scan of the X-Y plane, which is in the middle plane of the short side of the transducer. No wave peak is observed at 8.7um. This may be due to the tilt of the transducer placement.

### 2.13MHz Bulk PMN-PT Transducer

A piezoelectric transducer of 2.13 MHz, fabricated from PMN-PT, was constructed following an identical assembly protocol. Given that PMN-PT boasts thrice the d33 and one and a half times the k33 of PZT, it is anticipated to exhibit superior energy conversion efficiency, translating to a more pronounced piezoelectric intensity.

(a)



(b)



(c)



(d)



(e)



(f)
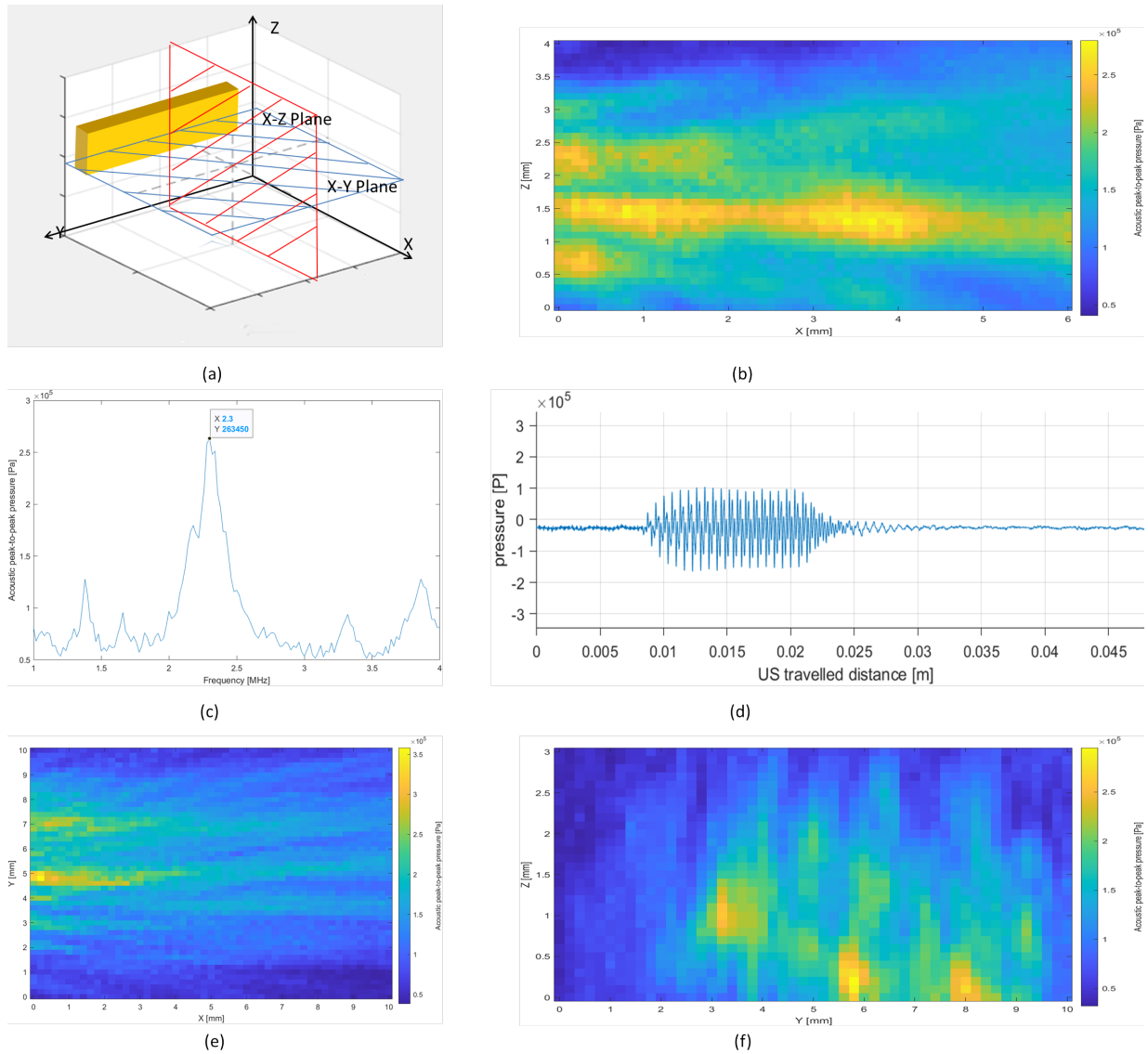
**Figure 5.3:** The 2 MHz Bulk PZT Transducer Performance Results: (a) Relative Positioning of the Transducer and the Scanning Plane for Reference (b) Scan Results in the X-Z Plane (c) Frequency Sweep at the Focal Point, Highlighting the 2.3MHz Resonance Frequency (d) Distance from the Transducer to the Focal Point Measured at 8.7µm (e) Scan Results in the X-Y Plane (f) Scanning of Y-Z Plane, Positioned 8.7µm Away.

Upon subjecting the PMN-PT transducer to analogous tests, the empirical findings were somewhat underwhelming. As depicted in Figure 5.3 (c), the PMN-PT registered a resonant frequency of 2.56 MHz, yet peaked at a mere pressure of 54.7 kPa. The focal distance was established at 5.23mm. Subsequent to this, a scan along the YZ plane, situated 5.23mm from the transducer, was executed, with results presented in Figure 5.3 (f). Drawing parallels with the PZT transducer, three natural focal points emerged. Intriguingly, the zenith of pressure wasn't centered on the transducer. Instead, it was discerned at the flanking focal points, peaking at approximately 90 kPa— a mere third of the pressure exhibited by the PZT transducer.
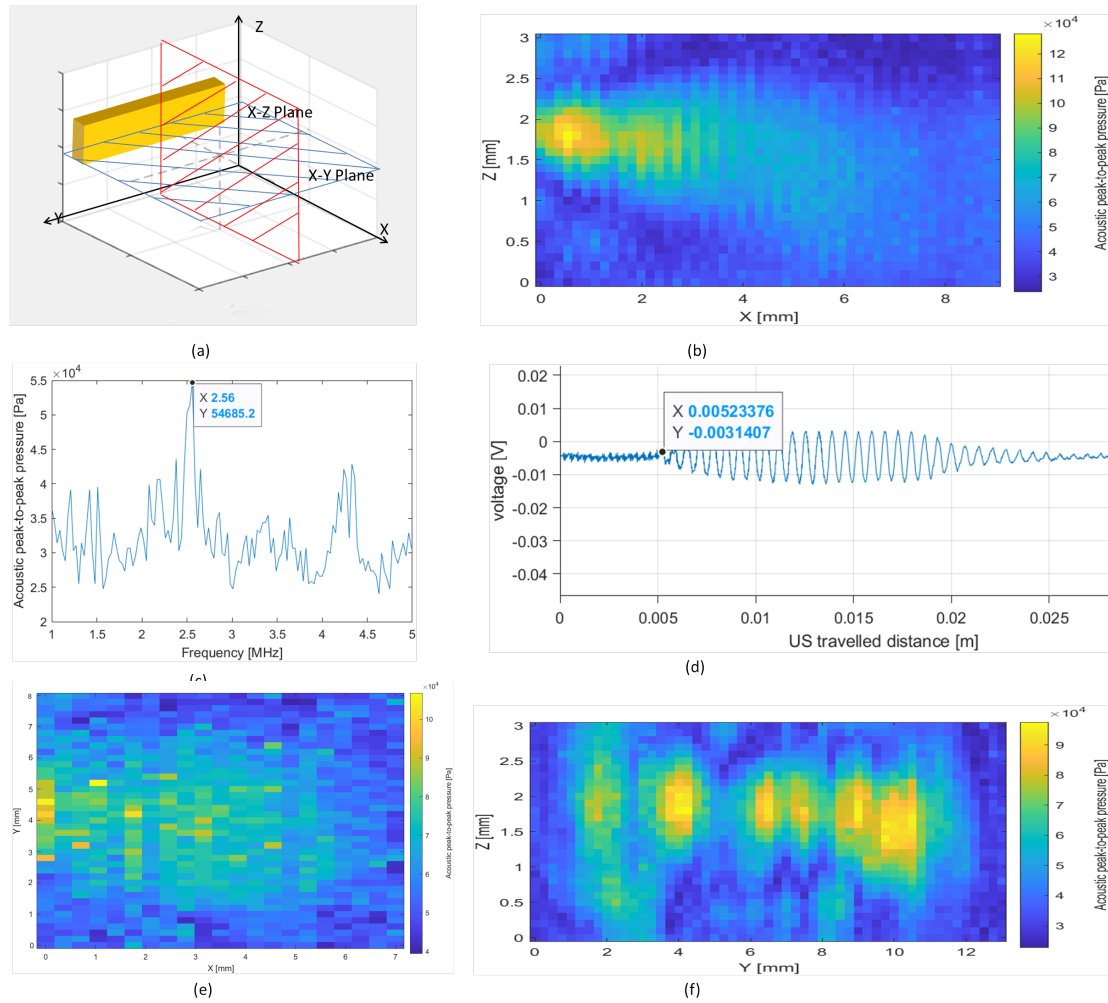
**Figure 5.4:** The 2.13 MHz Bulk PMN-PT Transducer Performance Results: (a) Position Reference (b) Scan Results in the X-Z Plane (c) Frequency Sweep at the Focal Point, Highlighting the 2.56MHz Resonance Frequency (d) Distance from the Transducer to the Focal Point Measured at 5.23µm (e) Scan Results in the X-Y Plane (f) Scanning of Y-Z Plane, Positioned 5.23µm Away from the Transducer.

A primary contributor to the PMN-PT suboptimal performance is believed to be depolarization induced by elevated temperatures. Silver epoxy, utilized in the assembly, necessitated five curing sessions at 93°C, each lasting 15 minutes. For testing purposes, the entire specimen was adhered to a glass substrate using an epoxy that mandated curing at 80°C. This culminated in the PMN-PT being subjected to temperatures hovering around 90°C for over an hour and a half. Notably, the PMN-PT also endured an excess of one hour at comparable high temperatures. Given that the PMN-PT's Trt is 80°C, its $k_{33}$ experiences a significant reduction beyond this threshold, a phenomenon depicted in Figure 2.5 [61]. This observation aligns with the findings from the current research. From Fig. 5.3 (c), the acoustic intensity response at several frequencies is notably higher, suggesting a certain degree of disruption in its internal dipole arrangement. While edge deterioration from cutting is another potential factor, considering only four edges exhibited damage in this specimen, it's deduced that this isn't a predominant factor in the observed performance decline.

Based on this extrapolation, we conducted a full room temperature assembly. Instead of curing the silver paste at the bond ground layer and tungsten wire at 93°C for 15 minutes, we allowed it to cure at room temperature for 24-48 hours. The subsequent results are as follows:

### 5.2.2. 2MHz PZT Phased Array Transducer Performance Results
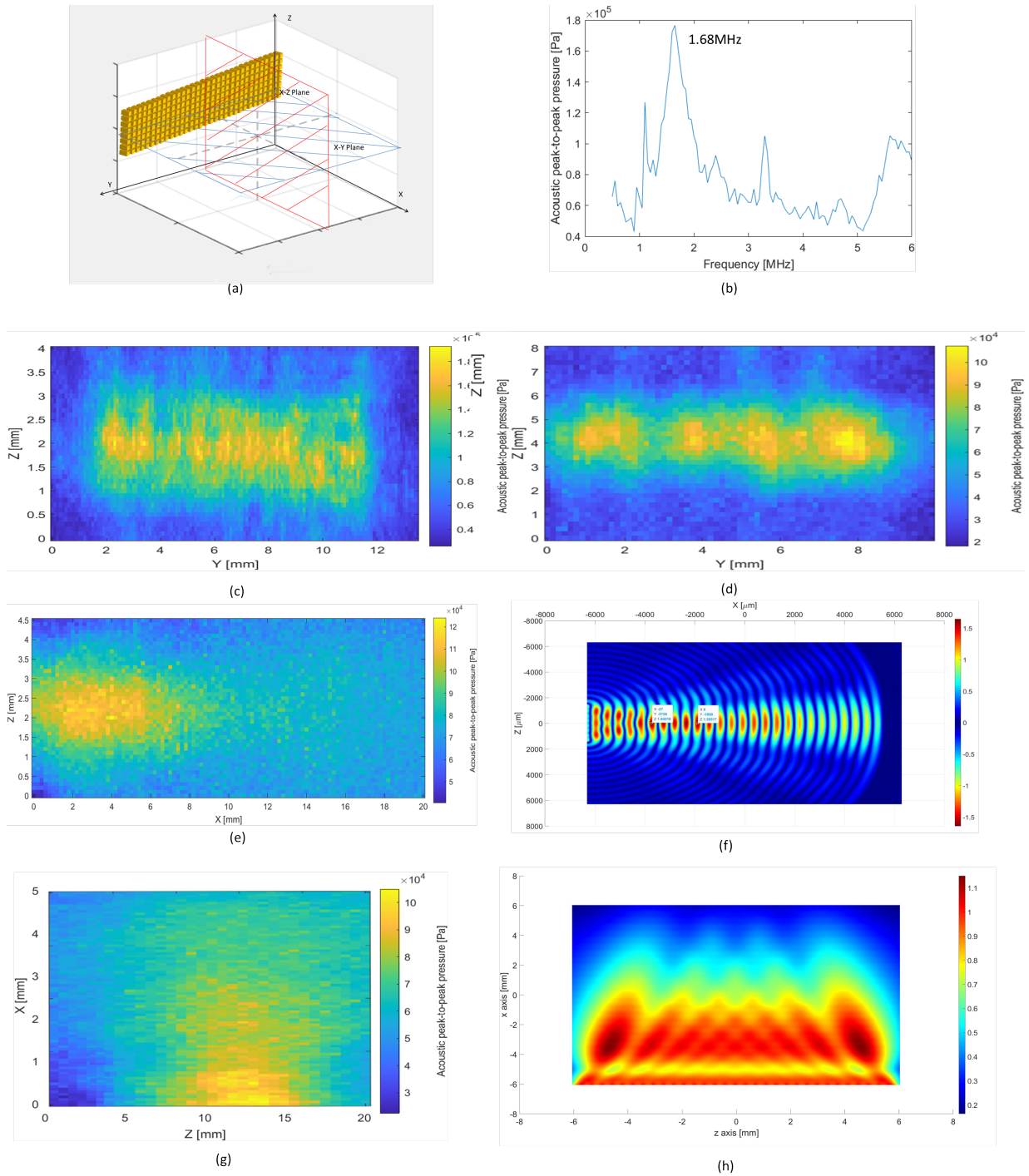


**Figure 5.5:** 2MHz PZT Array Transducer Performance Results: (a) Position Reference (b) Frequency Sweep at the Focal Point, Highlighting the 1.68MHz Resonance Frequency (c) Scanning of Y-Z Plane, Positioned 2μm Away, as a Confirmation of Individual Element Functionality (d)Scanning Y-Z Plane, Positioned at the Focus spot, 10μm Away (e) Scanning of Y-Z Plane, Shown that the Near Field Spot is Around 10um (f) Matlab simulation at the same Plane as e scanning (g) Scanning of X-Z Plane (h) Matlab simulation at the same Plane as g scanning

A thorough plane-wave analysis was conducted on a two-dimensional PZT array consisting of 256 elements. Initial observations from Figure 5.4 (b) indicate the resonant frequency of the array to be 1.68 MHz. The discrepancy between the observed frequency and the expected frequency based on thickness will be addressed in the subsequent section.

Observations from Figures 5.4 (c) and (d) provide insights into the array's performance at varying distances. The 2mm scan, shown in (c), aims to verify the functionality of all the 2D array elements. The results illustrate a consistent ultrasonic wave distribution across an area approximately 2.2mm wide and 10mm long. However, a slightly diminished wave strength, represented by the blue-green region in the upper right corner, suggests potential issues, possibly due to inadequate electrode contact with the piezoelectric element's contact pad or ground plane. Conversely, the 10mm scan displays four distinct focal points at the intended focusing distance. This observation aligns with expectations, as Figure 5.4 (h) demonstrates that an unmodulated array naturally forms a multi-peaked beam.

The last four plots present the real scanning results for the X-Y plane and the X-Z plane placed together with the corresponding MATLAB simulation results. The actual measurements are close to the pattern of the simulation results.

### 5.2.3. Prototype2 Dual-Frequency Transducer Performance

The second prototype has two rows of signal traces at each end, there were 48 traces controlling the peripheral array and 36 traces controlling the inner array. Since there is only one signal source, we control and test the two arrays separately. The theoretical near-field region for the internal array is calculated as follows

$$N = \frac{kL^2}{4\lambda} = \frac{kL^2}{4\frac{c}{f}} = \frac{1.37 \times (1.142)^2}{4 \times 0.37} \approx 1.206 \text{ mm} \tag{5.1}$$

The hydrophone could not be placed too close to the sample, so the measurement was taken from 1.2mm, and the result is shown in Figure 5.6.
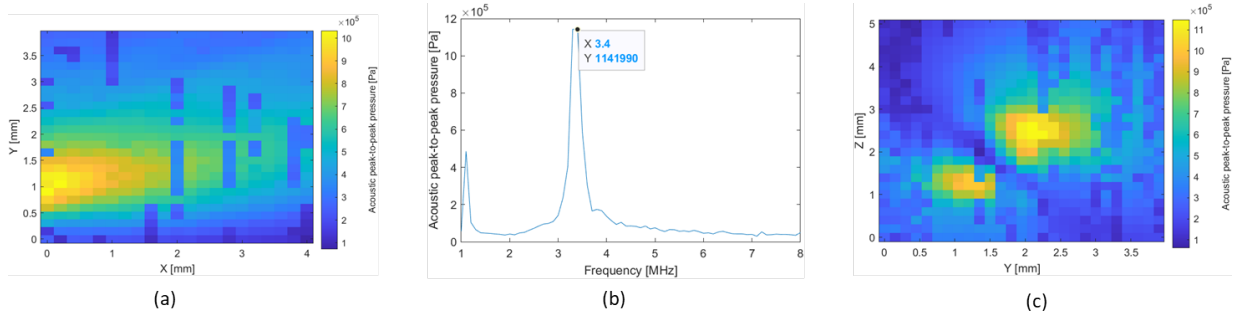


**Figure 5.6:** Results of the Prototype2 Dual-Frequency Transducer, Internal Array only: (a) Measurement Taken Perpendicular to the Device at a 1.2mm Distance. (b) Frequency Characterization 1.2mm Away from the Device. (c) Calculated Near-Field Point Measurement on the Plane Parallel to the Device

A resonant frequency of 3.4 MHz, and a pressure of 1.14 MPa were measured at the focal point of the calculation. Figure 5.6(c) shows that the focal region is about 1mm in diameter, and the pressure peak in the lower left corner may be the effect produced by the peripheral array. Unfortunately, testing the peripheral arrays individually didn't produce any compression, so it's possible that there is a bad connection somewhere, or that the sliver epoxy used by the peripheral arrays to act as a ground plane overflowed during the curing process and shorted out in contact with the contact pad.

## 5.3. Result Discussion

Measurements observed deviations of bulk piezoelectric blocks and array piezoelectric arrays from the calculated resonance frequencies of piezoelectric materials operating in the thickness mode, and the

deviations were homogeneous across multiple samples.

**Table 5.1:** Measurements fr Deviations from the Calculated fr

|  | PZT 1 | PZT 2 | PMN-PT |
|---|---|---|---|
| Calculated fr | 2MHz | 4MHz | 2.13MHz |
| Impedance Measured fr as a Device | 2.35MHz | — | 2.5MHz |
| Impedance Measured fr as a Strip | 2.31MHz | 4.71MHz | 2.53MHz |
| Measured fr in Bulk Shape | 2.3MHz | 4.56MHz | 2.56MHz |
| Measured fr in Array Shape | 1.68MHz | 3.34MHz | — |

Several studies have examined the distinct behavior of the resonant frequency in longitudinal piezoelectric blocks [62] [23] [63]. There are two primary types of bulk acoustic waves: the thickness shear mode and the longitudinal bulk mode [64], as shown in Figure 5.7 (a). When operating a longitudinal mode resonator in air, the mismatch in acoustic impedance causes the acoustic energy to be reflected back into the piezoelectric substrate, which is essential to sustain the resonant mode. The resonant wavelength is half the material's thickness. However, in this experiment, the piezoelectric block is not directly exposed to air—which possesses nearly zero acoustic impedance— on both sides. Instead, the side of the piezoelectric block facing the hydrophone is layered with electrodes, silver paste, Al foil, and water. The difference in impedance between these media and that of the piezoelectric material isn't as pronounced, leading to some acoustic energy loss or multiple vibrations.

Regarding the observation that the resonant frequency of the arrays was lower than the frequency corresponding to their thickness, it's postulated that this is due to the air-filled kerf between the arrays. The significant mismatch in their acoustic impedances could also induce a thickness shear mode. Another consideration is that for 2D arrays, both the thickness vibration Mode and the longitudinal mode are concurrently present[23] as shown in Figure 5.7 (b). When considering the air-filled 2D array as a 1-3 composite structure, it's imperative to note that its overall speed of sound differs from that of the standalone piezoelectric block. Drawing from the fundamental wavelength-frequency relationship, the inclusion of air within the array leads to a reduction in the speed of sound. Consequently, this decrease also results in a corresponding reduction in the resonance frequency. In this experiment, frequencies were scanned, with the assumption being that the frequency yielding the highest pressure within the examined range represents the resonance frequency. This frequency is indicative of the entire device's resonance, rather than a direct measurement of the material in isolation. As a result, the resonance frequency associated solely with the material's thickness cannot serve as the exclusive reference point.
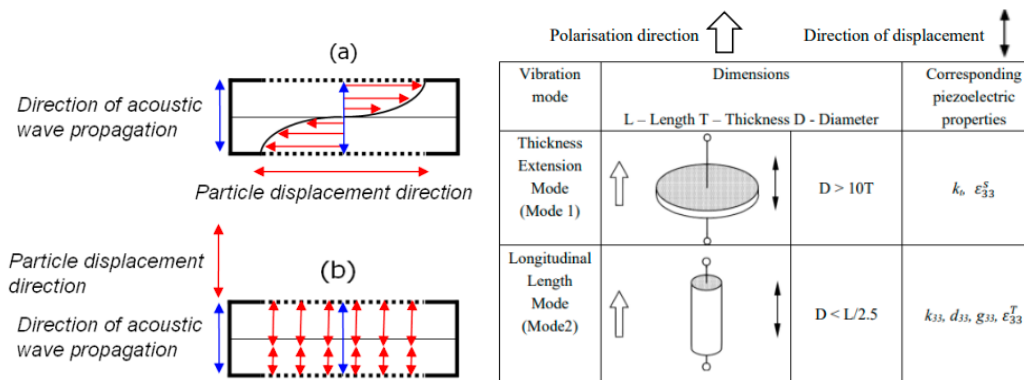


**Figure 5.7:** (a)Two Types of bulk Acoustic Vaves (b) Thickness Vibration Mode and the Longitudinal mode

**Transducer performance comparison**

Upon close examination of the collected data, it becomes evident that the performance of bulk PZT distinctly outperforms that of PMN-PT. One of the primary reasons for this divergence in performance is the assembly process of PMN-PT. The piezoelectric effect intrinsic to PMN-PT single crystals tends to be sensitive to external factors. When subjected to heat and mechanical pressure during assembly, these crystals can lose most of their piezoelectric efficiency.

Moving on to the bulk PZT versus the arrayed PZT comparison, the pressure variances are noteworthy. This difference is attributed to the kerf present in the array. In this context, the kerf leads to the removal of a certain portion of the PZT material in the arrayed configuration. Consequently, the effective piezoelectric area in the arrayed PZT is reduced to 70% of what is available in the bulk PZT. This dimensional reduction directly influences the pressure generation capacity of the arrayed PZT, making it proportionally lesser than its bulk counterpart. It's a clear indication of how material configuration can impact performance.

**Table 5.2:** Transducer Performance Comparison

|  | Fr | Volume Fraction | Max. Pressure | Natural Focus Spot |
|---|---|---|---|---|
| 2MHz Bulk PZT Transducer | 2.3MHz | 100% | 263kPa | 8.7mm |
| 2.13MHz Bulk PMN-PT Transducer | 2.56MHz | 100% | 54.7kPa | 5.23mm |
| 2MHz PZT Phased Array Transducer | 1.68MHz | 72.57% | 176kPa | 9~11mm |
| Prototype 2, 4MHz PZT Inter-Array | 3.4MHz | 58.17% | 1142kPa | 1.2mm |

Next is examining the second prototype equipped with a 4MHz PZT and comparing with the first prototype. Despite its aperture being a mere 5% of the size of the first prototype, it generates a staggering pressure that's six times that of the first. The reason could be:

- **Frequency Influence:** In the case of the second prototype, its 3.4MHz frequency inherently yields greater pressure compared to the 1.68MHz of its counterpart. Higher frequencies correspond to shorter wavelengths. Shorter wavelengths lead to a denser packing of wave cycles within a specific timeframe, resulting in amplified oscillations that exert greater pressure on their medium.

- **Substrate Thickness:** The backing layer's primary role is to absorb ultrasound energy that moves toward the back of the transducer, preventing it from reflecting back. This ensures that the energy is directed forward, toward the area of interest. The underside of the two prototypes are both copper-filled vias, except that one is 16mm thick and one is 1.6mm thick. Copper has a high density and acoustic impedance (41.6 MRayl), close to the acoustic impedance of the PZT (34 MRayl). The sensitivity of the transducer is reduced because more ultrasound energy is induced into the backing. Theoretically, as the backing material becomes thicker, its attenuation of ultrasound increases, so more ultrasound energy is absorbed.

- **Distance Dependency:** Ultrasound's effectiveness is intricately tied to the distance from its source. In the context of the second prototype, the measurements were executed in close proximity to the device. It's a foundational principle in acoustics that ultrasound pressure diminishes as we move away from its origin. This attenuation is largely attributed to wave energy dispersing over an expanding area, diluting its intensity. Consequently, when measurements are taken nearer to the source, the captured pressure is invariably higher.

6

# Conclusion

In this thesis, two prototypes of phased array piezoelectric ultrasound transducers are designed and fabricated for non-invasive UVNS applications, predominantly in the form of patches suitable for the neck region. The emphasis was on fabricating 2D arrays of piezoelectric transducers adaptable for phase control, with the vision that the transducers would possess both transmitter (TX) and receiver (RX) functions. We successfully fabricated a complete PZT 256-element array for the first prototype and compared the performance of the bulk PZT with the PMN-PT transducers. Additionally, we refined the PMN-PT machining and assembly processes. We also completed the assembly of the second prototype, offering insights into the full fabrication process. We assessed the device's capability to emit plane waves in a water tank, which simulates soft tissue, and analyzed the resultant sound intensity.

## 6.1. Key Results

Key insights from this research encompass:

**Materials and Configuration**: The design and optimisation of miniature UVNS transducer arrays are paramount. This endeavour delves into both advanced materials and array configurations. Two distinct materials were selected for the first prototype: the commercially available PZT and the relatively uncharted <001> oriented PMN-0.3PT piezoelectric single crystal. A comprehensive and proficient PZT transducer array was produced, and the cutting parameters of PMN-PT were also optimised to a significant degree.

**Prototyping**: Two distinct PCB prototypes were crafted throughout this study. The first is a 256-element rectangular transducer array situated on an 8-layer stacked rigid PCB. The second prototype is a flexible dual-band array, exemplifying the innovation requisite for imaging and neuromodulation functions.

**Fabrication Optimisation**: This study underscores the full integration of air-filled 2D arrays directly onto PCBs using the flip-chip method. No published studies currently document such fabrication optimisation in this domain. Months of meticulous optimisation ensured a vast majority of piezoelectric pillars remained undamaged on the substrate, boasting a remarkably low cluster rate.

**Evaluation**: Although instrumental constraints curtailed the comprehensive testing of phase-delay beam-forming and imaging capacities, preliminary evaluations were executed to ascertain the efficacy of plane wave generation.

**Implications**: The developed prototype can serve as a foundational model for subsequent studies, guiding future design considerations for customised piezoelectric ultrasonic transducers in UVNS. Insights into design and manufacturing, along with the optimisation recipes, hold the potential to expedite the prototyping phase of analogous projects, consequently conserving time and resources.

## 6.2. Limitations and Future Directions

This study, while pivotal in advancing knowledge in the field of UVNS transducer fabrication, carries some limitations which can serve as avenues for future exploration and refinement:

### 6.2.1. Assembly Process

1. **ACF Bonding**: In the study, the experimentation process for Prototype 1 faced challenges arising from the machine's diminutive needle tip. This restricted the exertion of adequate pressure, leading to the use of sub-sensitive ACF. Unfortunately, this choice did not achieve an optimal bond, resulting in significant bonding issues.

2. **Matching Layer**: When ultrasound waves move between different materials, they can reflect or transmit. For efficient transmission, the acoustic impedance of the transmitting medium should be close to that of the receiving one. Soft tissue's impedance is about 1.5 MRayl, similar to water, but much lower than piezoelectric materials like PZT, which is 33 MRayl. This disparity causes most waves to reflect back, rather than moving into the tissue. A matching layer bridges this gap, allowing waves to transfer effectively between layers. The matching layer should $\lambda/4$ with the acoustic impedance of:

$$Z_m = \sqrt{Z_P Z_L} \tag{6.1}$$

In which $\lambda$ is the wavelength of the ultrasound produced by the transducer; $Z_P$ and $Z_L$ represent the acoustic impedances of the piezoelectric transducer and the soft tissue, respectively. Applying two or three matched layers can achieve better performance. The acoustic impedance with two matching layers is respectively:

$$Z_{m1} = \sqrt[7]{Z_P^4 Z_L^3} \tag{6.2}$$

$$Z_{m2} = \sqrt[7]{Z_P Z_L^3} \tag{6.3}$$

Some options include AZ31B Magnesium alloy with an acoustic impedance of 10.36MRayl, a mixture of tungsten powders (9.5MRayl) with EPO-TEK 301-2 (2.4MRayl), or Parylene C at 2.5MRayl.

3. **Air Backing**: Air-backing is a way to maximize transmit efficiency. Air has a very low acoustic impedance compared to most materials, especially piezoelectric materials. When the backside of a piezoelectric transducer element is backed by air, the acoustic waves generated in the reverse direction (away from the target medium) get almost entirely reflected back into the piezoelectric material due to this huge impedance mismatch. This causes the transducer to vibrate more vigorously and produce stronger waves in the forward direction. Also, the air-backing provides minimal damping to the oscillations of the piezoelectric element. This allows the transducer to resonate more freely, resulting in a higher amplitude of transmitted waves. It also contributes to pulse length reduction. With air-backing, the time the transducer takes to stop ringing after a pulse is reduced. This can help in achieving shorter pulse lengths, which is often desirable for improving axial resolution in imaging applications.

For the PCB prototype, air-backing can be achieved by leaving the via-in-pad unfilled, essentially creating a hollow cylinder with an internal copper conductive layer. However, due to the eight-layer stack of Prototype 1 being 1.6mm thick, this arrangement becomes unfeasible because of the excessively long and dense hollow cylinders. The manufacturer suggests that PCBs with six layers or fewer can successfully incorporate hollow vias, thus facilitating air-backing.

### 6.2.2. PMN-PT Dicing Optimisation

1. **Blade Selection**: The inability to fabricate the PMN-PT arrays may be attributed to the incompatibility of the Z09 series blades available in the lab. Different blades have varying profiles, sharpness, and construction materials, which make them suitable for specific cutting tasks. The inappropriate blade choice can lead to uneven stresses during cutting, resulting in micro-cracks, fractures, or other defects in the material. Wu et al. found a significant improvement in cutting yield when they employed the 10um disco-made model from the ZHZZ series [23]. This underscores the critical role blade selection plays in

ensuring the integrity and quality of the material being processed.

2. **Temperature Control**: Proper temperature management during fabrication is crucial to preserve the material's piezoelectric traits. Keeping temperatures below the transition temperature (Trt) is essential. Using lower curing epoxy and extending its curing time can mitigate excessive heat exposure. Assembling under ambient conditions, especially for Anisotropic Conductive Film (ACF) bonding, is also recommended.

3. **Repoling After Dicing**: Degradation in the performance of PMN-PT after dicing and assembly has been shown in multiple studies [65]. One of the proven techniques to restore the piezoelectric properties of PMN-PT is repoling. Tools required are simply a high-voltage amplifier and a silicon oil bath. Connect the sample electrodes to a high-voltage power supply and immerse them in a silicone oil bath. The temperature of this bath ranges from 100°C to 200°C. Depending on the material type and its thickness, apply a voltage between 500 to 2000 V/cm. The polarization field should exceed the coercive field, typically falling between 4.5-6 kV/cm, as advised by sources like piezo.com. Other research references suggest repoling parameters at room temperature, such as applying a DC electric field of 1.5 kV/mm for 15 minutes or 20 kV/cm for 3 minutes [66] [67].

### 6.2.3. Prototype2 Assembly

For the internal array, a 50-μm-wide blade was used, resulting in a kerf of 50 μm. This led to a low volume fraction of 58% for the active elements. Additionally, a mismatch between the shape of the contact pad and the PZT array caused misalignment. In future iterations, using a 20-μm blade will result in a higher volume fraction and produce a larger pressure force.

In the future, peripheral arrays can be fabricated through multiple attempts. Manual placement of the outer array has resulted in significant misalignment, indicating the need for a pick-and-place tool. Any mismatched tips could be replaced with specialized 3D-printed ones. It's also recommended to utilize 3D-printed molds for positioning the ground plane during assembly. Given that the inner and outer arrays have different heights, it would be optimal to print molds with a raised center and a lowered periphery. This design allows the device to be inverted and aligned with the mold. By doing so, a conductive adhesive can be applied to the center, and the components can then be cured together, ensuring a stable bond

### 6.2.4. Characterisation

1. **Beamforming Tests with Verasonics 256**: The prototype was designed in line with phased array parameter requirements. Its beamforming capabilities can be assessed using platforms like Verasonics 256, which provides a detailed insight into the device's overall performance.

2. **Component Control**: The prototype was designed in line with phased array parameter requirements. Its beamforming capabilities can be assessed using platforms like Verasonics 256, which provides a detailed insight into the device's overall performance.

3. **d33 Meter Utilisation**: Using a d33 meter enables precise measurements of d33 at each phase of the manufacturing process. Such granularity not only highlights specific areas for enhancement but also offers crucial insights into the overall efficiency and evolution of production.

4. **Acoustic Impedance Measurement**: The acoustic impedance of a material is a crucial parameter, especially since it can vary when the material is diced or when different filler materials are used. To determine it, one can employ Archimedes' principle. Once the array's density and the transverse velocity of sound propagation are established, the Z can be computed using the equation $Z = \rho c$.

# References

[1] Bruno Bonaz et al. "Vagus nerve stimulation: from epilepsy to the cholinergic anti-inflammatory pathway". In: *Neurogastroenterology & Motility* 25.3 (2013), pp. 208–221.

[2] S Fetzer et al. "A systematic review of magnetic resonance imaging in patients with an implanted vagus nerve stimulation system". In: *Neuroradiology* 63 (2021), pp. 1407–1417.

[3] PJ Goadsby et al. "Effect of noninvasive vagus nerve stimulation on acute migraine: an open-label pilot study". In: *Cephalalgia* 34.12 (2014), pp. 986–993.

[4] Yue Wang et al. "Vagus nerve stimulation in brain diseases: Therapeutic applications and biological mechanisms". In: *Neuroscience & Biobehavioral Reviews* 127 (2021), pp. 37–53.

[5] Joseph Blackmore et al. "Ultrasound neuromodulation: a review of results, mechanisms and safety". In: *Ultrasound in medicine & biology* 45.7 (2019), pp. 1509–1536.

[6] Wanjia Gao et al. "Study of ultrasonic near-field region in ultrasonic liquid-level monitoring system". In: *Micromachines* 11.8 (2020), p. 763.

[7] KARL F Graff. "A history of ultrasonics". In: *Physical Acoustics V15* (2012).

[8] Etienne Balmes et al. *Modeling structures with piezoelectric materials: Theory and SDT Tutorial*. General info `http://www.sdtools.com`, Support `http://support.sdtools.com`. SDTools. 44 rue Vergniaud, 75013 Paris (France), 2019. URL: `http://www.sdtools.com`.

[9] "Publication and Proposed Revision of ANSI/IEEE Standard 176-1987 "ANSI/IEEE Standard on Piezoelectricity"". In: *IEEE Transactions on Ultrasonics, Ferroelectrics and Frequency Control* 43 (1996), pp. 717–.

[10] Thomas L Szabo. *Diagnostic ultrasound imaging: inside out*. Academic press, 2004.

[11] I Standard. "IEEE standard on piezoelectricity". In: *ANSI/IEEE Std* (1988), pp. 176–1987.

[12] Wallace Arden Smith. "Composite piezoelectric materials for medical ultrasonic imaging transducers-a review". In: *Sixth IEEE International Symposium on Applications of Ferroelectrics*. IEEE. 1986, pp. 249–256.

[13] Yuan Zhuang. "Loss phenomenology and the methodology to derive loss factors in piezoelectric ceramics". In: (2011).

[14] Qifa Zhou et al. "Piezoelectric single crystal ultrasonic transducers for biomedical applications". In: *Progress in Materials Science* 66 (2014), pp. 87–111. DOI: `https://doi.org/10.1016/`

`j.pmatsci.2014.06.001`. URL: `https://www.sciencedirect.com/science/article/pii/S0079642514000541`.

[15] Rob Carter et al. "Introduction to piezoelectric transducers". In: *Midé Technology Corp., Woburn, MA, USA* (2020).

[16] D Berlincourt et al. "Properties of Morgan electro ceramic ceramics". In: *Technical Publication TP-226, Morgan Electro Ceramics* (2000).

[17] Qiu-chen Wu et al. "Nonlinear dielectric effect of Fe2O3-doped PMS–PZT piezoelectric ceramics for high-power applications". In: *Ceramics International* 43.14 (2017), pp. 10866–10872.

[18] Kazuhiko Echizenya et al. "PMN-PT and PIN-PMN-PT piezoelectric single crystals with stable properties". In: *JFE Tech. Rep.* 47 (2021), pp. 50–55.

[19] F Stuart Foster et al. "A history of medical and biological imaging with polyvinylidene fluoride (PVDF) transducers". In: *IEEE transactions on ultrasonics, ferroelectrics, and frequency control* 47.6 (2000), pp. 1363–1371.

[20] Heng Li et al. "Fabrication of single crystal based phased array medical imaging ultrasonic transducers". In: (2008).

[21] L Luo et al. "Single Crystal PZN-PT, PMN-PT, PSN-PT, and PIN-PT-Based Piezoelectric Materials". In: *Advanced Piezoelectric Materials* (2010), pp. 271–318.

[22] D.N. Stephens et al. "The effective coupling coefficient for a completed PIN-PMN-PT array". In: *Ultrasonics* 109 (2021), p. 106258. DOI: `https://doi.org/10.1016/j.ultras.2020.106258`. URL: `https://www.sciencedirect.com/science/article/pii/S0041624X20301979`.

[23] Weichang Wu. "High-Frequency Phased Array Ultrasonic Transducer". PhD thesis. UNSW Sydney, 2020.

[24] Jie Chen et al. "Commercialization of piezoelectric single crystals for medical imaging applications". In: *IEEE Ultrasonics Symposium, 2005.* Vol. 1. IEEE. 2005, pp. 235–240.

[25] Shuai Yang et al. "Textured ferroelectric ceramics with high electromechanical coupling factors over a broad temperature range". In: *Nature communications* 12.1 (2021), p. 1414.

[26] Noriko Yamamoto et al. "Electrical and physical properties of repoled PMN–PT single-crystal sliver transducer". In: *Sensors and Actuators A: Physical* 200 (2013). Selected Papers from the 9th International Workshop on Piezoelectric Materials and Applications in Actuators, pp. 16–20. DOI: `https://doi.org/10.1016/j.sna.2012.10.002`. URL: `https://www.sciencedirect.com/science/article/pii/S0924424712006127`.

[27] Yujia Jing et al. "Property enhancement in relaxor-PbTiO3 single crystals by alternating current poling: Evaluation of intrinsic and extrinsic contributions". In: *Ceramics International* 48.8 (2022),

pp. 11764–11771. DOI: `https://doi.org/10.1016/j.ceramint.2022.01.035`. URL: `https://www.sciencedirect.com/science/article/pii/S0272884222000360`.

[28] Yan Chen et al. "High performance relaxor-based ferroelectric single crystals for ultrasonic transducer applications". In: *Sensors* 14.8 (2014), pp. 13730–13758.

[29] Ángel Verges Moreno et al. "Sistema de caracterización de palpadores Phased Array". In: (2018).

[30] Rayyan Manwar et al. "Transfontanelle photoacoustic imaging: ultrasound transducer selection analysis". In: *Biomedical Optics Express* 13.2 (2022), pp. 676–693.

[31] NDT Olympus. "Introduction to phased array ultrasonic technology applications". In: *D Tech Guideline", Olympus NDT* (2004).

[32] K Heath Martin et al. "Dual-frequency piezoelectric transducers for contrast enhanced ultrasound imaging". In: *Sensors* 14.11 (2014), pp. 20825–20842.

[33] Vida Pashaei et al. "Flexible body-conformal ultrasound patches for image-guided neuromodulation". In: *IEEE Transactions on Biomedical Circuits and Systems* 14.2 (2019), pp. 305–318.

[34] Alejandra Ortega Castrillon. "Novel beamforming methods for fast volumetric cardiac imaging using ultrasound". In: (2016).

[35] A Abrar et al. "1–3 connectivity piezoelectric ceramic–polymer composite transducers made with viscous polymer processing for high frequency ultrasound". In: *Ultrasonics* 42.1-9 (2004), pp. 479–484.

[36] Yaoyao Zhang et al. "Fabrication of PIMNT/Epoxy 1-3 composites and ultrasonic transducer for nondestructive evaluation". In: *IEEE Transactions on Ultrasonics, Ferroelectrics, and Frequency Control* 58.9 (2011), pp. 1774–1781. DOI: `10.1109/TUFFC.2011.2014`.

[37] Gordon Hayward et al. "A theoretical study on the influence of some constituent material properties on the behavior of 1-3 connectivity composite transducers". In: *The Journal of the Acoustical Society of America* 98.4 (1995), pp. 2187–2196.

[38] Beth A Schrope et al. "Physical principles of Ultrasound". In: *Abdominal Ultrasound for Surgeons*. Springer, 2014, pp. 7–15.

[39] Alexander Ng et al. "Resolution in ultrasound imaging". In: *Continuing Education in Anaesthesia, Critical Care & Pain* 11.5 (2011), pp. 186–192.

[40] Ahmad Safari et al. "Development of fine-scale piezoelectric composites for transducers". In: *AIChE journal* 43.S11 (1997), pp. 2849–2856.

[41] Yan Li et al. "PMN-PT/Epoxy 1-3 composite based ultrasonic transducer for dual-modality photoacoustic and ultrasound endoscopy". In: *Photoacoustics* 15 (2019), p. 100138. DOI: `https:`

//doi.org/10.1016/j.pacs.2019.100138. URL: `https://www.sciencedirect.com/science/article/pii/S2213597919300035`.

[42] Jinpeng Ma et al. "Performance enhancement of 1–3 piezoelectric composite materials by alternating current polarising". In: *Ceramics International* 47.13 (2021), pp. 18405–18410. DOI: `https://doi.org/10.1016/j.ceramint.2021.03.163`. URL: `https://www.sciencedirect.com/science/article/pii/S0272884221008506`.

[43] Dan Zhou et al. "Lead-free piezoelectric single crystal based 1–3 composites for ultrasonic transducer applications". In: *Sensors and Actuators A: Physical* 182 (2012), pp. 95–100. DOI: `https://doi.org/10.1016/j.sna.2012.05.030`. URL: `https://www.sciencedirect.com/science/article/pii/S0924424712003299`.

[44] Ruibin Liu et al. "Interdigital pair bonding for high frequency (20-50 MHz) ultrasonic composite transducers". In: *IEEE Transactions on Ultrasonics, Ferroelectrics, and Frequency Control* 48.1 (2001), pp. 299–306. DOI: `10.1109/58.896143`.

[45] Jiabing Lv et al. "Cold ablated high frequency PMN-PT/Epoxy 1-3 composite transducer". In: *Applied Acoustics* 188 (2022), p. 108540. DOI: `https://doi.org/10.1016/j.apacoust.2021.108540`. URL: `https://www.sciencedirect.com/science/article/pii/S0003682X21006344`.

[46] JR Yuan et al. "5I-1 Microfabrication of piezoelectric composite ultrasound transducers (PC-MUT)". In: *2006 IEEE Ultrasonics Symposium*. IEEE. 2006, pp. 922–925.

[47] Tiago Costa et al. "An integrated 2D ultrasound phased array transmitter in CMOS with pixel pitch-matched beamforming". In: *IEEE Transactions on Biomedical Circuits and Systems* 15.4 (2021), pp. 731–742.

[48] Ziyuan Wang et al. "Fabrication of 2-D capacitive micromachined ultrasonic transducer (CMUT) array through silicon wafer bonding". In: *Micromachines* 13.1 (2022), p. 99.

[49] FOCUSLIGHT TECHNOLOGIES INC. W. Gu. *As Displays Evolve, Lasers Offer New Bonding Options*. 2019. URL: `https://www.photonics.com/Articles/As_Displays_Evolve_Lasers_Offer_New_Bonding/a66239`.

[50] Yipeng Lu et al. "Modeling, Fabrication, and Characterization of Piezoelectric Micromachined Ultrasonic Transducer Arrays Based on Cavity SOI Wafers". In: *Journal of Microelectromechanical Systems* 24.4 (2015), pp. 1142–1149. DOI: `10.1109/JMEMS.2014.2387154`.

[51] Christina Hassler et al. "Characterization of parylene C as an encapsulation material for implanted neural prostheses". In: *Journal of Biomedical Materials Research Part B: Applied Biomaterials: An Official Journal of The Society for Biomaterials, The Japanese Society for Biomaterials, and The Australian Society for Biomaterials and the Korean Society for Biomaterials* 93.1 (2010), pp. 266–274.

[52]  Franck Levassort et al. "Characterisation of thin layers of parylene at high frequency using PZT thick film resonators". In: *Journal of the European Ceramic Society* 25.12 (2005), pp. 2985–2989.

[53]  B. Hadimioglu et al. "Polymer films as acoustic matching layers". In: *IEEE Symposium on Ultrasonics*. 1990, 1337–1340 vol.3. DOI: `10.1109/ULTSYM.1990.171581`.

[54]  X Zhuang et al. "Biocompatible coatings for CMUTs in a harsh, aqueous environment". In: *Journal of micromechanics and microengineering* 17.5 (2007), pp. 994–1001.

[55]  Chunying Wang et al. "Effect of kerf filler on the electromechanical coupling coefficient of 1–3 piezoelectric composites". In: *Journal of Alloys and Compounds* 651 (2015), pp. 643–647.

[56]  S. Michau et al. "Single crystal-based phased array for transoesophagial ultrasound probe". In: *2002 IEEE Ultrasonics Symposium, 2002. Proceedings.* Vol. 2. 2002, 1269–1272 vol.2. DOI: `10.1109/ULTSYM.2002.1192525`.

[57]  Rachael McPhillips et al. "The fabrication and integration of a 15 MHz array within a biopsy needle". In: *2017 IEEE International Ultrasonics Symposium (IUS)*. IEEE. 2017, pp. 1–4.

[58]  Muhammad Saleem Mirza et al. "Dice-and-fill processing and characterization of microscale and high-aspect-ratio (K, Na) NbO3-based 1–3 lead-free piezoelectric composites". In: *Ceramics International* 42.9 (2016), pp. 10745–10750.

[59]  Xiaoning Jiang et al. "Single crystal piezoelectric composites for advanced NDT ultrasound". In: *Nondestructive Characterization for Composite Materials, Aerospace Engineering, Civil Infrastructure, and Homeland Security 2007*. Vol. 6531. SPIE. 2007, pp. 108–115.

[60]  Chi Tat Chiu et al. "Fabrication and Characterization of a 20-MHz Microlinear Phased-Array Transducer for Intervention Guidance". In: *IEEE Transactions on Ultrasonics, Ferroelectrics, and Frequency Control* 64.8 (2017), pp. 1261–1268. DOI: `10.1109/TUFFC.2017.2709623`.

[61]  MR Sadiq et al. "Characterization of PMN-29% PT as a function of temperature and pressure". In: *2011 IEEE International Ultrasonics Symposium*. IEEE. 2011, pp. 1825–1828.

[62]  Chao Zhong et al. "Characterization of an improved 1-3 piezoelectric composite by simulation and experiment". In: *Journal of Applied Biomaterials & Functional Materials* 15.1_suppl (2017), pp. 38–44.

[63]  AR Selfridge et al. "Fundamental concepts in acoustic transducer array design". In: *1980 Ultrasonics Symposium*. IEEE. 1980, pp. 989–993.

[64]  Christopher D Corso. *Theoretical and experimental development of a zinc oxide-based laterally excited thickness shear mode acoustic wave immunosensor for cancer biomarker detection*. Georgia Institute of Technology, 2008.

[65]  Noriko Yamamoto et al. "Electrical and physical properties of repoled PMN–PT single-crystal sliver transducer". In: *Sensors and Actuators A: Physical* 200 (2013), pp. 16–20.

[66]  Dan Zhou et al. "Fabrication and performance of endoscopic ultrasound radial arrays based on PMN-PT single crystal/epoxy 1-3 composite". In: *IEEE transactions on ultrasonics, ferroelectrics, and frequency control* 58.2 (2011), pp. 477–484.

[67]  Nestor E Cabrera-Munoz et al. "Fabrication and characterization of a miniaturized 15-MHz side-looking phased-array transducer catheter". In: *IEEE Transactions on Ultrasonics, Ferroelectrics, and Frequency Control* 66.6 (2019), pp. 1079–1092.